This is to certify that the
dissertation entitled

PERFORMANCE PREDICTION AND PRELIMINARY DESIGN
OF WAVE ROTORS ENHANCING GAS TURBINE CYCLES

presented by

PEZHMAN AKBARI

has been accepted towards fulfillment
of the requirements for the

Ph.D. degree in Mechanical Engineering

Major Professor's Signature

8/23/2004

Date

DATE DUE	DATE DUE	DATE DUE

PERFORMANCE PREDICTION AND PRELIMINARY DESIGN OF WAVE ROTORS ENHANCING GAS TURBINE CYCLES

By

Pezhman Akbari

A DISSERTATION

Submitted to
Michigan State University
in partial fulfillment of the requirements
for the degree of

DOCTOR OF PHILOSOPHY

Department of Mechanical Engineering

2004

ABSTRACT

PERFORMANCE PREDICTION AND PRELIMINARY DESIGN OF WAVE ROTORS ENHANCING GAS TURBINE CYCLES

By

Pezhman Akbari

Wave rotors as a family of unsteady-flow devices have shown unique capabilities to enhance the performance and operating characteristics of a variety of engines and machinery utilizing thermodynamic cycles. The wave rotor is an unsteady-flow machine that utilizes compression and expansion waves to exchange energy between fluids with different pressures. The first part of this study presents several thermodynamic cycle analyses proving the performance improvement of small gas turbines (microturbines) by implementing various advantageous four-port wave rotor topping cycles. General performance maps are generated showing the design space and optima for baseline and topped engines. In the second part of this work, a one-dimensional analytical gasdynamic model of the high-pressure phase is suggested to calculate flow characteristics inside the wave rotor channels. Useful design parameters such as port widths and rotor size are determined by computing transit times of the waves traveling inside the channels. Reasonable agreement has been found comparing the predicted results of the analytical design procedure with the available numerical data. Using the commercial software FLUENT, some CFD simulations are performed showing that commonly available CFD software can be utilized for wave rotor simulations and to support their design. Overall, the predicted results are in good agreement with established wave rotor theories. Finally, several innovative wave rotor concepts and designs including have been studied.

To My Family

ACKNOWLEDGMENTS

I would like first to express my gratitude to my supervisor Prof. Norbert Müller for providing an opportunity to make the present research a true learning process. He generously allowed me to start this work in order to learn and satisfy my own curiosity. His sense of guidance, unending patience, refreshing humor, and friendly suggestions have made my research experience both fruitful and enjoyable. His encouragement and timely advice have always helped me to overcome the difficulties I faced during my research. I consider myself lucky to have Prof. Norbert Müller as my supervisor.

I have had a privilege to learn a lot from my Ph.D. committee members. As a former student of Prof. Indrek Wichman, I admire his inspiring work and his continuous support. Prof. Abraham Engeda deserves my special thanks as one of the most supportive advisors through my research, offering very helpful discussions and suggestions. I am also grateful to Prof. Farhad Jaberi on my Ph.D. committee for his valuable suggestions. He has always been a valuable mentor and an excellent model for me. Special thanks to Prof. Charles MacCluer for serving on my Ph.D. committee. His helpful advice and feedback have been very beneficial for me. I am also very thankful to Prof. Razi Nalim at the Purdue School of Engineering and Technology at IUPUI. As an acting member of my Ph.D. committee and top specialist in his field, he has provided me with continuous and valuable guidance in improving this work.

I would particularly like to thank Prof. Jenasz Piechna at Warsaw University of Technology in Poland with whom I have had many constructive discussions. I appreciate his unique talents and brightness and enjoy his friendship.

Thanks to Prof. Manoochehr Koochesfahani for assisting me to begin my Ph.D. at MSU. I am honored to had a chance to work in his laboratory in the early stages of my Ph.D. program. I am also very grateful to my former supervisor Prof. Kaveh Ghorbanian at Sharif University of Technology in Iran who first inspired me to work on such a challenging topic. Working with him was a valuable and enjoyable undertaking.

This work would have never been completed without the support of several colleagues in the MSU Turbomachinery Laboratory. I am thankful for the collaboration and friendship of Florin Iancu whose assistance in numerical simulations performed in this work is appreciated. His patience during our collaboration is appreciated. I would like to thank Amir A. Kharazi for a productive collaboration, leading to our several technical publications. The materials presented in Chapter 6 are the result of my collaboration with the above friends at the MSU wave rotor team. I am also very thankful to Azadeh Behinfar as a real friend and a great source of support. Several of the 3D sketches presented here are results of her excellent skills. Thanks for keeping me happy during those difficult moments.

Finally and most importantly, I certainly remain indebted to my parents and all other family members for their continuing love, encouragement, and endless support through this journey. I could never pay them back what they have given me.

TABLE OF CONTENTS

LIST OF TABLES

LIST OF FIGURES

CHAPTER 1: INTRODUCTION

1.1 Unsteady-Flow Devices

Oscillatory and pulsatile fluid motion has been neatly utilized in nature, yet is comparatively poorly studied by engineers despite the invention of cyclically operating engines and machines. The potential for utilizing unsteady flows has been recognized since the early twentieth century but neglected as long as substantive improvements could be made to conceptually simple steady-flow or semi-static devices. Also, the inherent non-linearity of large-amplitude wave phenomena in compressible fluids and unusual geometry of non-steady flow devices necessitates detailed calculations, which until recently were too laborious or expensive or imprecise. By understanding and exploiting complex unsteady flows, a quantum increase in engine performance is possible. Often it has been feasible to simplify the hardware of engines, making them less costly, more responsive, and more durable by employing unsteady-flow processes.

Shock tubes, shock tunnels, pulse combustors, pulse detonation engines, and wave rotors are a few examples of unsteady-flow devices. The basic concept underlying these devices is the transfer of energy by pressure waves. By generating compression and expansion waves in appropriate geometries, wave machines can transfer energy directly between different fluids without using mechanical components such as pistons or vaned impellers. In fact, these devices properly represent applications of classical, unsteady, one-dimensional, compressible flow theory. The major benefit of these unsteady-flow machines is their potential to generate much greater pressure rises than those obtained in steady-state flow devices [1, 2]. For instance as illustrated in Figure 1, for the same change from a given inlet Mach number M_1 to a given outlet Mach number M_2, the local

(static) pressure ratio p_2/p_1 across a single shock wave (solid line) moving in a frictionless channel is always much greater than that obtained by an isentropic deceleration in a 100% efficient diffuser (dotted line). However, it must be noted that friction effects always exist, and hence pressure gains are actually less than those predicted by Figure 1.

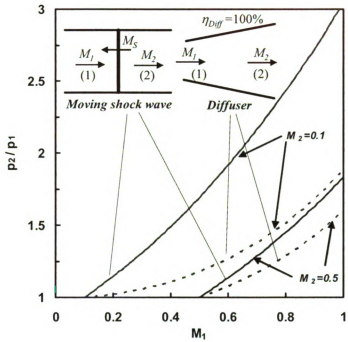

Figure 1: Comparison of pressure gain (local pressure ratio) of moving shock and steady-flow isentropic diffuser for γ=1.4

It is also worthwhile to note that shock wave compression is a relatively efficient process as indicated in Figure 2, where shock isentropic efficiency η_{Shock} (red) is compared with compressor isentropic efficiency $\eta_{Compressor}$ (green) and diffuser isentropic efficiency $\eta_{Diffuser}$ (blue). Figure 2 shows variations of these parameters as functions of the pressure gain p_2/p_1 obtained by a moving shock wave in a frictionless channel, by a compressor with different values of polytropic efficiencies, and by a diffuser with

different values of total pressure drop across the diffuser expressed by p_{t2}/p_{t1}, respectively. The comparison reveals that for the same pressure gain p_2/p_1, the ideal shock compression efficiency may far exceed the efficiency obtained by a decelerating diffuser or a compressor. For example, it is seen that for a pressure gain of up to p_2/p_1 =2.2, η_{Shock} is greater than about 93% and thus is greater than those of typical diffusers and compressors. Therefore a gain in cycle performance can be expected when a compressor (or a diffuser) is replaced by an unsteady-flow device utilizing shock waves. Flow friction-effects would lower the efficiency of wave devices and reduces their efficiency advantage (not shown in Figure 2), but the relative advantage is expected to persist. Detailed calculations for developing Figure 1 and Figure 2 are presented in Appendix A.

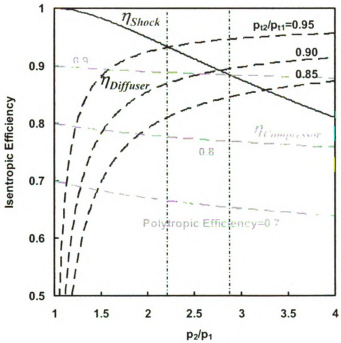

Figure 2: Shock wave, diffuser, and compressor isentropic efficiencies as functions of pressure gain

1.2 Wave Rotors

There are at least two classes of wave machines: rotating wave machines and non-rotating wave machines. Dynamic pressure exchangers and wave rotors are two types of rotating wave devices developed to reach the high performance targets of thermodynamic cycles. In Europe, however, both terms have been often used interchangeably [3].

The essential feature of wave rotors is an array of channels arranged around the axis of a cylindrical drum. As schematically shown in Figure 3, the drum rotates between two end plates each of which has a few ports or manifolds, controlling the fluid flow through the channels. The number of ports and their positions vary for different applications. By carefully selecting their locations and widths to generate and utilize wave processes, a significant and efficient transfer of energy can be obtained between flows in the connected ducts.

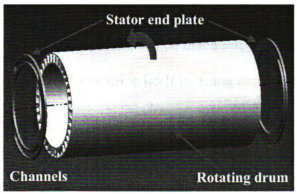

Figure 3: Schematic configuration of a typical wave rotor

Through rotation, the channel ends are periodically exposed to the ports located on the stationary end plates initiating compression and expansion waves within the wave rotor channels. Thus, pressure is exchanged dynamically between fluids by utilizing unsteady pressure waves. Therefore, unlike a steady-flow turbomachine which either

compresses or expands the fluid, the wave rotor accomplishes both compression and expansion within a single component. To minimize leakage, the gap between the end plates and the rotor has to be very small or the end plates with sealing material could contact the rotor.

An inverted design with stationary rotor and rotating ports is also possible [4]. Such a configuration has more than one rotating part and usually doubles interfaces that need to be sealed between rotating and stationary parts. However, it may be preferred for laboratory investigations because it easily enables flow measurement in the channels where the important dynamic interactions take place. However, this arrangement rarely seems to be convenient for commercial purposes.

The rotor may be gear or belt driven or preferably direct driven by an electrical motor (not shown). The power required to keep the rotor at a correctly designed speed is negligible [5, 6]. It only needs to overcome rotor windage and friction in the bearings and contact sealing if used. Alternatively, rotors can be made self-driving. This configuration, known as the "free-running rotor", can drive itself by using the momentum of the flow to rotate the rotor [7, 8].

In wave rotor machines, two basic fluid-exchange processes usually happen at least once per revolution of the rotor: the high-pressure process (charging process) and the low-pressure process (scavenging process). In the high-pressure process, compression waves transfer the energy directly from a fluid at a higher pressure (driver fluid) to another fluid at a lower pressure (driven fluid). In the low-pressure process the driver fluid is scavenged from the rotor channels, using expansion waves. Generation of expansion waves allows ingestion of a fresh low-pressure fluid into the rotor channels.

There are several important advantages of wave rotor machines. Their rotational speed is low compared with turbomachines, which results in low material stresses. But they can respond on the timescale of pressure waves, with no rotor inertial lag. From a mechanical point of view, their geometries can be simpler than those of turbomachines. Therefore, they can be manufactured relatively inexpensively. Also, the rotor channels are less prone to erosion damage than the blades of turbomachines. This is mainly due to the lower velocity of the working fluid in the channels, which is about one-third of what is typical within turbomachines [5]. Another important advantage of wave rotors is their self-cooling capabilities. They are naturally cooled by the fresh cold fluid ingested by the rotor. Therefore, applied to a heat engine, the rotor channels pass through both cool air and hot gas flow in the cycle at least once per rotor revolution. As a result, the rotor material temperature is always maintained between the temperature of the cool air which is being compressed, and the hot gas which is being expanded.

Despite very attractive features, several challenges have impeded the vast appearance of commercial wave rotors in some applications though numerous research efforts have been carried out during the past century. Besides unusual flow complexity and anticipated off-design problems and uncertainties about the selection of the best wave rotor configuration for a particular application, the obstacles have been mainly of a mechanical nature, like sealing and thermal expansion issues, as mentioned throughout this study. However, due to the recent energy crises, technology improvement, and economic reasons, new desires for wave rotor technology have been stimulated.

1.3 Wave Rotor Applications

As a combined expansion and compression device, the wave rotor can be used as a supercharging device for IC engines, a topping component for gas turbines, in

refrigeration cycles, and more. In advanced configurations, combustion occurs internally in the wave rotor channels allowing extremely short residence times at high temperature, hence potentially reducing NO_X emissions. A condensing wave rotor may be viewed as a similarly advanced configuration that enhances the performance of water refrigeration cycles. Recently, wave rotor technology has been envisioned to enhance the performance of ultra-micro gas turbines manufactured using microfabrication technologies. In this study, the focus is on using wave rotor as topping components for gas turbine cycles.

1.3.1 Gas Turbine Applications

Over the last decades, gas turbines have played a major role in a wide size range of propulsion and power generation systems. A schematic diagram for a simple-cycle, single-shaft gas turbine is shown in Figure 4. It consists of three components: compressor, combustion chamber, and turbine.

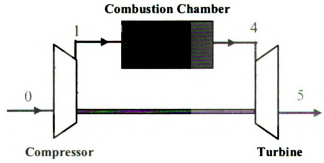

Figure 4: Schematic configuration of a simple gas turbine engine

Air enters the compressor at state "0" and is compressed to some higher pressure. Upon leaving the compressor, the compressed air enters the combustion chamber at state "1" where fuel is injected in a nearly constant pressure process. At state "4", the hot gases enter the turbine where part of their thermal energy is converted into work. In a power generation application, some of the work produced by the turbine is used to drive the

compressor, and the remainder is available as output work produced by the cycle. The expanded gases leave the turbine to the surroundings at state "5".

There are several methods to enhance the performance of gas turbines, including improvement in aerodynamic designs of turbomachinery components or thermodynamic cycle enhancement. The aerodynamics of turbomachinery has already yielded very high component efficiencies up to around 90% [9]. Further improvement is possible, but huge gains seem unlikely. From a thermodynamic point of view, increasing the turbine inlet temperature is the most efficient way to improve both thermal efficiency and output work. For a given engine, this can be achieved by increasing the cycle pressure ratio using a larger compressor. This is shown in a schematic temperature-entropy (T-s) diagram in Figure 5, where an increased pressure ratio has modified the baseline cycle from 0-1_b-4_b-5_b to 0-1-4-5. The numbers on this diagram correspond to the numbers used in Figure 4.

According to the first law of thermodynamics, the cycle net work (W_{net}) is equal to the cycle net heat transfer. Since the cycle with the higher pressure ratio has a greater heat supply (Q_H) with the same heat rejected (Q_L) as the baseline cycle, it has greater output work and also greater thermal efficiency defined by:

$$\eta = \frac{W_{net}}{Q_H} = \frac{Q_H - Q_L}{Q_H} = 1 - \frac{Q_L}{Q_H} \tag{1}$$

However, the maximum temperature of the gas entering the turbine is usually fixed by material considerations. Therefore, cycle 0-1-4-5 has an intolerably high turbine inlet temperature (T_4) much greater than that for the baseline engine (T_{4b}). One innovative solution for this turbine blade temperature limitation is to cool the burned gases by extracting energy from the flow before it enters the turbine. This way, the cycle peak

temperature is de-coupled from the turbine inlet temperature. It can be accomplished by letting the hot gas leaving the combustion chamber compresses the air coming from the compressor, utilizing shock waves in an appropriate geometry. This is the basic principle behind the operation of wave rotors.

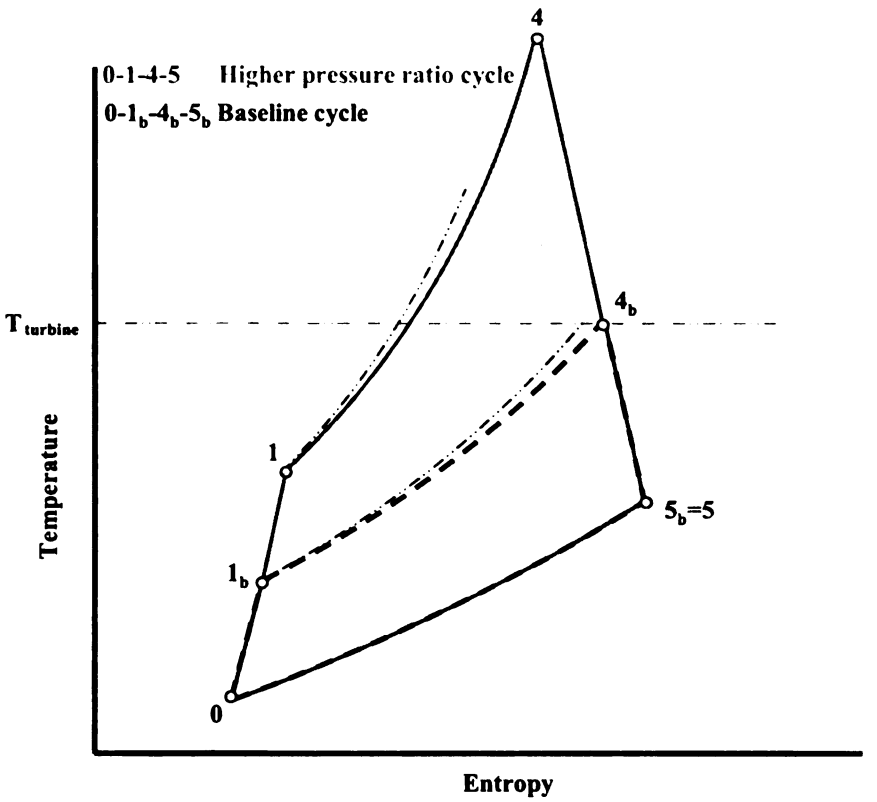

Figure 5: Schematic temperature-entropy diagram for a gas turbine with low and high pressure ratios

- **Wave Rotor Topping Cycles**

In a wave-rotor-topped cycle, the combustion can take place at a higher temperature while the turbine inlet temperature can be equal to that of the baseline cycle. Also, a pressure gain additional to that provided by the compressor is obtained by the wave rotor. Thus, the wave rotor can increase the overall pressure ratio and peak cycle temperature beyond the limits of ordinary turbomachinery. As a result, the performance enhancement

is achieved by increasing both the thermal efficiency and the output work, hence reducing the specific fuel consumption rate considerably. In the following, a four-port wave rotor integrated into a simple gas turbine cycle is selected to prove these facts and its principal operation is briefly discussed

In a conventional arrangement, the wave rotor is embedded between the compressor and turbine "parallel" to the combustion chamber. Figure 6 illustrates how a four-port wave rotor is used to top a gas turbine cycle. Figure 7 schematically shows how the wave rotor can be embedded physically into a baseline engine that uses single stage radial compressor and turbine.

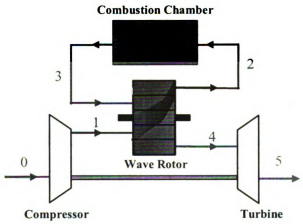

Figure 6: Schematic of a gas turbine topped by a four-port wave rotor

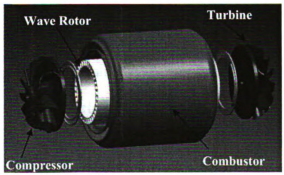

Figure 7: Schematic example of the physical implementation of a wave rotor in a gas turbine (exploded view, piping not shown)

Following the flow path shown in Figure 6, air from the compressor enters the wave rotor (state 1) and is further compressed inside the wave rotor channels. After the additional compression of the air in the wave rotor, it discharges into the combustion chamber (state 2). Here, combustion takes place at a higher pressure and temperature than in the baseline engine. The hot gas leaving the combustion chamber (state 3) enters the wave rotor and compresses the air received from the compressor (state 1). To provide the energy transfer to compress the air, the burned gas expands and is afterward scavenged toward the turbine (state 4). Due to the pre-expansion in the wave rotor, the burned gas enters the turbine with a lower temperature than that of the combustor exit. However, the gas pressure is still higher than the compressor exit pressure by the pressure gain obtained in the wave rotor. The turbine inlet total pressure is typically 15 to 20% higher than the air pressure delivered by the compressor [10]. This pressure gain is in contrast to the untopped engine, where the turbine inlet pressure is always lower than the compressor discharge pressure due to the pressure loss across the combustion chamber. As a result of the wave rotor pressure gain, more work can be extracted from the turbine increasing overall engine thermal efficiency and specific work. Finally, the channels are re-connected to the compressor outlet, allowing fresh pre-compressed air to flow into the wave rotor channels and the cycle repeats.

The general advantage of using a wave rotor becomes apparent when comparing the thermodynamic cycles of baseline and wave-rotor-enhanced engines. Figure 8 shows schematic T-s diagrams of the baseline engine and the corresponding wave-rotor-topped engine. The shown wave rotor implementation is the one most commonly discussed in references, referred to as Case A in this study. It is evident that both gas turbines are

operating with the same turbine inlet temperature and compressor pressure ratio. Each wave rotor investigated in this work has zero shaft work. Therefore, the wave rotor compression work is equal to the wave rotor expansion work. Thus, the energy increase from state "1_b" to "4_b" in the baseline engine and from state "1" to "4" in the wave-rotor-topped engine is the same. This results in the same heat addition for both cycles. However, the output work of the topped engine is higher than that of the baseline engine due to the pressure gain across the wave rotor ($p_{t4}>p_{t4b}$, where subscript "t" indicates total values). Therefore, the thermal efficiency for the topped engine is higher than that of the baseline engine. The inherent gas dynamic design of the wave rotor compensates for the combustor pressure loss from state "2" to "3", meaning that the compressed air leaving the wave rotor is at higher pressure than the hot gas entering the wave rotor.

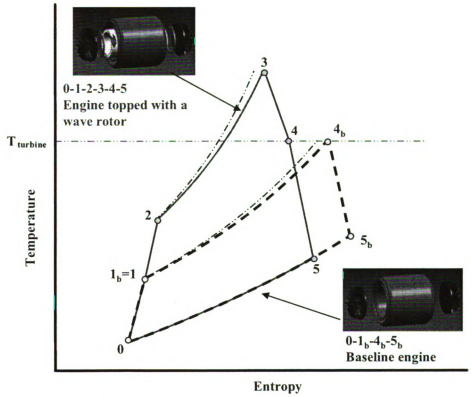

Figure 8: Schematic T-s diagrams for a gas turbine with and without a wave rotor

Other advantageous implementation cases for the wave rotor into the given baseline engine are also possible. Four more advantageous cases have been extensively studied in this work and their advantages and disadvantages will be discussed in detail in Chapter 4.

The goal of this chapter was to introduce the reader to the concept of the wave rotor and its application for gas turbine cycles. Next chapter (Chapter 2) provides a succinct review of past and current research in developing wave rotor technology. Chapter 3 describes the gasdynamic principle behind the operation of wave rotors. In Chapter 4, a comprehensive and systematic performance analysis of two microturbines known as the C-30 and C-60 engines which are topped with a four-port wave rotor in various wave-rotor-topping cycles is presented. Chapter 5 describes an analytical design procedure for the critical high-pressure phase of four-port wave rotors to predict some of their useful design parameters. A CFD simulation is also performed showing that commonly available CFD software FLUENT can be utilized for wave rotor simulations and to support their design. Finally, Chapter 6 introduces and studies several innovative wave rotor concepts and designs including radial-flow wave rotors, integrating wave rotors in ultra-micro gas turbines (UμGT), and water refrigeration systems working with wave rotors.

CHAPTER 2: HISTORICAL REVIEW OF WAVE ROTOR TECHNOLOGY

Recent advances and experiences obtained by the wave rotor community have renewed interest in this technology. These advances include new computational capabilities allowing accurate simulation of the flow field inside the wave rotor, and modern experimental measurements and diagnostic techniques. Improvements in aerodynamic design, sealing technologies, and thermal control methods have been sought. Recent developments in related unsteady flow and combustion processes of pulsed detonation engines have also provoked renewed interest. For this reason it is worthwhile to review the past and current work.[1]

The Early Work (1906-1940)

The earliest pressure exchanger was suggested by Knauff in 1906 in which he did not employ the action of pressure waves [11]. The pressure exchanger introduced by him consisted of a cellular drum that rotates between two end plates containing several ports through which flows with different pressures enter and leave, exchanging their pressure. Knauff initially described rotor channels with curved blades and proposed inclined nozzles in the stator to achieve output shaft power (pressure exchange engine) besides pressure equalization inside the rotor. Reported by Pearson [12], Knauff in his second patent in 1906 [13] and Burghard in 1913 [14] proposed a simpler device in which the pressure exchange takes place in long narrow channel configurations (pressure exchanger) known later as the Lebre machine following Lebre's patent in 1928 [15]. Today, the term "static pressure exchanger" is normally given to this type of device. Around 1928, Burghard proposed the utilization of pressure waves in another invention

[1] Materials presented in this chapter have been accepted for publication in *2004 International Mechanical Engineering Conference, ASME Paper IMECE2004-60082, USA, Nov 2004.*

[16] that was termed the "dynamic pressure exchanger" to distinguish it from the static pressure exchanger. Here, the term "dynamic" implies the utilization of pressure waves in both compression and expansion processes taking place inside the rotor channels. However, difficulties mainly related to poor knowledge about unsteady flow processes limited the dissemination of the dynamic pressure exchanger concept [3] until World War II when Seippel in Switzerland implemented this concept into real engines, as discussed below.

The Comprex® Pressure Wave Supercharger (1940-Present)

Brown Boveri Company (BBC), later Asea Brown Boveri (ABB) and now Alston, in Switzerland has a long history in wave rotor technology. As reported by Meyer [17], their initial investigations in the beginning of the 1940s were aimed at implementing a wave rotor as a topping stage for a 1640 kW (2200 hp) locomotive gas turbine plant of British Railways [18-21]. They expected to obtain a power increase of 80% (2983 kW or 4000 hp) and a 25% efficiency increase (from 18% to 22.5%) based on the patents of Seippel [22-25]. This arrangement is shown in Figure 9. The wave rotor had 30 channels rotating at 6000 rpm, with two opening ports on each side through which air and gas entered and left. It had originally shown a pressure ratio up to 3:1 and total efficiency of 69% in previous tests during 1941-1943, which could approximately result in a 83% efficiency for each compression and expansion process [17].

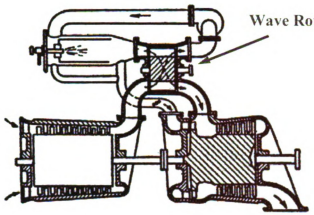

Figure 9: Wave rotor as a topping stage for the locomotive gas turbine, taken from Ref. [17]

The first wave rotor worked satisfactorily, proving the concept of wave rotor machines. However, its performance when installed in the engine was far from expectations, mainly because of its inefficient design and crude integration [20].

Seippel's work also initiated the notion of using the wave rotor as a pressure wave supercharger for diesel engines. The extensive practical knowledge accumulated by BBC during investigations of gas turbine topping cycles was then used to develop pressure wave superchargers first by the ITE Circuit Breaker Company in the US [26-28]. In an effort jointly sponsored by the US Bureau of Aeronautics and ITE supervised by Kantrowitz of Cornell University and Berchtold of ITE, the first units were successfully manufactured and tested on vehicle diesel engines between 1947 and 1955. As a result of this success, a co-operative program with BBC was started in 1955 and BBC decided to concentrate on the development of pressure wave superchargers for diesel engines, due to their higher payoff compared to other applications [29]. As a manufacturer of superchargers, BBC later continued the project in collaboration with the Swiss Federal Institute of Technology (ETH Zurich). While the first prototype was installed in a truck

engine in 1971 [30], the supercharging of passenger car diesel engines was started in 1978 [31, 32] with a first successful test on an Opel 2.1 liter diesel engine [32, 33]. This supercharger was given the trade name Comprex® shown in Figure 10. The port arrangement indicates the use of two operating cycles per revolution, shortening the rotor length and reducing thermal loads. The main advantage of the Comprex® compared to a conventional turbocharger is its rapid response to changes in engine operating conditions where the turbocharger is less responsive, due to its rotational inertia. Furthermore, as the efficiency of the Comprex® is independent of scale, its light weight and compact size make this device attractive for supercharging small engines (below about 75 kW or 100 hp) [34, 35].

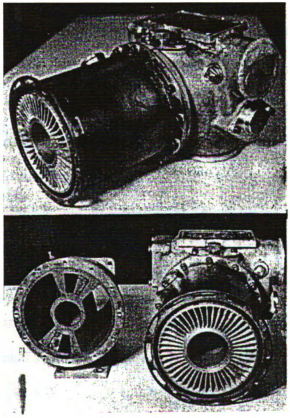

Figure 10: The Comprex®, taken from Ref. [34]

By 1987, the first wide application of the Comprex® in passenger cars occurred in the Mazda 626 Capella [7, 36]. Since then, ABB's Comprex® pressure wave supercharger has been commercialized for several passenger car and heavy diesel engines. For instance, once Mazda produced 150,000 diesel passenger cars equipped with pressure wave superchargers [37]. The Comprex® has also tested successfully on vehicles such as the Mercedes-Benz diesel car [8], Peugeot [29], and Ferrari [29].

The progress by BBC/ABB took almost five decades to accomplish. The successful development of the Comprex® has been enabled by efforts of numerous researchers. Besides the above mentioned names, only some more are listed here: Gyarmathy [6], Burri [38], Wunsch [39], Croes [40], Summerauer [41], Kollbrunner [42], Jenny [43], Keller [44], Rebling [45], and Schneider [46]. Further references related to the development of the Comprex® by BBC [47-60] and other organizations [61-71] until 1990 can be found in the literature. By the end of the 1980s, when the Comprex® activity was transferred to the Mazda company in Japan [3, 72], researchers at ABB turned to the idea of utilizing wave rotor technology for gas turbine applications [9, 73].

During 1990s, a few groups continued the development of pressure wave superchargers. Nour Eldin and his associates at the University of Wuppertal in Germany have developed a fast and accurate numerical method for predicting the unsteady-flow field in pressure wave machines, using the theory of characteristics [74-80]. Piechna et al. at the Warsaw University of Technology in Poland have developed experimentally validated one-dimensional and two-dimensional numerical codes to analyze the flow field inside the Comprex® [81-87]. Piechna has also proposed a compilation of the pressure exchanger with the internal combustion wave rotor, presenting the idea of the

autonomous pressure wave compressor [88]. Oguri et al. at Sophia University in Japan have performed measurements on a car gasoline engine supercharged by the pressure wave supercharger to investigate the feasibility of such integrations [89]. This effort sought to extend the application from diesel engines to gasoline engines and achieved a satisfactory increase of thermal efficiency of the supercharged engines. Guzzella et al. [35, 90-94] at ETH in Switzerland have developed a control-oriented model that describes the entire engine supercharged by pressure wave devices, with special emphasis on the modeling of transient exhaust gas recirculation phenomena. The experimentally validated model has introduced an optimized strategy to operate a supercharged engine with good drivability. Finally, an investigation of Comprex® supercharging on diesel emissions has been recently performed in Turkey [95], demonstrating that the Comprex® has the potential for reducing NO_X in diesel engines.

To date, the Comprex® has been recognized the most successful application of wave rotor technology and represents a practical utilization of the wave rotor concept. The Comprex® development by BBC/ABB also has established fabrication techniques for wave rotors in commercial quantities and considered as a matured and reliable machine for internal combustion engine supercharging. For this application, BBC/ABB has solved difficult development challenges like sealing against leakages, noise, and the thermal stress problems. For instance, enclosing the rotor in a pressurized casing and using a rotor material with a low thermal expansion coefficient over the operating temperature range has kept Comprex® leakages to an acceptable level [29]. Furthermore, several pockets have been cast into the end plates to control wave reflections and to achieve good off-design performance when engine speed changes [59].

In recent years, Swissauto WENKO AG in Switzerland has developed a modern version of the pressure wave supercharger [37]. This new generation of Comprex® known as the Hyprex® is designed for small gasoline engines. It benefits from new control features, enabling higher pressure ratios at low engine speeds, further reduced noise levels, and improvement of the compression efficiency at medium or high engine speeds. The Hyprex® has been successfully demonstrated in the SmILE (Small, Intelligent, Light and Efficient) vehicle which is a modified Renault Twingo, achieving very low specific fuel consumption and low emissions. ETH is collaborating closely in this effort by developing control systems for the proper operation of the device.

Cornell Aeronautical Laboratory and Cornell University (1948-2001)

Inspired by the cooperation with BBC in the late 1940s, work on unsteady-flow concepts was initiated at Cornell Aeronautical Laboratory (CAL). Among several novel concepts including development of energy exchangers for gas turbine cycles and various stationary power applications [96], the CAL Wave Superheater was built in 1958 and utilized until 1969 [21]. The 2 m diameter wave superheater used heated helium as the low molecular weight driver gas to provide a steady stream of high-temperature and high-pressure air for a hypersonic wind tunnel test facility. It compressed and heated air to more than 4000 K and up to 120 atm for run times as long as 15 seconds. Figure 11 is a photograph of this device. The CAL Wave Superheater was a landmark demonstration of the high temperature capabilities of wave rotor devices [21, 96].

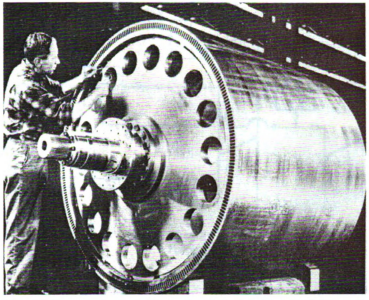

Figure 11: Photograph of the CAL Wave Supercharger, taken from Ref. [5]

Around 1985, Resler, a former member of the CAL Wave Superheater team, resumed the wave rotor research at Cornell University. His efforts and those of his group led to the development of new wave rotor concepts and analytic methods for three-port wave rotor diffusers [97], double wave rotor cycles [98], five-port wave rotors [98-105], and supersonic combustor aircraft engines using wave rotors [106]. Five-port wave rotors have shown significant potential for reducing NO_X in gas turbine engine applications. Figure 12 illustrates a double wave rotor in a gas turbine cycle. The idea of using a compound unit consisting of two (or multiple) wave rotors, one supercharging the other, is also reported in an early German patent by Müller in 1954 [107], as stated by Azoury [34].

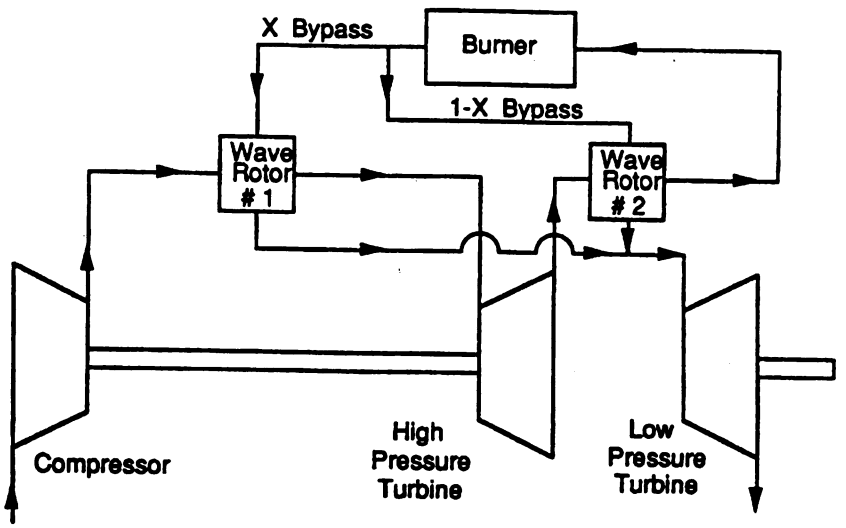

Figure 12: Schematic of a double wave rotor cycle, taken from Ref. [98]

Power Jets Ltd (1949-1967)

In parallel with but independent of Seippel's efforts in 1940s, Jendrassik, former chief engineer of the Gantz Diesel Engine Company of Budapest, was working on the development of wave rotor machines for gas turbine applications [20, 108-110]. He developed one of the first concepts for wave rotor applications to aircraft engines, proposing the wave rotor as a high pressure topping stage for early aircraft engines [111, 112]. His ideas stimulated the government-controlled company of Power Jets Ltd in the UK to become active in the wave rotor field in 1949. Even though the initial intent of Power Jets Ltd was to use wave rotor technology for IC engine supercharging, the interest was later extended to several other applications including air cycle refrigerators, gas turbines, pressure equalizers, and dividers [3, 5, 20, 110]. For instance, two prototype air-cycle refrigerators using wave rotors were designed and employed in gold mines in India and South Africa for environmental cooling purposes. They performed the same duty as equivalent vapor-cycle machines, but with lower weight and bulk. After Jendrassik's death in 1954, theoretical and experimental work continued at Imperial

College, University of London, directed by Spalding and Barnes and also by Ricardo Company in the UK [20, 113]. The experimental divider test rig at Imperial College is shown in Figure 13. Detailed information related to Power Jets Ltd efforts can be found in company reports listed in Ref. [5].

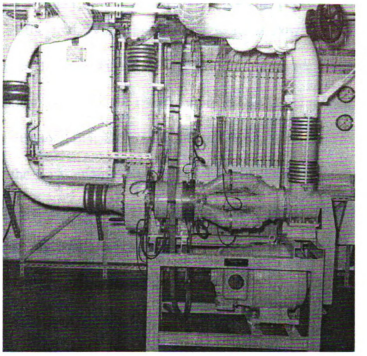

Figure 13: The experimental divider test rig at Imperial College, taken from Ref. [5]

Most of these efforts were experimental and thus expensive. Computational methods and digital computer facilities were too poorly developed in that time, so extensive theoretical methods required to improve the progress were too difficult. Cycle analyses by hand calculations were tedious and impractical. Spearheading the development of CFD methods, Spalding of Imperial College formulated a numerical procedure for wave rotors considering the effects of heat transfer and friction. It utilized novel features to ensure solutions free from instabilities and physical improbabilities [20]. Based on this numerical model, a computer program was developed by Jonsson [114] and it was

successfully applied to pressure exchangers [115-117]. Spalding's students, Azoury [118] and Kentfield [119], continued their efforts on different theoretical aspects of pressure exchangers [3, 5, 20, 34, 110, 117, 120-123] despite the dissolution of Power Jets Ltd in 1967 [20].

Ruston-Hornsby Turbine Company: The Pearson Rotor (Mid 1950s - 1960)

In the U.K. of the mid 1950s, besides the work at Power Jets Ltd and Imperial College, the Ruston-Hornsby Turbine Company, manufacturer of diesel engines and industrial gas turbines, supported the construction and testing of a different kind of wave rotor designed by Pearson [124, 125]. This unique wave rotor, known as the wave turbine engine or simply the wave engine, has helical channels that change the direction of the gas flows producing shaft work similar to a conventional turbine blade. With the financial support by the company, Pearson designed and tested his wave rotor in less than a year, shown in Figure 14.

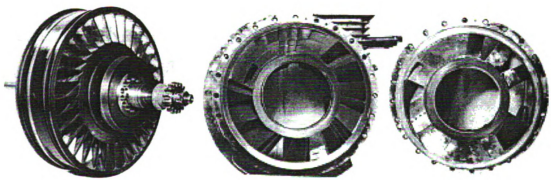

Figure 14: The Pearson rotor (left) and rear and front stator plates (right), taken from Ref. [124]

The rotor has a 23 cm (9") diameter and a 7.6 cm (3") length. The engine worked successfully for several hundred hours in a wide range of operating conditions (e.g., 3000-18000 rpm) without variable porting, and produced up to 26 kW (35 hp) at its

design point with a cycle peak temperature of 1070 K and a thermal efficiency of around 10%. While the performance results were slightly less than the expected design performance (mainly due to the combined effect of excessive leakage and incomplete scavenging), higher performance seemed to be possible with more careful design and development. The design of the engine was based on many wave diagrams using the method of characteristics that accounted for all internal wave reflections. The engine utilized extra ports and injection nozzles to control and cancel unwanted reflected waves. The engine had a length of only one third of its diameter despite having only one cycle per revolution [12]. The sealing and bearings were carefully adapted considering rotor thermal expansion. Unfortunately, the engine was accidentally wrecked due to over speeding from an improperly connected fuel line while the company was suffering financial difficulties. Despite the success achieved, the wave engine experiments were far from the norm of ordinary projects at Ruston-Hornsby and it was considered a redundant project. Tragically, the wave rotor project was canceled when success seemed so close. Further efforts by Pearson to attract additional funding by other sources to commercialize his engine were unsuccessful.

In the history of wave rotor technology, the Pearson rotor and the Comprex® are known as the most successful wave rotor machines developed to date [20, 29, 109]. Both devices have worked efficiently over a wide range of operating conditions, demonstrating good off-design performance although the less-publicized CAL Wave Superheater was an equal success. Nevertheless, the Pearson rotor is a notable wave rotor for producing a significant power output in addition to being a successful pressure exchanger.

General Electric Company (1956-1963)

While Pearson was developing his novel wave engine, General Electric Company (GE) in the US initiated a wave rotor program in 1956 [126]. The work was motivated by earlier work at NASA Langley initiated by Kantrowitz and continued by Huber [127] during the development of a wave engine in the early 1950s and later in 1954-1956 developing pressure gain combustors (constant volume combustion) [126]. GE studied a new configuration of wave rotor in which combustion took place inside the rotor channels (internal combustion wave rotors). Such an arrangement eliminates the need for an external combustion chamber used in the gas turbine cycle, resulting in a significantly lower weight, less ducting, and a compact size. In the period of 1956 to 1959, the methods used at NASA were analyzed, improved and applied to the design and fabrication of the first internal combustion wave rotor demonstrator. As reported by Weber [2], the test rig was first tested at the California Advanced Propulsion Systems Operation (CAPSO) of GE. After 20 seconds of operation, due to the heating and expansion phenomena, the rotor seized between the end plates causing an abrupt stop. The test demonstrated the difficulty of clearance control between the end plates and rotor during thermal expansion. Rotor expansion is an especially challenging problem in the design of wave rotors. While the running clearance between the end plates and rotor must be kept as small as possible, the rotor tends to expand thermally due to hot gases in the rotor. Henceforth, GE resorted to inferior rubbing type seals, and tested only pressure-exchange configurations from 1960 to 1961 [126]. Despite flow leakage, due to the poor sealing method, respectable wave rotor overall pressure ratios of 1.2 to 1.3 were achieved. Meanwhile, a feasibility study was initiated for reducing compressor stages of a T-58 GE-06 engine by using a wave rotor. It showed a considerable reduction in overall

engine weight and cost, and a 15% reduction in specific fuel consumption rate. These results motivated GE further to come up with a conceptual design layout of such an advanced engine. However, further rig experiments revealed other mechanical and aerodynamic shortcomings including start-up, bearing durability, fuel system complications and control [10].

GE also pursued designing a shaft work output wave rotor. Over the period from 1961 to 1963, Klapproth and his associates at GE in Ohio fabricated and tested a wave engine using air-gap seals. An ideal wave diagram of this engine is shown in Figure 15. The engine worked continuously, but it did not produce the anticipated net output power. It is believed that insufficient attention was given to account for internal wave reflections, thus, the flow field calculations were inaccurate [29]. Simplifications were unavoidable at that time and generation of wave diagrams by hand required considerable time and effort and small design changes necessitated a lengthy recalculation. Although the Klapproth rotor did not produce the expected performance, it clearly demonstrated the possibility of the complete exchange of energy within the wave rotor. GE development of the wave rotor was canceled in 1963 due to shifting funds from turbine engine development to space exploration and rocket propulsion [2], and GE's commitment to pursue large engine development exclusively [126, 127].

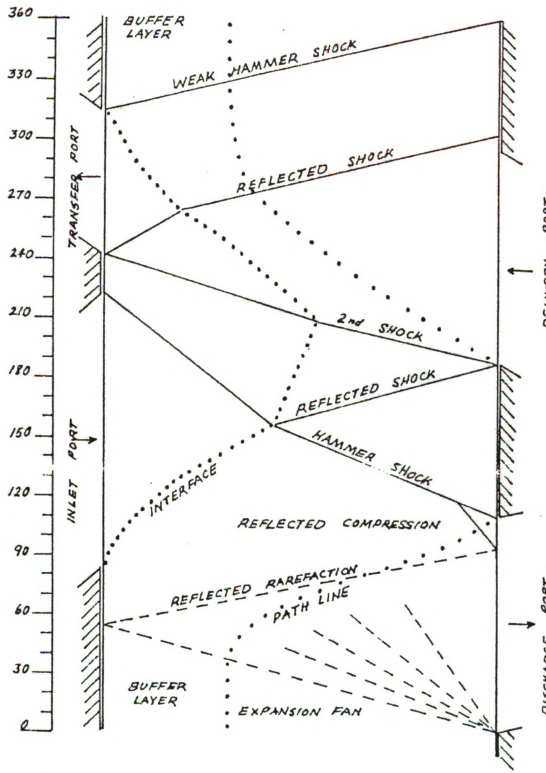

Figure 15: Ideal wave diagram of the Klapproth rotor, taken from Ref. [126]

General Power Corporation (Mid 1960s - 1984)

In the mid 1960s, General Power Corporation (GPC) started a wave rotor program originally intended for a road vehicle engine application [29]. Over a period of about 20 years, GPC spent considerable time and money to successfully design and develop wave rotors. The work was initially supported by Ford Motor Company and later by the Department of Energy (DOE) and the US Defense Advanced Research Program Projects Agency (DARPA). Unfortunately, the GPC work is poorly documented making it difficult to further report about their wave rotor. Some information is briefly reported in Ref. [128]. As stated by Taussig [29, 109], while the GPC rotor shared some of the features of the Klapproth and Pearson rotors, it differed in several aspects taking into account its own unique design and operation. Figure 16 illustrates an ideal wave diagram of the GPC rotor, intended to produce reactive shaft power utilizing curved blades.

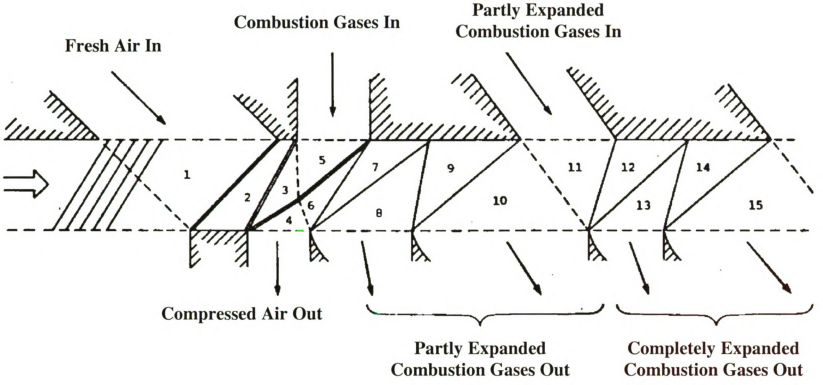

Figure 16: Ideal wave diagram of the GPC rotor, taken from Ref. [109]

There have been reported several difficulties with the GPC design which resulted in poor output power. Its performance suffered from excessive blade curvatures, lack of control of reflected waves within the device required to make the wave system periodic within one revolution, and the absence of any strong impulsive loading of the rotor from inlet manifolds to produce shaft work. The latter was in contrast with the Pearson rotor that relied heavily on impulsive loading of the rotor blades to achieve power output. Furthermore, the GPC rotor had inadequate control on maintaining high performance for off-design operating conditions. Although GPC developed a computer code to obviate manual wave pattern design, accurate calculations were still tedious. Unfortunately Ford ultimately withdrew its support from the wave rotor research before completion of tests, mainly due to commitments to other engine development programs [129]. As a result, GPC discontinued development of the wave engine in the early 1980s.

Rolls-Royce (1965-1972)

In the mid 1960s, Rolls-Royce (RR) in the UK began numerical and experimental wave rotor research [29]. BBC cooperated with RR in the development of pressure exchange wave rotors as topping spools in gas turbine applications [131], with Berchtold of the ETH and Spalding of Imperial College serving as consultants [3]. Considerable efforts were made to design a wave rotor as a topping stage for a small helicopter engine (Allison Model 250) [130]. The BBC-RR engine utilized a reverse-flow wave rotor incorporated into a single turbine cycle. This was somewhat different from the cycle suggested by Berchtold and Lutz [63] in BBC gas-turbine-topping investigations, which employed a through-flow wave rotor integrated with both low-pressure and high-pressure turbines. BBC's interests in wave rotors at that time were mostly related to development of small gas turbines for passenger cars, beset by poor efficiencies at sizes of 100 kW and

smaller [21]. Similar to previous wave rotor efforts, rotor designs protracted manual design methods. While the enhanced engine operated nearly as predicated, measured data revealed low performance mainly due to leakage [29]. Other difficulties related to the start-up and control are reported [10]. The program was abruptly canceled in 1972 amidst severe company financial difficulties [131]. As stated by Kentfield [3], contemporaneous rapid progress in turbomachinery technology may have disfavored high-risk projects, both at RR and GE.

Mathematical Science Northwest Inc. (1978-1985)

In the late 1970s Mathematical Science Northwest Inc. (MSNW, later Spectra Technology Inc., and now STI Optronics Inc.) investigated various applications of wave rotors [21]. Under the sponsorship of DOE and DARPA, they considered a broad range of stationary power systems such as magnetohydrodynamic cycles (MHD) [29], combined cycles integrated with gasification plants [132], pressurized fluidized bed (PFB) power systems [133], and also propulsion and transportation applications [109]. Furthermore, significant numerical and experimental efforts were performed developing a laboratory wave rotor known as the MSNW wave rotor [134-137], shown in Figure 17. With diameter of 45 cm, it consists of 100 channels each with a 40 cm length. It is a four-port wave rotor with two additional small ports provided to cancel pressure waves at critical rotor locations providing more uniform port flows and a higher transfer efficiency [137]. The design rotor speed is reported as 1960 rpm and a pressure ratio of approximately 2.5 was achieved. A measured wave rotor efficiency of 74% is reported [138]. Besides successful tests using several configurations (clearance variations, port sizes, etc.) and various operating conditions, experiments were designed to verify the scaling laws for predicting the performance of larger machines [132].

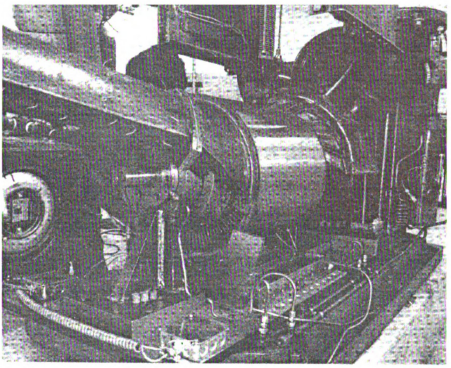

Figure 17: The MSNW experimental set up, taken from Ref. [21]

The MSNW wave rotor was initially designed based on the method of characteristics using only the Euler equations, but later a one-dimensional unsteady computer code (the FLOW code) was used for optimizations and modifications of the MSNW design [109]. The modifications led to improvement in obtaining a very good agreement between the numerical and experimental results in a wide range of operating conditions. Analytic estimations involving the ideal wave patterns also supported the obtained results. The FLOW code which was developed specifically for both pure pressure exchanger wave rotor and wave engine analyses, uses the flux-corrected transport algorithm solving Euler equations accounting for heat transfer, viscosity, gradual port opening, and flow leakage. The sensitivity of wave rotor performance to tip speed, port placement and size, inlet and outlet flow conditions, channel geometry, number of channels, leakage, and heat transfer was analyzed for both on-design and off-design conditions. For instance, it was

outlet flow conditions, channel geometry, number of channels, leakage, and heat transfer was analyzed for both on-design and off-design conditions. For instance, it was concluded that heat transfer losses were negligible and leakage was recognized as a key problem for efficient wave rotor operation. Numerical work has been also reported for a nine-port wave rotor concept to resolve the problem of nonuniform port flows and poor scavenging.

MSNW has used the knowledge obtained through their investigation to establish preliminary wave rotor designs for a small turbofan engine generating 600 lb thrust at sea level condition [109, 138]. A conceptual design of such engine integrated with a pressure exchanger wave rotor is illustrated in Figure 18. Performance calculations for both on-design and off-design flight conditions using a cycle performance code and the FLOW code simulation have predicted significant performance improvements of such an enhanced engine. No new material development for such combined engines was required, proving the possibility of designing such engines by using available technology.

Despite all successful achievements and satisfying results, the wave rotor activity at MSNW was discontinued in the mid 1980s. No specific reasons for this cancellation are reported.

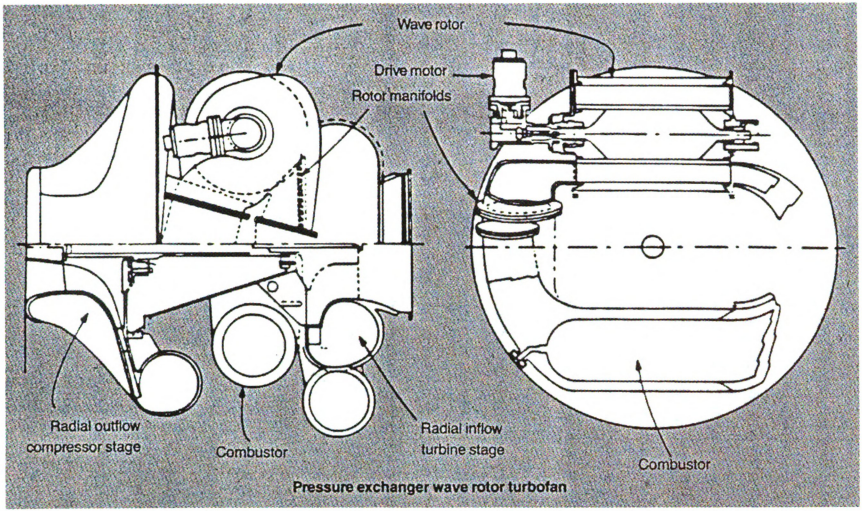

Figure 18: Conceptual design of a turbofan engine incorporating a wave rotor, taken from Ref. [138]

Naval Postgraduate School (1981-1986)

In 1981, the Office of Naval Research (ONR) agreed to monitor a joint DARPA/ONR program to evaluate the wave rotor concept and its potential application in propulsion systems [127]. Following this decision, Turbopropulsion Laboratory (TPL) at Naval Postgraduate School (NPS), directed by Shreeve, started an extensive numerical and analytical wave rotor program. To support the accuracy of the computational results, the wave rotor apparatus formerly used by Klapproth at GE was transferred to TPL and some preliminary tests were carried out. It is reported that the rotor produced some shaft work running at approximately 5000 to 6000 rpm [139]. No further experimental details are reported.

For numerical simulations, two different approaches to the solution of the unsteady Euler equations were examined in the overall program. First, Eidelman developed a two-dimensional code based on the Godunov Method to analyze the flow in wave rotor channels [140-143]. Unlike contemporary one-dimensional approaches [144], the two-dimensional code showed the effect of gradual opening of the channels. The main conclusion of these studies is that if the channels are straight, the flow remains nearly one-dimensional, which in turn leads to minimal mixing losses caused by rotational flow in the channels [145]. However, when the channel of the wave rotor is curved, even an instantaneous opening of the channel does not lead to the development of a one-dimensional flow pattern with small losses. Computation time of such a two-dimensional code has been reported to be quite long. For faster computations, a one-dimensional, first order time-accurate code was introduced by Mathur based on the Random Choice Method for solving the Euler equations [146, 147]. The unconditionally stable code, called WRCOMP (wave rotor component), calculated the unsteady-flow process inside

the wave rotor, inlet and outlet opening times and other useful design parameters required for a preliminary design. The outputs from WRCOMP are used in a second program, called ENGINE, for turbofan jet engine performance calculations [148-150]. The results confirmed the significant performance improvement expected by integrating a wave rotor into a turbofan engine. Work was planned toward incorporating the effects of friction and heat transfer into WRCOMP and also including other engine configurations in the ENGINE code. Some improvements to the WRCOMP code were later started [151, 152], but further development was not pursued after terminating the wave rotor research around 1986.

It is also worth to point out that NPS sponsored the most comprehensive wave rotor conference in 1985 where worldwide participation in this conference took place [153]. The conference reviewed much of the history to that point.

NASA Glenn Research Center (1990-Present)

Since the late 1980s, a sustained research program at NASA Lewis (now Glenn) Research Center (GRC), collaborating with the US Army Research Laboratory (ARL), Rolls-Royce Allison has aimed to develop and demonstrate the benefits of wave rotor technology for future aircraft propulsion systems [10].

In 1993, using a thermodynamic approach to calculate the thermal efficiency and specific power, Wilson and Paxson [154] published a feasibility study for topping jet engines with wave rotors. Applied to the case of an aircraft flying at Mach 0.8, they have shown that a wave-rotor-topped engine may gain 1...2% in efficiency and 10...16% in specific power compared to a simple jet engine with the same overall pressure ratio and turbine inlet temperature. Additionally, Paxson developed a quasi-one-dimensional gasdynamic model to calculate design geometry and off-design wave rotor performance

[155, 156]. The code uses an explicit, second order, Lax-Wendroff type TVD scheme based on the method of Roe to solve the unsteady flow field in an axial passage for time-varying inlet and outlet port conditions. It employs simplified models to account for losses due to gradual passage opening and closing, viscous and heat transfer effects, leakage, flow incidence mismatch, and non-uniform port flow field mixing.. In order to verify wave rotor flow predictions and to assess the effects of various loss mechanisms [157, 158], a three-port wave-divider machine was constructed and tested [159-161] in a new wave rotor laboratory facility at GRC. Concurrently, the non-ideal behavior and losses due to multi-dimensional effects were studied by Welch [162-164] and Larosiliere [165-167]. Welch has also established macroscopic and passage-averaged models to estimate the performance enhancements of wave rotors [168, 169]. Based on experimental data, Paxson further improved the one-dimensional model [157, 158, 170, 171] and used it to evaluate dynamic behavior, startup transients, and channel area variation [172-175]. This model was then used as a preliminary design tool to evaluate and optimize a four-port wave rotor cycle for gas turbine topping [176]. This through-flow cycle was chosen based on several perceived merits, including relatively uniform rotor temperature, and the feasibility of integration with gas turbomachinery. As a result of these studies, a new four-port wave rotor was designed and built [177] to test the performance of this concept under scaled laboratory conditions. A photograph of NASA four-port wave rotor is shown in Fig. 16. However, a study by Rolls-Royce Allison discussed below indicated that thermal loads on the rotor and ducting predicted for the NASA wave rotor cycle in real engine conditions may be difficult to manage. In

response, Nalim and Paxson [178, 179] proposed an alterative cycle with a combustor bypass significantly lowering thermal loads.

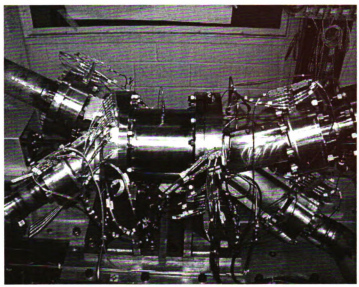

Figure 19: Four-port wave rotor of NASA

Additional studies of the performance benefits of wave rotor topped gas turbines have been reported. In 1995, Welch et al. [180] predicted a 19…21% increase in specific power and a 16...17% decrease in specific fuel consumption compared with the baseline engines in performance calculations for small (300 to 500 kW) and intermediate (2000 to 3000 kW) wave-rotor-enhanced turboshaft engines. The same calculations for a wave-rotor-enhanced large turbofan engine, equal in thrust to the baseline engine, have shown a 6…7% reduction in thrust specific fuel consumption. Welch has also studied the possibility of curving the channels to create a wave turbine [181, 182].

In 1995, Nalim at NASA published a feasibility assessment of combustion in the channels of a wave rotor, for use as a pressure-gain combustor [183]. Combustion prediction capability was added to the wave rotor code by Nalim and Paxson [184],

enabling the exploration of wave cycles involving both detonation and deflagration modes of combustion. For uniform mixtures, a single reaction progress variable is utilized. Multiple species are represented for a variable fuel-air ratio in deflagration modes. Mixing controlled reaction is combined with a simple eddy diffusivity model. Other notable features that were incorporated are temperature kinetics factors and a simple total-energy based flammability limit [185]. The performance of detonative and deflagrative cycles was studied by combined CFD and system simulation. It was determined that deflagrative combustion with longitudinal fuel stratification could be accomplished over a reasonable time in wave rotors.

The current NASA wave rotor research has been mostly focused on experimental tests with special attention to sealing technology [186-188], identified as a critical challenge in high-pressure wave rotor design.

Rolls-Royce Allison (1990-Present)

In 1996, Snyder and Fish [189, 190] of Allison Engine Company evaluated the Allison 250 turboshaft engine as a potential platform for a wave rotor demonstration, predicting an 18...20% increase in specific power and a 15...22% decrease in specific fuel consumption. They used a detailed map of the wave rotor cycle performance accomplished by Wilson and Paxson [10, 154, 176]. Allison (by now Rolls-Royce Allison) has also studied transition duct designs for integration with turbomachiney [191, 192]. This was later followed by investigations of pulse detonation wave rotors in the newly formed Allison Advanced Development Company (AADC). A novel four-port device is proposed [193] for supersonic turbofan engines [194], and was investigated in collaboration with Indiana University Purdue University Indianapolis (IUPUI) as discussed later.

University of Florida (1992-1998)

Motivated by NASA wave rotor successes, Lear at the University of Florida initiated analytical and numerical methods to investigate different configurations of wave rotors. His team developed an unsteady two-dimensional numerical code using a direct boundary value method for the Euler equations to analyze the flow in wave rotors and their adjoining ducts, treating the straight or curved channel walls as constraints imposed via a body force term [195]. The code was later used to simulate the flow field of the three-port NASA wave rotor. They also introduced a preliminary design method for selecting the wave engine inflow and outflow blade angles. Furthermore, an analytical thermodynamic description of wave rotors was developed [196], which predicted potential increase in specific power of 69% and a 6.8% increase in thermal efficiency over a conventional gas turbine topped by a wave engine. A parametric study of gradual opening effects on wave rotor compression processes is reported, too [197].

ONERA in France (1995-1999)

Fatsis and Ribaud at the French National Aerospace Research Establishment (ONERA) have investigated wave rotor enhancement of gas turbines in auxiliary power units, turboshaft, turbojet, turbofan engines [198, 199], accounting for compression and expansion efficiency, as well as mixing and pressure losses in the ducting. Their results show the largest gains and efficiency for engines with a low compressor pressure ratio and high turbine inlet temperature, such as turboshaft engines and auxiliary power units. These results are consistent with those obtained by NASA GRC [200]. They hve also developed a one-dimensional numerical code based on an approximate Rieman solver taking into account viscous, thermal, and leakage losses [198, 201], and applied it to three-port, through-flow, and reverse-flow configurations.

- **Recent Academic Work**

Besides ongoing research mainly at NASA, AADC, and ETH Zurich, a few universities have been conducting wave rotor research. To the knowledge of the author, the universities listed below are are active in this field.

Purdue School of Engineering and Technology (1997-Present)

Recent research at Indiana University Purdue University Indianapolis (IUPUI) by Nalim and coworkers has focused on internal combustion wave rotors, following the initial work at NASA described above. Deflagrative combustion with longitudinal fuel stratification has yielded a wave rotor geometry competitive with pressure-exchanger designs using a separate combustor [185, 202]. Nalim has highlighted the importance of thermal management of leakage flows of rotor and end-wall temperatures, with illustration of the impact of the hot ignition gas and the cold buffer zones on the end walls. This is consistent with the major challenges revealed by the ABB experiment [73]. Radial stratification [203] using a pre-combustion partition has been proposed to introduce a relatively cooler buffer zone close to the leakage gaps, reducing hot gas or fuel leakage to the rotor cavity. Figure 20 is a contour plot of the temperature contour from a simulation of deflagrative combustion in a stoichiometric partition region propagating into a leaner mixture in the main chamber. Above and below the partitions, there is no fuel, and gas may leak out or in without danger of overheating or pre-ingnition. These thermal management approaches are possible utilizing extensive cycle design studies and analysis, and seek to alleviate the challenges previously recognized by ABB and NASA. This technique also helps burn leaner mixtures, resulting in reduced NO_X emissions, similar to other pilot combustion or lean-burn techniques in conventional engines [204]. For this approach, radial leakage flows [205] and different combustion

models [206] have been studied in detail. These ideas have not yet been tested experimentally.

Figure 20: Temperature distribution of partition exit flow, taken from Ref. [204]

Detonative combustion cycles for propulsion engines have been also studied [207, 208]. Interest in detonative combustion initially focused on pulsed detonation engines (PDE) has evolved to the consideration of the wave rotor as an effective implementation of the concept [209], and a means of overcoming challenges to PDE concepts that involved integration with conventional turbomachinery. In effect the wave rotor provides automatic high-speed valving, nearly steady inflow and outflow, and the use of one or few steady ignition devices for multiple tubes. However, detonative combustion is fundamentally restricted to highly energetic mixtures and sufficiently large passage widths, and generates strong pressure waves. This results in the outflow being highly non-uniform in pressure, velocity, and possibly temperature. To better utilize the output of a wave rotor PDE, it has been proposed to add an ejector element to the wave rotor [210]. The rotary wave ejector admits bypass air after the detonation tubes to transfer energy and momentum. Numerical simulations using a quasi-one-dimensional code, modified to account for radial-type bypass flows, have shown that the specific impulse at static thrust conditions can be doubled, after accounting for flow-turning and shock losses, comparing with an equivalently loss-free PDE cycle. A sample wave diagram and

a schematic sketch are given in Figure 21, where the cold ejector gas flow is clearly distinguishable.

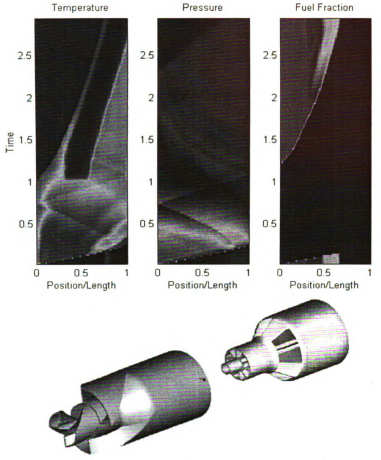

Figure 21: Rotary Wave Ejector Pulse Detonation Engine, taken from Ref. [210]

IUPUI has also investigated [211] the four-port detonation wave rotor proposed by AADC [193], in which a recirculation duct allows air that is compressed by the shock of a detonation wave to be reinjected with fuel. Air-buffer regions both between the fuel/air-combusted gas interface and at the exit end plate are inherent in the cycle design, allowing self-cooling of the walls. The inflow and outflow of this engine concept is designed to be nearly uniform and acceptable to modern turbines, compared to conventional rotary detonation cycles, as shown in Figure 22.

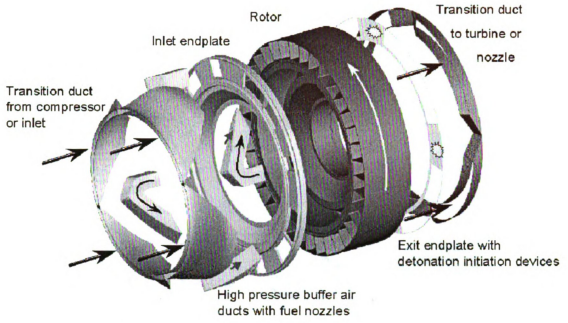

Figure 22: Wave Rotor PDE the 'CVC' Engine, taken from Ref. [211]

A computational and experimental program is currently being conducted at IUPUI in collaboration with AADC to investigate the combustion process and performance of a wave rotor with detonative and near-detonative internal combustion [212]. A preliminary design method based on a sequence of computational models has been developed to design wave processes for testing in an experimental test rig.

University of Tokyo (2000-Present)

Nagashima et al. have developed one-dimensional [213] and two-dimensional [214] CFD codes to simulate the flow fields inside through-flow four port wave rotors, including the effects of passage-to-passage leakage. The codes have been validated with experimental data obtained by a single-channel wave rotor experiment Single-cell experiments can efficiently demonstrate the operation of actual wave rotor engines. The test rig, shown in Figure 23, consists of a stationary single tube, and two rotating plates connected to a shaft driven by an electric motor. This group has also explored the idea of

using wave rotors for ultra-micro gas turbines manufactured using microfabrication technology [215].

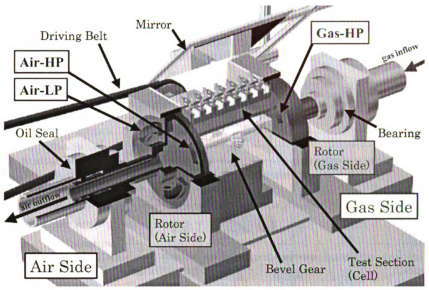

Figure 23: University of Tokyo single-channel test rig, taken from Ref. [214]

In conclusion, Figure 24 summarizes the history of the wave rotor research reviewed here. The goal of this review was to report the continued interest in wave rotor technology and its wide variety of applications. Some of the latest efforts were discussed in more detail, inspiring further research and development on this topic

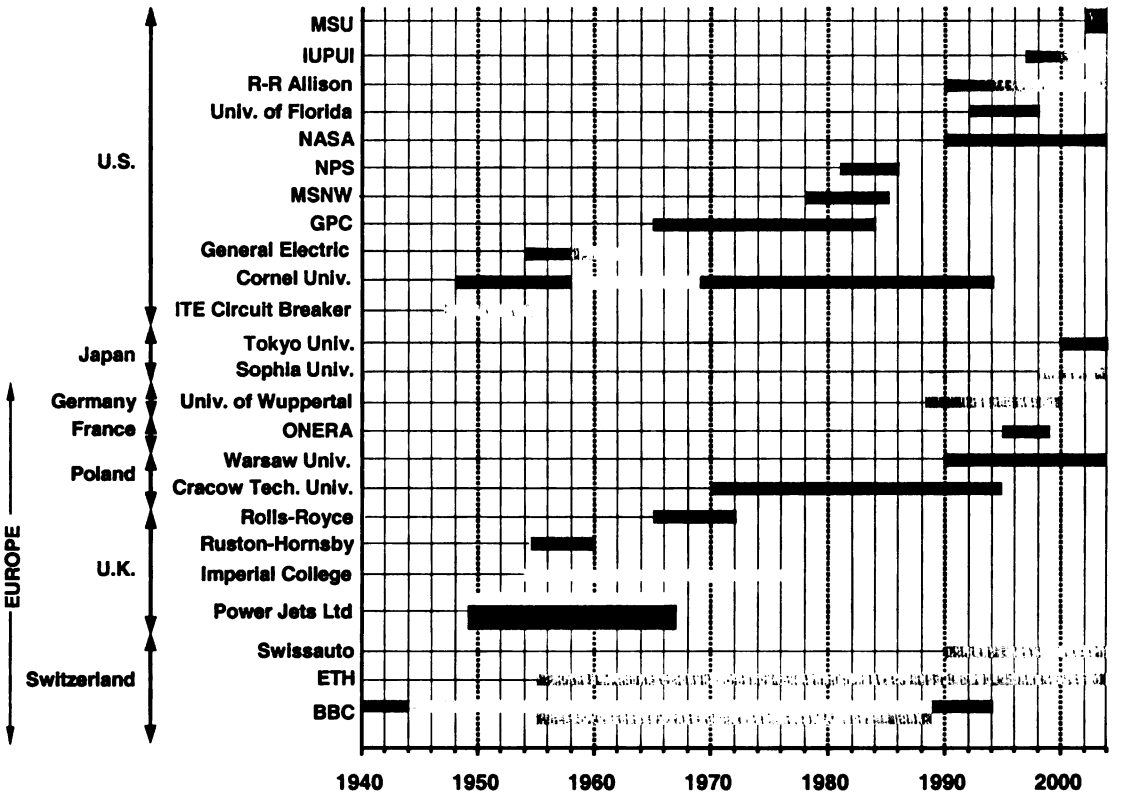

Figure 24: Historical perspective of wave rotor technology. Red: gas turbine application, Green: IC engine supercharging, Blue: refrigeration cycle, [illegible], Black: general applications

CHAPTER 3: WAVE ROTOR THEORY

3.1 Energy Exchange with Waves

To understand the principle of wave rotor operation, it is more convenient first to analyze wave processes that occur in a single stationary channel. This is very similar to analyzing gasdynamic processes in shock tubes. Figure 25 schematically shows a shock tube and its corresponding wave diagram (time- space diagram). The wave diagram describes the wave action by tracing the trajectories of the waves and gas interfaces. It is a plot of the wave motion as a graph of time verses space.

When the diaphragm which has separated two gases at different pressures is ruptured, two types of gasdynamic waves are initiated at the diaphragm location. A shock wave propagates into the low-pressure gas (driven section) and an expansion wave spreads out into the high-pressure gas (driver section). The shock wave increases the pressure and temperature of the driven section rapidly and induces a mass motion behind itself. The interface between the driver and driven gases, called the contact surface, moves with an induced velocity in the same direction as the incident shock. The expansion wave decreases the pressure and temperature of the driver section smoothly. Therefore, across the contact surface the pressure and velocity are preserved while the temperature and entropy change discontinuously.

Now, consider a closed tube which is initially sealed on both ends and contains a gas at rest, as shown in Figure 26. The rapid opening of one end of the tube to a higher or lower pressure media can initiate waves in the tube similar to the rupturing of the diaphragm in a shock tube, as it will be described in the following. Two cases are

introduced here utilizing the principle of shock tube operation to increase or decrease the pressure and temperature of the gas inside the tube.

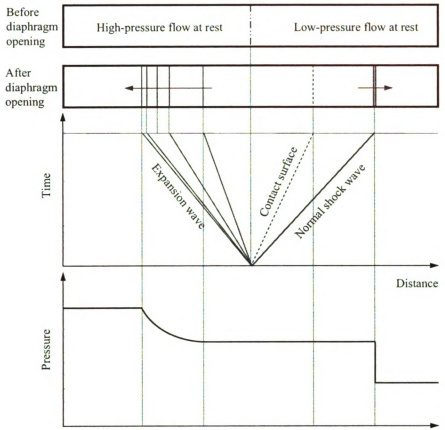

Figure 25: Flow in a shock tube after the diaphragm is ruptured

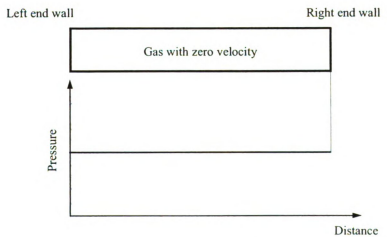

Figure 26: Closed tube containing stationary gas

- **Generation of a Shock Wave**

Assume it is aimed to increase the pressure and temperature of the gas trapped in the tube. This can be achieved by the rapid opening of one tube end to a medium with a higher pressure. When the tube opens instantaneously to a high-pressure gas, a shock wave forms and propagates into the channel as shown in Figure 27. This simulates the compression process of the driven section in the shock tube by suddenly removing the diaphragm.

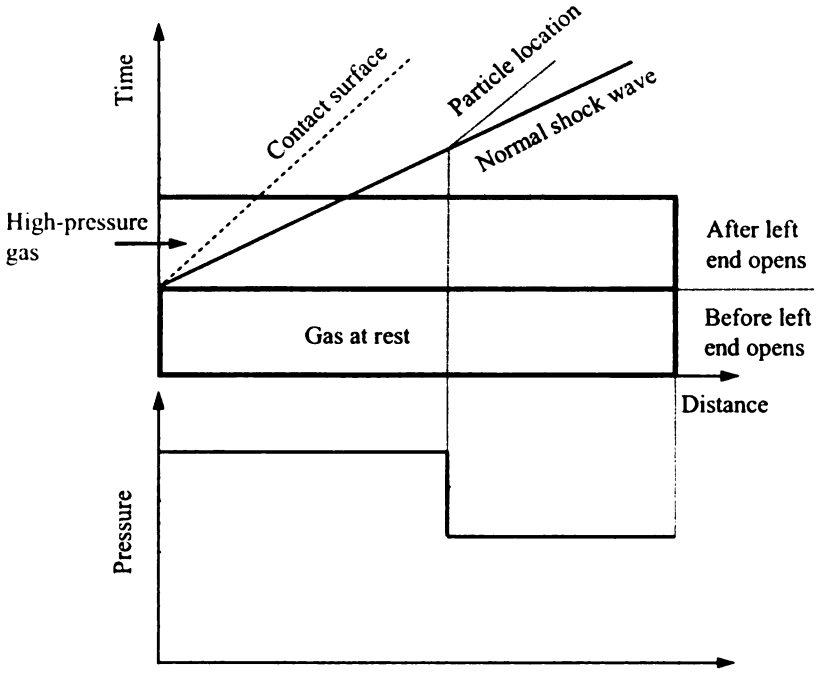

Figure 27: Left end opening to gas at higher pressure

- **Generation of an Expansion Wave**

To decrease the pressure and temperature of the trapped gas, one end of the tube is opened to a gas with a lower pressure than the pressure in the tube, as depicted in Figure 28. Rapid opening of one end of the tube results in the formation of a centered expansion fan which propagates into the tube, inducing a gas flow out of the tube. Such a

scavenging flow process imitates the expansion process of the driver section in a shock tube after sudden removal of the diaphragm.

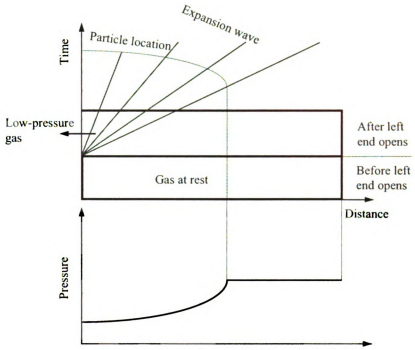

Figure 28: Left end opening to gas at lower pressure

In the operation of wave rotors, shock and expansion waves may also be generated in other ways. As an example, consider a case where a gas is flowing through a tube at a steady rate as shown in Figure 29. Suddenly closing one end of the tube can generate either a shock wave or an expansion wave. Figure 30 illustrated how an expansion wave can be generated by rapidly closing the left end of the tube. Because the velocity of the gas in contact with the closed end must be zero, an expansion wave propagates into the moving gas, bringing it to rest. Also, the pressure and temperature inside the tube drop depending on the strength of the expansion wave, reducing the flow velocity to zero. Using the same concept, suddenly closing the right end of the tube results in the

generation of a shock wave. This is shown in Figure 31. The shock wave propagates in the tube from right to left increasing the pressure and temperature inside the tube.

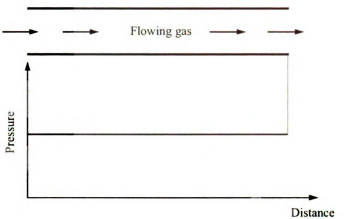

Figure 29: Opened tube containing flowing gas

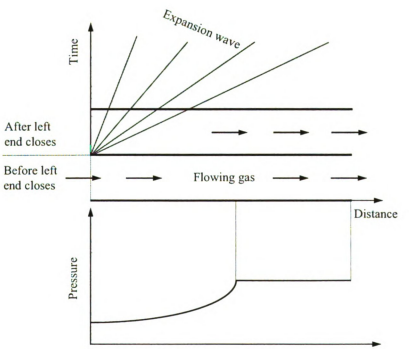

Figure 30: Left end closing to generate an expansion wave

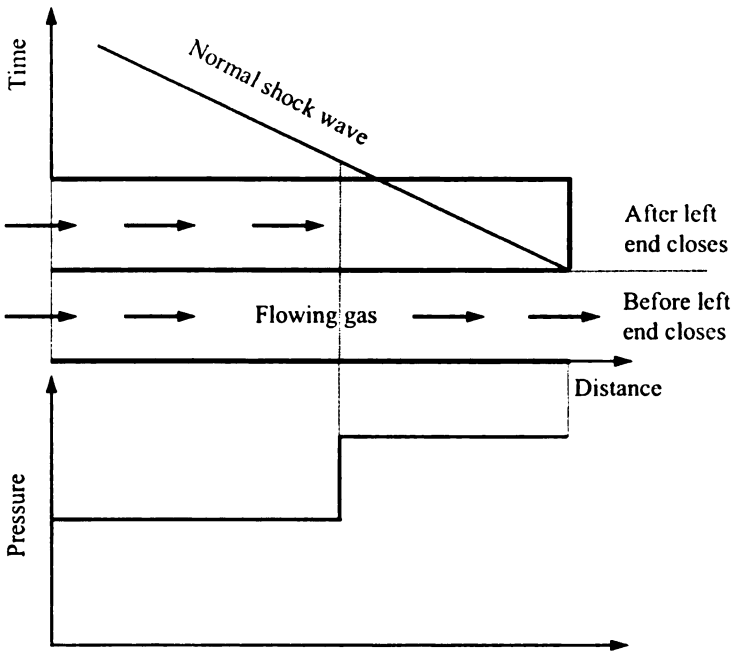

Figure 31: Right end closing to generate a shock wave

3.2 Charging Process in Wave Rotors

The above gasdynamic phenomena can be used in an array of rotating shock tubes (wave rotors) to increase the pressure and temperature of a flow by expanding another flow which has a higher pressure and temperature. Several configurations can be introduced for this purpose, but only two of them are briefly discussed here.

Figure 32 shows a developed (unwrapped) view of the charging process of a wave rotor. This figure shows a sequence of events occurring within the channels moving in the upward direction. Such a representation is called a wave diagram. The wave process occurring inside the wave rotor channels is customarily illustrated by the wave diagram, where the circular motion of the rotor channels is replaced by a straight translatory motion. It describes the rotor internal operation by tracing the trajectories of the waves and gas interfaces. The wave diagram is very useful for visualizing the wave process occurring inside the channels and also for determining wave rotor design parameters, i.e.,

port opening and closing times and their locations. The utility of the wave diagram is analogous to that of a velocity diagram for a conventional turbine or compressor. In Figure 32, the ducts are set at the correct angle, so that in the rotor reference frame the flow can enter and leave the rotor aligned with its axis. The shock wave trajectory is shown by a dashed line. The trajectory of the interface line is indicated by a dotted line.

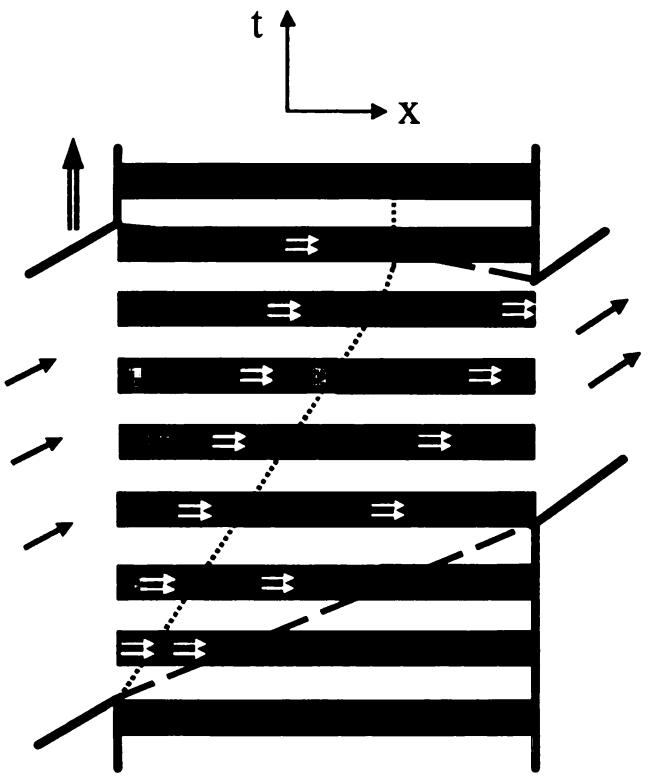

Figure 32: Wave diagram of charging process with two primary shock waves

The process begins in the bottom part of Figure 32, where the channel is closed at both ends and contains low-temperature and low-pressure flow (e.g., air). When the inlet port opens, the rotor channels are exposed to a high-pressure and high-temperature gas arrived from a heat source (e.g., the combustion chamber). This hot driver gas penetrates the channel. Because its pressure is higher than the pressure in the channel, a shock wave

is triggered starting from the lower corner of the inlet port. The shock wave runs through the channel and causes an abrupt rise of local pressure inside the channel. The shock wave speed is higher than the local speed of sound. Within the relevant design space the flow speeds are everywhere subsonic. Therefore, the air/gas interface follows the shock wave with an induced velocity less than the speed of sound. However, behind the shock wave the compressed air has the same local pressure and speed as the inlet driver gas. As the shock wave reaches the end of the channel, the outlet port opens through which the compressed air is then pushed out. At this moment, both the gas and the compressed air column in the channel have the same local pressure and move uniformly with the same induced velocity toward the outlet port. By closing the outlet port, a second primary shock wave originates from the upper outlet edge and propagates from the right to the left. It reduces the velocity of the compressed air to zero to satisfy the zero-slip boundary condition at the end wall. The process is finished when the gas inlet port closes. The moment is timed with the arrival of the secondary shock wave to the upper corner of the inlet port.

While the charging process described above is theoretically feasible, it is rarely used in wave rotor designs. Even though the second primary shock wave compresses the air further, the doubly compressed air is not delivered to the outlet port. This may lead to overheating of the channels. Hence, the second primary shock wave has been only generated to stop the compressed air. Therefore, another type of charging processes utilizing an expansion wave is often preferred. This configuration is shown in Figure 33 where the flow is stopped by closing the gas inlet port. This way, an expansion wave originates from the upper corner of the gas inlet port and propagates toward the right end

of the channel. Expansion waves (fans) are depicted by thin solid lines. Since this expansion wave induces a flow velocity equal but opposite to that of the gas flow, the gas flow behind this expansion wave is stopped and its local pressure is decreased. Both local and total pressures behind the expansion wave are still considerably higher than the pressure of the fresh air in the beginning of the process. The speed of the expansion wave with reference to the channel wall is equal to the gas speed plus the local speed of sound. As a result, the expansion wave is traveling faster than the air/gas interface, overtaking the air/gas interface before the latter reaches the right end of the channel. The expansion wave reaches the end of the channel at the moment when the upper edge of the outlet port closes the channel. At this moment, the trapped flow within the channel consists of a large part of the hot gas and a plug of compressed air preventing the hot gas to contact the end wall. Thus, during the high-pressure process, penetration of the hot gas into the outlet flow is avoided.

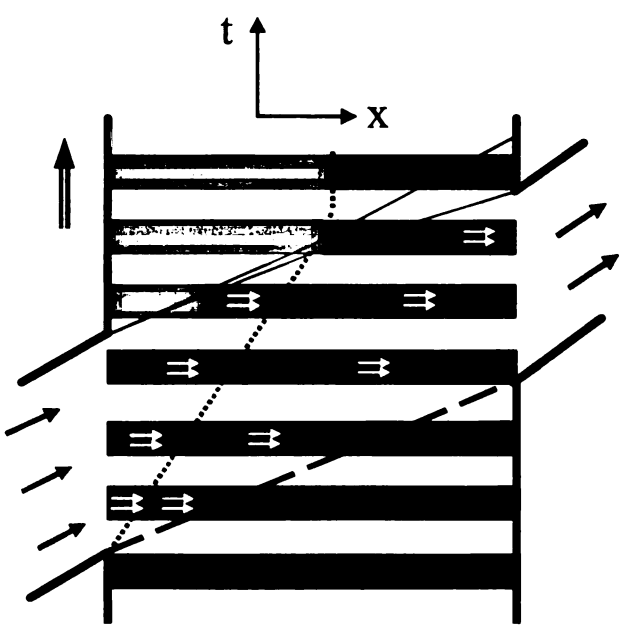

Figure 33: Wave diagram of charging process using single shock wave and expansion wave

3.3 Principles of Four-Port Wave Rotor Operation

A variety of wave rotor configurations have been developed for different applications. The number and azimuthal location of the wave rotor ports along with heat addition schemes distinguish them for different purposes. As described in the previous chapter, four-port configurations have been mainly used as superchargers for internal combustion engines. Three- port wave rotors have been employed in pressure dividers and pressure equalizers in which the pressures of different fluids are increased or reduced. Two-port, four-port, five-port, and nine-port wave rotors have been extensively investigated for gas turbine engine topping applications. As an application of current interest, a four-port wave rotor integrated into a gas turbine cycle is briefly discussed below to illustrate wave rotor operation and options.

3.3.1 Through-Flow versus Reverse-Flow Wave Rotors

In the described wave rotor illustrated in Figure 6, both gas and air inlet ports are located on one side of the rotor while the outlet ports are located on the other side of the rotor. This configuration is known as the through-flow (TF) wave rotor in the literature. Alternatively, another type of wave rotor has been designed where the fresh air enters and exits at the same end of the rotor (air casing) while the burned gas enters and exits the rotor at the other end (gas casing). This configuration is called reverse-flow (RF) wave rotor as shown in Figure 34. These two configurations may provide identical topping and overall performance enhancement, but they differ substantially in their internal processes.

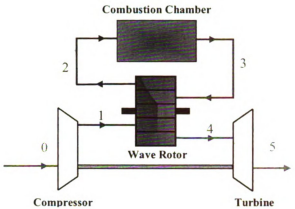

Figure 34: Schematic of a gas turbine topped by a reverse-flow four-port wave rotor

In a TF four-port wave rotor, both hot gas and relatively cold air traverse the full length of the rotor, keeping the wall at a relatively uniform intermediate temperature. This self-cooling feature of TF wave rotors has prompted interest in them for gas turbine engine topping applications where gas temperatures are high. The RF configuration does not inherently result in such a self-cooled rotor. The cold air never reaches the other end of the rotor as seen from Figure 34. As a result, the air side of the rotor is relatively cool while the gas side of the rotor is relatively hot. To achieve a better self-cooled RF design, a mirrored reverse-flow cycle design of the RF configuration can be constructed, which orients the cycle alternately right and left on the rotor [189]. This approach introduces symmetry and assures that both sides of the rotor are washed by the relatively cold fresh air. Unfortunately, it also poses severe ducting challenges. However, for small gas turbines the gas temperatures are often lower than those of large scale gas turbines. Therefore, the RF approach seems to be the viable choice for microturbines. Also, it has been claimed that the RF cycle provides better separation of air and gas in the rotor channels [2]. Due to this separation of air and gas regions in the channels, the analysis of the fluid flow inside RF wave rotor channels is easier. Knowing about all these facts, RF

configurations have been mostly used in the relatively low-temperature application of car engine supercharging although such configuration for gas turbines has been also investigated [131, 189, 198]. The General Electric Company has obtained experimental data on a gas turbine engine enhanced by a RF wave rotor [126].

3.3.2 How Does it Work Inside?

Figure 35 represents NASA wave diagrams [168] for through-flow (left) and reverse-flow (right) four-port wave rotors for one cycle operation of the rotor. The journey of a channel of the wave rotor is periodic. The top of each wave diagram is considered to be looped around and joined to the bottom of the diagram. This requirement presents a fundamental challenge in the simulation and design of wave rotors. A successful prediction of the wave rotor implies that the state of the working fluid in the channel at the end of the cycle must be the same as that postulated at the beginning of the cycle.

To show how a four-port wave rotor works, the events occurring in one cycle are now described. For the RF configuration, the process begins in the bottom part of the right wave diagram where the flow within the channel consists of a large part of the hot gas and a buffer layer separated by a contact surface. For the TF wave rotors (left), the gas fills the whole channel. As the right end of the channel opens to the relatively low-pressure outlet port, an expansion fan originates from the leading edge of the outlet port and propagates into the channel, discharging only the gas to the turbine. The expansion fan reflects off the left wall and reduces the total pressure and temperature in the channel further. This draws fresh air provided by the compressor into the channel when the air inlet port opens. When the reflected expansion fan reaches the outlet port, it slows the outflow and reflects back as compression waves, while the outlet port closes and halts the flow inside the channel. The compression waves form a single shock wave as they travel

toward the inlet port. As the shock wave reaches the upper corner of the inlet port, it closes gradually. At this moment, the channel fluid is at rest relative to the rotor.

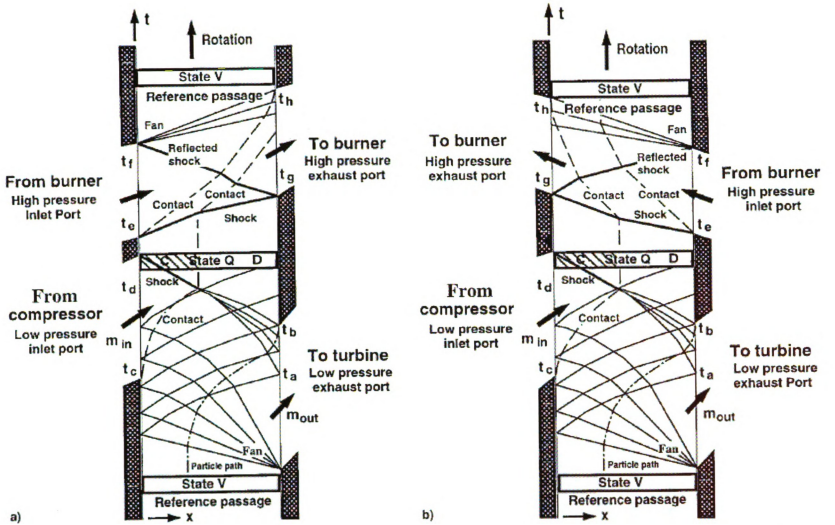

Figure 35: Wave diagrams for through-flow (left) and reverse-flow (right) four-port wave rotors, taken form Ref. [168]

The above sequence of events is called the low-pressure part of the cycle (scavenging process). Its purpose is to deliver a high-pressure gas into the turbine, partially purge the rotor channels, and ingest fresh air received from the compressor. In the high-pressure part of the cycle (charging process) that follows, the rotor channels are exposed to the burned gas arrived from the combustion chamber. The wave phenomena here are same as those described in Figure 33. The only difference here is the existence of a reflected shock wave in the NASA wave diagram. In fact, as the shock wave reaches the end of the channel and the outlet port opens a reflected shock wave originates at the lower outlet edge, propagating back into the channel. The reflected shock wave compensates for the combustor pressure loss. On the other hand, for an ideal combustion chamber (no pressure loss), the reflected shock wave would not appear. This has been shown in Figure 77 which is discussed later. The double-compressed flow behind the reflected shock wave leaves the wave rotor toward the combustion chamber. In the RF configuration the discharged flow into the burner is pure air, while in the TF configuration usually both air and once-burned gas are delivered into the burner. Detailed fluid flow investigations have suggested that approximately 30 to 50% of burned gas is recirculated to the combustion chamber in the TF configuration [180]. Again, a favorite case is considered when the closure of the gas inlet port is timed with the arrival of the reflected shock wave. At this moment, an expansion fan originates from the upper corner of the inlet port and propagates toward the other end of the channel which eventually brings the channel flow to rest. When the expansion fan reaches the end of the channel, the outlet port closes and the flow in the rotor channels stops. At this point, the flow with zero velocity is at nearly

the peak pressure and temperature of the cycle. It is now ready to be discharged into the turbine during the low-pressure process.

3.4 Gasdynamic Equations

To find flow properties inside wave rotor channels, it is required to predict the gasdynamic processes occurring inside the channels using boundary conditions provided by a thermodynamic cycle analysis. Proper design of a wave rotor requires a reasonable solution for the internal flow field.

To derive necessary equations for a gasdynamic analysis, several assumptions are made throughout this work. The aspect ratio of the wave rotor channels is assumed to be large enough, so the flow can be treated as one-dimensional. The flow within the rotor is considered frictionless and adiabatic. However, the wave rotor efficiency is used to account for dissipation losses inside the channels. The gases are treated as ideal gases.

3.4.1 Moving Normal Shock Wave Relations

Consider a moving normal shock wave which propagates with an absolute velocity w_S from right to left into a channel which contains a flow moving with velocity u_1 from left to right, as shown in the top part of Figure 36. The flow velocity decreases from u_1 to u_2 due to the mass motion induced by the shock. The term unsteady reference frame is attributed to this case. To find the flow properties in region 2 (compressed flow after the shock), the governing normal shock equations which are only valid for a stationary frame of reference can be used.

In a reference frame moving with the shock wave, the shock appears stationary and the downstream and upstream flow velocities are $u_1 + w_S$ and $u_2 + w_S$, respectively as shown in the bottom part of Figure 36.

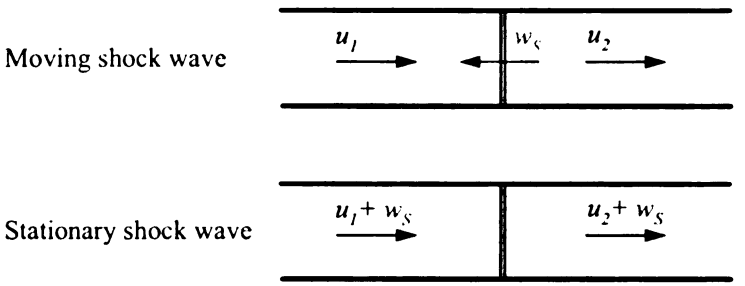

Figure 36: Transformation from a moving shock wave to a stationary shock wave

Applied to a control volume considered around the stationary shock wave, continuity, momentum, and energy equations become:

$$\rho_1 (w_S + u_1) = \rho_2 (w_S + u_2) \tag{2}$$

$$p_1 + \rho_1 (w_S + u_1)^2 = p_2 + \rho_2 (w_S + u_2)^2 \tag{3}$$

$$h_1 + \frac{(w_S + u_1)^2}{2} = h_2 + \frac{(w_S + u_2)^2}{2} \tag{4}$$

Assuming a calorically perfect fluid, solving the above equations leads to the relations given below, which give the local temperature ratio (T_2/T_1) and local density ratio (ρ_2/ρ_1) across the shock wave as a function of the local pressure ratio $\Pi_S = p_2/p_1$:

$$\frac{T_2}{T_1} = \Pi_S \left(\frac{\frac{\gamma+1}{\gamma-1} + \Pi_S}{1 + \frac{\gamma+1}{\gamma-1}\Pi_S} \right) \tag{5}$$

$$\frac{\rho_2}{\rho_1} = \frac{1 + \frac{\gamma+1}{\gamma-1}(\Pi_S)}{\frac{\gamma+1}{\gamma-1} + \Pi_S} \tag{6}$$

As seen, local thermodynamic properties across a moving normal shock are physically independent of the flow field velocities. Furthermore, the induced velocity can be expressed as:

$$u_{induce-shock} = \frac{a_1}{\gamma}(\Pi_S - 1)\sqrt{\frac{\frac{2\gamma}{\gamma+1}}{\Pi_S + \frac{\gamma-1}{\gamma+1}}} \tag{7}$$

where a_1 represent the speed of sound in the undisturbed region 1. Therefore, the flow velocity after the moving shock in region 2 becomes:

$$u_2 = u_1 - u_{induce-shock} \tag{8}$$

The moving shock velocity can be obtained as [216]:

$$w_S = a_1\sqrt{\frac{\gamma+1}{2\gamma}(\Pi_S - 1) + 1} \tag{9}$$

However, the velocity of the shock relative to the gas in the region 1 becomes w_S - u_1 or:

$$w_S = a_1\sqrt{\frac{\gamma+1}{2\gamma}(\Pi_S - 1) + 1} - u_1 \tag{10}$$

Furthermore, the shock Mach number is introduced as:

$$M_S = \frac{w_S + u_1}{a_1} = \sqrt{\frac{\gamma+1}{2\gamma}(\Pi_S - 1) + 1} \tag{11}$$

Finally, the entropy change across the shock is obtained by:

$$\Delta s = C_P ln\frac{T_2}{T_1} - C_P ln\frac{p_2}{P_1} \tag{12}$$

It is worthwhile to note that the total pressure increases across a moving shock while it decreases across a stationary shock wave. Also, the total enthalpy is not constant across

a moving shock wave. It increases for a moving shock wave, but it remains unchanged for a stationary shock wave.

3.4.2 Expansion Wave Relations

Due to the isentropic nature of expansion waves, the method of characteristics can be used to find the flow properties across an expansion wave. This method is a very general and powerful technique for analyzing compressible flow. For the specific problem considered in this study, only one-dimensional version of this method is used. Because the method of characteristics is a well-know theory, only the application of this method is used here and details of this theory can be found in the literature [216].

Consider any given point (x_1 , t_1) in the *x-t* plane as shown in Figure 37. It is possible to find a specific path through point (x_1 , t_1) along which the following equation holds:

$$u + \frac{2a}{\gamma - 1} = constant = J_+ \tag{13}$$

where u is the flow velocity and a is the sound speed. Such a path is called a C_+ characteristic line (right-running wave) in the *x-t* plane. This specific path is chosen so that its slope becomes $dt/dx = 1/(u + a)$.

In addition, a C_- characteristic line can be found through the point (x_1 , t_1) in Figure 37, where the slope of the C_- characteristic (left-running wave) is $dt/dx = 1/(u - a)$ and along which the following equation obtains:

$$u - \frac{2a}{\gamma - 1} = constant = J_- \tag{14}$$

The constant values of J_+ and J_- are known as the Riemann invariants.

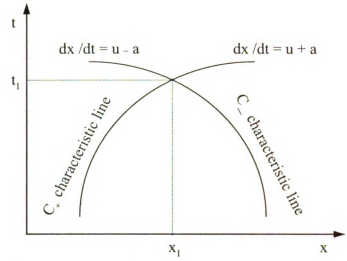

Figure 37: Illustration of the characteristic lines in the *x-t* plane

With the above results, it is possible to solve for the flow field in a one-dimensional expansion wave. As an example, consider again the generation of an expansion wave by suddenly closing a tube, as previously described in Figure 30. This figure is modified in Figure 38 to include a C_- characteristic line as well. Note that here the C_+ characteristic lines are physically the paths of the expansion waves in the *x-t* plane.

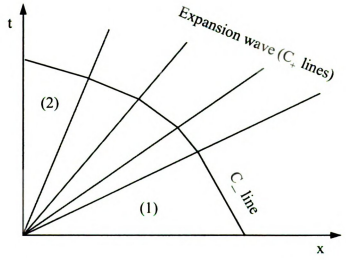

Figure 38: Left end closing to generate an expansion wave

Knowing the flow properties in front of the head of the expansion wave (region 1), solution for the flow behind the tail of the expansion wave (region 2) can be obtained as now described.

Because J_- is constant through the C_- characteristic line, Eq. (14) applied to both regions 1 and 2 gives:

$$u_1 - \frac{2a_1}{\gamma - 1} = u_2 - \frac{2a_2}{\gamma - 1} = J_- \tag{15}$$

However, the wall condition on the left side implies that $u_2=0$. Therefore, the sound speed ratio between region 1 and 2 can be written as:

$$\frac{a_2}{a_1} = 1 - \frac{\gamma - 1}{2}\frac{u_1}{a_1} \tag{16}$$

or,

$$\frac{T_2}{T_1} = \left[1 - \frac{\gamma - 1}{2}\frac{u_1}{a_1}\right]^2 \tag{17}$$

Because the expansion flow is isentropic, therefore:

$$\frac{p_2}{p_1} = \left(\frac{T_2}{T_1}\right)^{\frac{\gamma}{\gamma-1}} = \left[1 - \frac{\gamma - 1}{2}\frac{u_1}{a_1}\right]^{\frac{2\gamma}{\gamma-1}} \tag{18}$$

and,

$$\frac{\rho_2}{\rho_1} = \left(\frac{T_2}{T_1}\right)^{\frac{1}{\gamma-1}} = \left[1 - \frac{\gamma - 1}{2}\frac{u_1}{a_1}\right]^{\frac{2}{\gamma-1}} \tag{19}$$

The expansion wave induces a mass motion in the direction opposite to its propagation, but equal in value to the flow in region 1. Therefore, it is also possible to find a relation

for the induced velocity based on the pressure ratio across the expansion wave. This can be easily found by using Eq. (18) as:

$$u_{induce-expansion} = \frac{2a_1}{\gamma - 1}\left[1 - \left(\frac{p_2}{p_1}\right)^{\frac{\gamma-1}{2\gamma}}\right] \tag{20}$$

It can be shown that this relation obtained for the induced velocity is independent of flow velocities of the medium in which the expansion wave moves. Here, the velocity of the flow in region 2 was zero, however, Eq. (20) always calculates the change of flow velocity due to the wave expansion. This conclusion is also valid for the induced velocity generated by a moving shock wave described before, as shown in Eq. (7). Both induced velocities are only functions of the pressure ratio across the waves, the speed of sound, and the γ value of the downstream flow.

Finally, it is important to mention that the head of the expansion wave moves with the velocity $u_1 + a_1$ to the right because it is a C_+ characteristic line. The same reasoning shows that the tail of the expansion wave moves at the slower velocity $0 + a_2$ in the same direction. Hence, the expansion wave spreads out as it propagates down the tube.

CHAPTER 4: THERMODYNAMIC ANALYSIS

4.1 Microturbines

A growing market for distributed power generation and propulsion of small vehicles has motivated a strong interest in design of small gas turbine systems in the range of 30-300 kW. Known as microturbines, they are now widely used in the US for distributed power generation, shaving peak loads, and providing backup power for critical needs. They propel small commercial aircraft, unmanned air vehicles (UAV), and terrestrial vehicles. Microturbines are often the preferred alternative to IC engines, due to their higher power density and robustness. They present several advantageous features such as compact size, simple operability, ease of installation, low maintenance, fuel flexibility, and low NO_X emissions. Furthermore, due to the recent electric-power crises and environmental concerns, a strong interest in the research, development, and application of microturbines has been stimulated

Despite their attractive features, compared with larger gas turbines, microturbines suffer from lower thermal efficiency and their relative output power, due to their limited cycle pressure ratio and peak cycle temperature. For many applications improvement of their performance is desirable to enhance advantages over competing technologies.

To achieve such improvements, current efforts are mainly focused on utilizing heat recovery devices and developing new high-strength high-temperature materials for turbine blades [217]. Geometries of microturbines make blade cooling very difficult. Hence, their lifetimes using typical materials used for larger gas turbines are shorter [218]. Therefore, there is significant research toward developing advanced metallic alloys and ceramics for high-thermal-resistance turbine wheels used in microturbines[219, 220].

Currently, recuperators play a key role in performance enhancement of microturbines. For example, experimental and theoretical research has shown that microturbines with pressure ratios of 3 to 5 without recuperation systems achieve only about 15 to 20% efficiency [221, 222]. Utilizing conventional recuperators based on the use of existing materials can improve the thermal efficiency of microturbines up to 30% [222-225]. An excellent example of a commercial microturbine with a recuperator is the Capstone 30 kW unit, with an efficiency of 26% using natural gas fuel [226].

Despite the attractive feature of the recuperator concept, a recuperator introduces pressure losses reducing the output power and it adds about 25 to 30% to the overall engine manufacturing cost, which is a challenge for commercialization of microturbines [227-229]. The current trend of the microturbine market is to reduce the investment cost per kW. Therefore, alternative devices need to be considered to achieve higher performance at lower component costs. Topping a microturbine with a wave rotor device is an appropriate solution. Wave rotor investigations [154, 164, 198-200] have shown a significant potential for performance gain in smaller gas turbines, where the compressor pressure ratios are typically lower than those of larger machines.

The objective of the present chapter is a comprehensive and systematic performance analysis of two actual microturbines known as the C-30 and C-60 engines made by Capstone Turbine Corporation which are topped with a four-port wave rotor in various wave-rotor-topping cycles. The challenges and advantages associated with the different implementation cases are discussed. While the performance evaluation of several gas turbine engines has been studied extensively [154, 198-, 200], to the knowledge of the author, there exits no comprehensive work investigating the potential benefits of various

implementation cases of wave rotor topping cycles for small gas turbines. The presented results have been obtained using basic thermodynamic equations along with the wave-rotor characteristic equation previously validated using computational tools [154]. The model can be employed to predict the performance improvement of various wave-rotor-topping cycles without the need for knowing the details of the complex fluid mechanics within the wave rotor. [2]

4.2 Gas Turbine without Recuperation

4.2.1 Implementation Cases

There are several possibilities to top a gas turbine with a wave rotor. Considering possible design restrictions and preferences, five different advantageous implementation cases for a wave rotor into a given baseline engine can be introduced as follows:

Case A: same compressor, same turbine inlet temperature

Case B: same overall pressure ratio, same turbine inlet temperature

Case C: same combustor

Case D: same turbine

Case E: same compressor, same combustion end temperature

These five cases have been described in detail in the following. According to the state numbering introduced in Figure 4 (or Figure 34), Figure 39 visualizes all five cases in schematic T-s diagrams. Path $0\text{-}1_b\text{-}4_b\text{-}5_b$ represents the baseline cycle and $0\text{-}1_i\text{-}2_i\text{-}3_i\text{-}4_i\text{-}5_i$ (i=A, B, C, D, E) indicates the wave-rotor-topped cycles, where the subscripts indicate the case. One of the five cases might be preferable for a practical design. However intermediate design cases are possible.

---

[2] Parts of materials presented in this chapter have been accepted for publication in *2005 ASME Journal of Engineering for Gas Turbines and Power.*

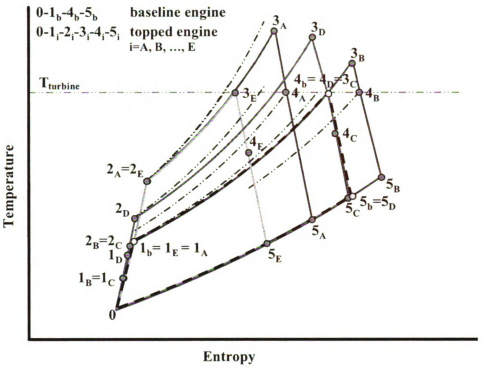

Figure 39 : Schematic T-s diagrams for a baseline cycle and five wave-rotor-topped cycles

Case A: In Case A the pressure ratio of the compressor is kept unchanged, so the physical compressor of the baseline engine can also be used for the wave-rotor-enhanced engine provided the mass flow is kept approximately the same. The pressure in the combustion chamber of the enhanced engine is increased by the compression ratio of the wave rotor. This may require modifications to the structure of the combustion chamber and to the fuel injection system. The heat addition in the combustor is the same as for the baseline engine, but it takes place after the energy exchange in the wave rotor, hence the heat addition starts at a higher temperature. Thus, the combustion end temperature is even higher than that of the baseline engine, possibly requiring additionally a thermal enhancement of the combustor structure. The turbine of the topped engine might need to be adapted to efficiently utilize the higher pressure ratio. The turbine inlet temperature,

however, is the same as that of the baseline engine. As will be shown later, this implementation case provides the highest thermal efficiency and specific work and the lowest value of *SFC*.

Case B: In Case B the overall pressure ratio for the wave-rotor-enhanced engine is kept equal to that of the baseline engine, so that the combustor works under the same pressure. However, for the wave-rotor-topped engine, the heat addition in the combustor and the combustion end temperature are greater than those of the baseline engine. This may require some adaptation of the combustor, especially in the outlet region. The turbine and compressor work with lower pressure ratios, reducing the design challenges. Thus, both may be adapted advantageously. This might reduce the cost of the compressor and turbine due to reduction of stages in multi-stage types (mostly axial), or due to reduction of the tip diameter in radial types (mostly single-stage). With a smaller tip diameter the wheels can be manufactured more economically over a shorter time from cheaper materials with less strength and on smaller machines. Besides an attractive performance enhancement, this case additionally provides the highest turbine outlet temperature of all five cases investigated. The temperature of the leaving exhaust gas is much higher than that of the baseline engine. Therefore, this case is attractive for an external heat recovery application or for internal recuperation that can enhance the performance further.

Case C: Case C assumes that it is desirable for the wave-rotor-enhanced engine to use the unmodified combustor of the baseline engine. So the overall pressure ratio and combustor inlet and outlet temperatures for the wave-rotor-enhanced engine are kept equal to those of the baseline engine. The heat addition in the combustor is consequently

the same.[3] The implementation of the wave rotor considerably reduces the pressure ratio of the turbine and compressor. The compressor pressure ratio is as low as in Case B, and the turbine pressure ratio and turbine inlet temperature are even lower than those in Case B. Thus, the turbine and compressor could be made from less thermally resistant material. Compared to the baseline engine, they also could be smaller and hence less expensive, as discussed in Case B. This might be the main implementation reason because unfortunately, but not surprisingly, the unambitious combustor constrains the performance enhancement. It is nearly negligible for the smaller C-30 engine and even negative for the C-60 engine.

Case D: Case D employs the same physical turbine as the baseline engine. Due to the wave-rotor-topping, the compressor needs to produce a lower pressure ratio than that of the baseline engine. This allows for a smaller and less expensive compressor as discussed for Cases B and C. The pressure in the combustion chamber and the combustion end temperature are higher than those of the baseline engine, but lower than those of Case A. Hence, less effort might be required to adapt the structure and fuel injection of the combustion chamber. As a result of the lower pressure ratio in the compressor, hence lower compressor discharge temperature, the heat addition in the combustor has to be more than that for the baseline engine to utilize the same allowed turbine inlet temperature. This case gives the second highest performance increase for both baseline engines.

Case E: Case E is similar to Case A but the combustion end temperature (the cycle peak temperature) is restricted to the turbine inlet temperature of the baseline engine in

[3] The wave rotor compression efficiency is greater than the compressor efficiency. Therefore, the combustor inlet temperature is in fact negligibly smaller and hence the heat addition is negligibly greater than that in the baseline engine.

order to avoid additional thermal requirements on the combustor design. The overall pressure ratio is the same as in Case A because this case employs the same physical compressor as for the baseline engine. Thus, the overall pressure ratio is greater than that of the baseline engine, by the wave rotor pressure ratio. The heat addition in the combustor is less than that for the baseline engine because to the wave rotor compression work is added to the fluid before combustion. The turbine in the topped cycle works with a slightly greater pressure ratio than the turbine of the baseline engine, but the turbine inlet temperature is less than that for the baseline engine. In fact, it is the lowest of all cases investigated. This may give the option to produce the turbine wheel at a lower cost out of less thermally resistant material.

4.2.2 Thermodynamic Calculations

To evaluate the performance enhancement of topping gas turbines with wave rotors, a computer program based on a thermodynamic model has been developed to determine the thermodynamic properties of the gases in different states of the cycles. The results are used to calculate the theoretical performance (expressed by thermal efficiency η , net specific work w, and specific fuel consumption *SFC*) and the actual T-s diagrams of both wave-rotor-topped and baseline engines. The methodology is similar to that introduced by Wilson and Paxson [154] with some modifications. The component performance parameters for the baseline engines are based on information provided by the manufacturer and are listed in Table 1.

Table 1: Baseline engine data, assuming T_0=300 K, Cp_{air}=1.005 kJ/kgK, Cp_{gas}=1.148 kJ/kgK, γ_{air}=1.4 , γ_{gas}=1.33

Baseline engine		C-30	C-60
turbine inlet temperature	T_{t4b}	1116.5 K (1550° F)	1227.6 K (1750° F)
compressor outlet temperature	T_{t1b}	466.5 K (380° F)	505.4 K (450° F)
compressor pressure ratio	p_{t1b}/p_0	3.6	4.8
compressor isentropic efficiency	η_C	79.6%	82.6%
turbine isentropic efficiency	η_T	84%	85%
compressor polytropic efficiency	η_{PC}	82.9%	85.9%
turbine polytropic efficiency	η_{PT}	81.7%	82.3%
combustor pressure ratio	Π_{comb}	0.98	0.98

For each engine it is assumed that the compressor inlet condition is known and is the same for both baseline and wave-rotor-enhanced engines. Considering the same "aerodynamic quality" of the wheels, the polytropic efficiencies are kept the same for the enhanced and baseline engine, for the compressor and turbine respectively. Incomplete combustion of the fuel is reflected by a combustor efficiency of 98% (η_Q = 0.98). No pressure losses in the intake air filter, exhaust silencer and additional piping, or heat losses or mechanical losses are taken into account. Such losses reduce the predicted performance. The gases are treated as ideal gases. For both air and burned gas constant values of specific heat coefficients (Cp_{air} = 1.005 kJ/kgK, Cp_{gas} = 1.148 kJ/kgK) and specific heat ratios (γ_{air}= 1.4 , γ_{gas}= 1.33) are considered. This assumption simplifies the performance calculations significantly without affecting the qualitative nature of the results. Air enters the compressor at 300 K.

In the following it is assessed how the wave-rotor-topping enhances the performance of C-30 and C-60 baseline gas turbine engines.

- **Path 0-1: Compressor**

With the given compressor inlet temperature ($T_0=T_{t0}$), the compressor outlet total temperature and pressure are calculated from the adiabatic relations:

$$T_{t1} = T_{t0} + \frac{T_{t0}}{\eta_C}\left(\Pi_C^{\frac{\gamma_{air}-1}{\gamma_{air}}} - 1\right) \tag{21}$$

$$\frac{p_{t1}}{p_{t0}} = \frac{p_{t1}}{p_0} = \Pi_C \tag{22}$$

where the compressor isentropic efficiency (η_C) relates the compressor pressure ratio (Π_C) to the compressor polytropic efficiency (η_{PC}) through:

$$\eta_C = \frac{\Pi_C^{\frac{\gamma_{air}-1}{\gamma_{air}}} - 1}{\Pi_C^{\frac{\gamma_{air}-1}{\gamma_{air}\eta_{PC}}} - 1} \tag{23}$$

For Cases A and E, the compressor pressure ratio is equal to that of the baseline engine (e.g. for the C-30 engine Π_C = 3.6 and for the C-60 engine Π_C = 4.8). However, for Cases B and C its value is calculated by dividing the baseline compressor pressure ratio with the wave rotor compression ratio ($PR_W = p_{t2}/p_{t1}$). The wave rotor compression ratio plays an important role in the performance analysis of wave-rotor-tapping engines by significantly altering the engine performance. A higher value of a PR_W leads to a higher engine performance. Fatsis and Ribaud have varied PR_W from 1.4 to 3 in their calculations [198, 199]. PR_W values lower than 1.8 have considered unacceptable due to the poor compression processes inside the rotor. The authors believe that a PR_W value higher than 3 is unrealistic. This is confirmed by detailed calculations in a four-port wave rotor by Welch [164]. Wilson and Paxson have used PR_W = 1.8 from GE data [154]. They have used the term "advanced" for their wave rotor working with PR_W = 3.6. Therefore, a

wave rotor compression ratio of 1.8 appears to be conceivable for the envisioned application and is chosen for the following discussion. In this work all performance plots are shown for various wave rotor pressure ratios, indicating its effect on cycle performance enhancement. For Case E, the value of Π_C is calculated in a way that keeps the pressure at the turbine inlet equal for both baseline and topped engines. This calculation can be performed by inreversly solving of Eq. (21) through (41). Finally, the compressor specific work is obtained as:

$$w_C = Cp_{air}(T_{t1} - T_{t0}) = \frac{Cp_{air} T_{t0}}{\eta_C}(\Pi_C^{\frac{\gamma_{air}-1}{\gamma_{air}}} - 1) \tag{24}$$

- **Path 1-2: Compression in the Wave Rotor**

The flow properties after the wave rotor compression process are obtained from the adiabatic relations similarly to those of the compressor:

$$T_{t2} = T_{t1} + \frac{T_{t1}}{\eta_{WC}}\left(PR_W^{\frac{\gamma_{air}-1}{\gamma_{air}}} - 1\right) \tag{25}$$

$$\frac{p_{t2}}{p_{t0}} = \frac{p_{t2}}{p_{t1}}\frac{p_{t1}}{p_{t0}} = PR_W \cdot \Pi_C \tag{26}$$

where η_{WC} is the wave rotor compression efficiency. Later η_{WE}, which is defined as the wave rotor expansion efficiency, will be used. Consistently with previous wave rotor investigations [154, 164, 198, 199], the wave rotor compression and expansion efficiencies are assumed as $\eta_{WC} = \eta_{WE} = 0.83$ in this study. In fact, the efficiencies are not constant values. However, the range of variations have been almost determined. In previous wave rotor studies it was not possible to evaluate η_{WC} and η_{WE} separately. Instead, their product was determined. Moritz found $\eta_{WC} \cdot \eta_{WE} = 0.6$ in experiments at Rolls-Royce [130]. Reference [153] has reported a range of $0.77 < \eta_{WC} = \eta_{WE} < 0.86$.

Wilson and Paxson assumed $\eta_{WC} = \eta_{WE} = 0.83$ based on previous work on wave rotors [154]. Recently, Fatsis and Ribaud have taken into account the effect of wave rotor efficiencies on the performance of several different types of gas turbine engines topped by a wave rotor [198, 199]. They have carried out their calculations with efficiencies in a range between $0.8 < \eta_{WC} = \eta_{WE} < 0.86$. For a small size turbojet engine considered in their study, they have shown that the gains of specific power and specific fuel consumption are sensitive to the values of wave rotor efficiencies. These authors have emphasized that it is important to optimize efficiencies for the compression and expansion processes.

- **Path 2-3: Combustion Chamber**

The value of fuel/air ratio ($f=m_f/m_{air}$) can be obtained by applying the energy (first law) equation to the combustion chamber:

$$\eta_Q \, f \, h_{PR} = (1+f) Cp_{gas} T_{t3} - Cp_{air} T_{t2} \tag{27}$$

where $h_{PR} = 43000$ kJ/kg is the heating value used for all calculations here. This equation gives:

$$f = \frac{Cp_{gas} T_{t3} - Cp_{air} T_{t2}}{\eta_Q \, h_{PR} - Cp_{gas} T_{t3}} \tag{28}$$

Alternatively, f can be expressed based on the turbine total inlet temperature (T_{t4}) and the compressor total exit temperature (T_{t1}). For this purpose, the wave rotor compression and expansion specific work (per unit mass of air flow) are defined respectively as follows:

$$w_{WC} = Cp_{air} (T_{t2} - T_{t1}) \tag{29}$$

$$w_{WE} = (1+f) Cp_{gas} (T_{t3} - T_{t4}) \tag{30}$$

Here, it is considered that $\dot{m}_1 = \dot{m}_2 = \dot{m}_{air}$ and $\dot{m}_3 = \dot{m}_4 = \dot{m}_{air} + \dot{m}_f$. Other cycles exist in which the mass flow rates $\dot{m}_1$ and $\dot{m}_2$ are not the same, and, correspondingly the mass flow rates $\dot{m}_3$ and $\dot{m}_4$ may not be equal either. These cycles are not considered here. Using Eqs. (29) and (30) , Eq. (27) can be expressed as:

$$\eta_Q \, f \, h_{PR} = (1+f) Cp_{gas} T_{t4} + w_{WE} - w_{WC} - Cp_{air} T_{t1} \tag{31}$$

Because the net output work of the wave rotor is zero ($w_{WC} = w_{WE}$), solving for f leads to:

$$f = \frac{Cp_{gas} T_{t4} - Cp_{air} T_{t1}}{\eta_Q \, h_{PR} - Cp_{gas} T_{t4}} \tag{32}$$

For Cases C and E, T_{t3} is equal to the baseline inlet turbine temperature, therefore Eq. (28) is used to calculate f. For Cases A, B, and D, where T_{t4} is a known value and is equal to the baseline inlet turbine temperature, f can be obtained from Eq. (32). The relation between T_{t3} and T_{t4} can be found by equating Eqs. (29) and (30):

$$T_{t3} = T_{t4} + \left[\frac{T_{t1}}{\eta_{WC}} \left(PR_W^{\frac{\gamma_{air}-1}{\gamma_{air}}} - 1 \right) \right] \frac{Cp_{air}}{(1+f) Cp_{gas}} \tag{33}$$

Finally, the total pressure after the combustion chamber is obtained:

$$\frac{p_{t3}}{p_{t0}} = \frac{p_{t3}}{p_{t2}} \frac{p_{t2}}{p_{t0}} = \Pi_{comb} \cdot PR_W \cdot \Pi_C \tag{34}$$

- **Path 3-4: Expansion in the Wave Rotor**

To obtain the turbine inlet total pressure (p_{t4}), it is convenient to express the wave rotor compression work and the expansion work in terms of pressure ratios:

$$\dot{W}_{WC} = \dot{m}_{air} Cp_{air} (T_{t2} - T_{t1}) = \frac{\dot{m}_{air} Cp_{air} T_{t1}}{\eta_{WC}} \left(PR_W^{\frac{\gamma_{air}-1}{\gamma_{air}}} - 1 \right) \tag{35}$$

$$\dot{W}_{WE} = (\dot{m}_{air} + \dot{m}_f) Cp_{gas} (T_{t3} - T_{t4}) = (\dot{m}_{air} + \dot{m}_f) Cp_{gas}\ \eta_{WE}\ T_{t3} \left[1 - \left(\frac{PO}{\Pi_{comb} PR_W} \right)^{\gamma_{gas}-1/\gamma_{gas}} \right] \quad (36)$$

Where $PO = p_{t4} / p_{t1}$ is the pressure gain ratio across the wave rotor. Equating the compression work to the expansion work leads to:

$$\frac{Cp_{air}\ T_{t1}}{\eta_{WC}} \left(PR_W^{\frac{\gamma_{air}-1}{\gamma_{air}}} - 1 \right) = (1+f) Cp_{gas}\ \eta_{WE}\ T_{t3} \left[1 - \left(\frac{PO}{\Pi_{comb} PR_W} \right)^{\gamma_{gas}-1/\gamma_{gas}} \right] \quad (37)$$

Substituting T_{t3} from Eq. (33) into Eq. (37) and some algebra gives:

$$PO = \Pi_{comb} PR_W \left\{ 1 - \frac{A\dfrac{1}{\eta_{WE}\ \eta_{WC}} B}{1 + A\dfrac{1}{\eta_{WC}} B} \right\}^{\gamma_{gas}/\gamma_{gas}-1} \quad (38)$$

where

$$A = \frac{Cp_{air}}{(1+f) Cp_{gas}} \quad (39)$$

$$B = \frac{T_{t1}}{T_{t4}} \left[PR_W^{(\gamma_{air}-1)/\gamma_{air}} - 1 \right] \quad (40)$$

Equation (38) is a modified version of the "wave-rotor characteristic" equation introduced in the literature [154]. This equation represents the performance of the wave rotor. It predicts the pressure gain ratio across the wave rotor as a function of the temperature ratio across it (T_{t4} / T_{t1}). For $\eta_{WC} = \eta_{WE} = 0.83$, $f = 0$, $\Pi_{comb} = 100\%$, and $PR_W = 1.8$, Figure 40 clearly indicates monotonically increasing of the pressure gain as a function of the temperature ratio across the wave rotor. For a fixed turbine inlet temperature (e.g., T_{t4} = constant), using a smaller compressor with a low pressure ratio leads to a higher pressure gain across the wave rotor. Similarly, for a fixed compressor

pressure ratio, increasing the turbine inlet temperature results in a greater pressure gain across the wave rotor. The most significant performance gain has been found for engines with low compressor pressure ratios and high turbine inlet temperatures [154, 164, 198, 199].

Equation (38) can be also used again to investigate the influence of the wave rotor compression ratio on the pressure gain ratio across the wave rotor. This is shown in Figure 41 for $\eta_{WC} = \eta_{WE} = 0.83$, $f = 0$, $\Pi_{comb} = 100\%$, and $T_{t4}/T_{t1} = 2.2$. The plot clearly indicates that the pressure gain ratio across the wave rotor is an increasing function of the wave rotor compression ratio, while the highest relative gains are obtained at low compressor ratios. Therefore, higher values for PR_W results in a higher net absolute performance gain.

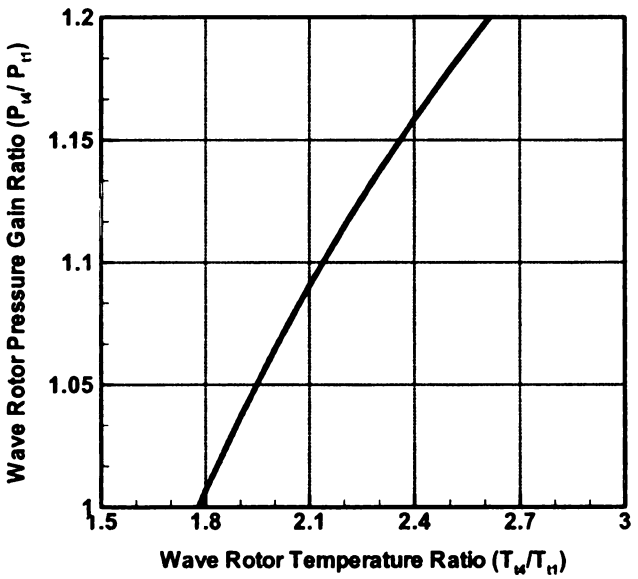

Figure 40: Pressure gain ratio across the wave rotor versus temperature ratio across it

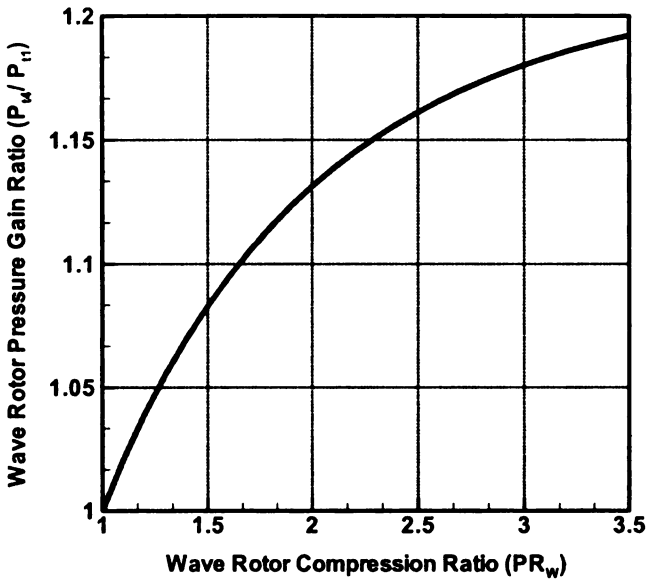

Figure 41: Pressure gain ratio across the wave rotor versus wave rotor compression ratio

By using Eq. (38), the turbine inlet total pressure is obtained as:

$$\frac{p_{t4}}{p_{t0}} = \frac{p_{t4}}{p_{t1}}\frac{p_{t1}}{p_{to}} = PO \cdot \Pi_C \tag{41}$$

For Cases C and E, where T_{t4} is an unknown value, the turbine inlet temperature is obtained by using Eq. (33), and T_{t3} is equal to the baseline inlet turbine temperature.

- **Path 4-5: Turbine**

The turbine specific work (per unit mass of air flow) can be calculated knowing the pressure ratio across the turbine:

$$w_T = (1+f)Cp_{gas}(T_{t4} - T_{t5}) = (1+f)\eta_T Cp_{gas} T_{t4}\left[1 - (\frac{p_0}{p_{t4}})^{\frac{\gamma_{gas}-1}{\gamma_{gas}}}\right] \tag{42}$$

assuming the turbine expands the hot gas leaving the wave rotor to atmospheric pressure ($p_{t5}=p_0$). The isentropic turbine efficiency (η_T) can be obtained from the polytropic turbine efficiency η_{PT}:

$$\eta_T = \frac{\left(\frac{p_0}{p_{t4}}\right)^{(\gamma_{gas}-1)\eta_T/\gamma_{gas}} - 1}{\left(\frac{p_0}{p_{t4}}\right)^{(\gamma_{gas}-1)/\gamma_{gas}} - 1} \tag{43}$$

Therefore, the total temperature of the gas leaving the turbine can be calculated as:

$$T_{t5} = T_{t4} - \frac{w_T}{(1+f)Cp_{gas}} \tag{44}$$

After calculating the thermodynamic properties of all states in the cycle, it is possible to calculate the engine performance parameters. The net specific output work produced by the engine can be calculated by subtracting the turbine specific work from the compressor work:

$$w = \eta_M w_T - w_C = \eta_M \eta_T Cp_{gas} T_{t4}\left[1-\left(\frac{p_{t0}}{p_{t4}}\right)^{\frac{\gamma_{gas}-1}{\gamma_{gas}}}\right] - \frac{Cp_{air} T_{t0}}{\eta_C}\left(\Pi_C^{\frac{\gamma_{air}-1}{\gamma_{air}}} - 1\right) \tag{45}$$

Where η_M is the turbine shaft mechanical efficiency. In this study an ideal transmission case (η_M =100%) is considered.

With the amount of specific heat addition through the combustion process being defined as $q=f.\ h_{PR}$, the thermal efficiency can be written as:

$$\eta = \frac{w}{q} = \frac{\eta_M \eta_T Cp_{gas} T_{t4}\left[1-\left(\frac{p_{t0}}{p_{t4}}\right)^{\frac{\gamma_{gas}-1}{\gamma_{gas}}}\right] - \frac{Cp_{air} T_{t0}}{\eta_C}\left(\Pi_C^{\frac{\gamma_{air}-1}{\gamma_{air}}} - 1\right)}{f\, h_{PR}} \tag{46}$$

Finally, the specific fuel consumption (*SFC*) is calculated from:

$$SFC = \frac{f}{w} \tag{47}$$

4.2.3 Predicted Performance Results

Cases A and B are the most common cases discussed in the literature, therefore, they have been discussed here in more detail.

Case A: Figure 42 shows the actual T-s diagrams for the baseline engines C-30 and C-60 as well as for the topped engines, simulated with a wave rotor pressure ratio of 1.8 (PR_W = 1.8). The overall pressure ratio of the enhanced engines is 1.8×3.6=6.48 and 1.8×4.8=8.64, respectively. The T-s diagrams qualitatively show that the topped engine has a higher thermal efficiency compared to the baseline engine. This is because the turbine has a higher specific work output, while the consumption of specific work by the compressor and specific heat addition to the cycle remain the same as for the baseline engine. Details of calculations for creating such plots are described step by step in Appendix B.

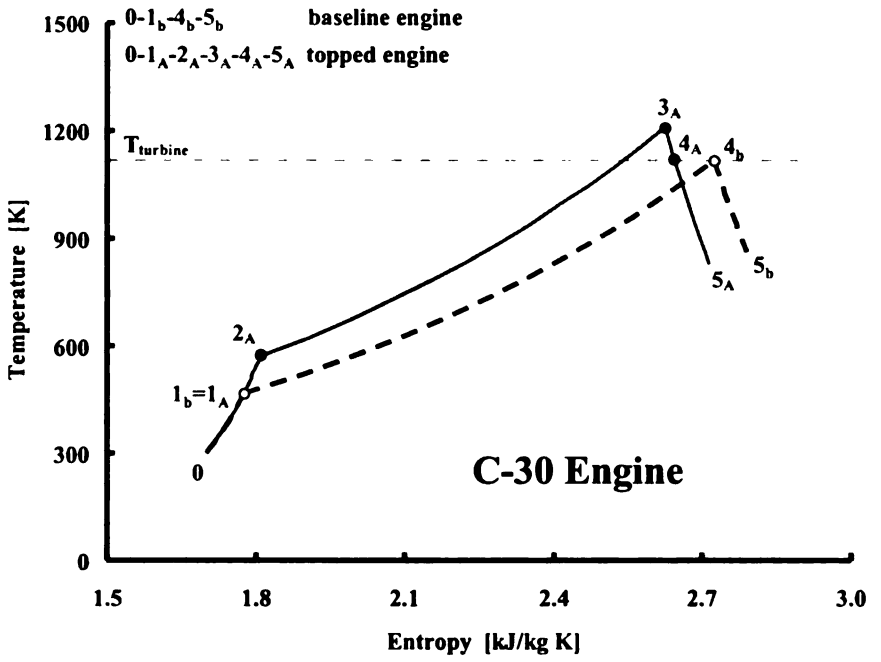

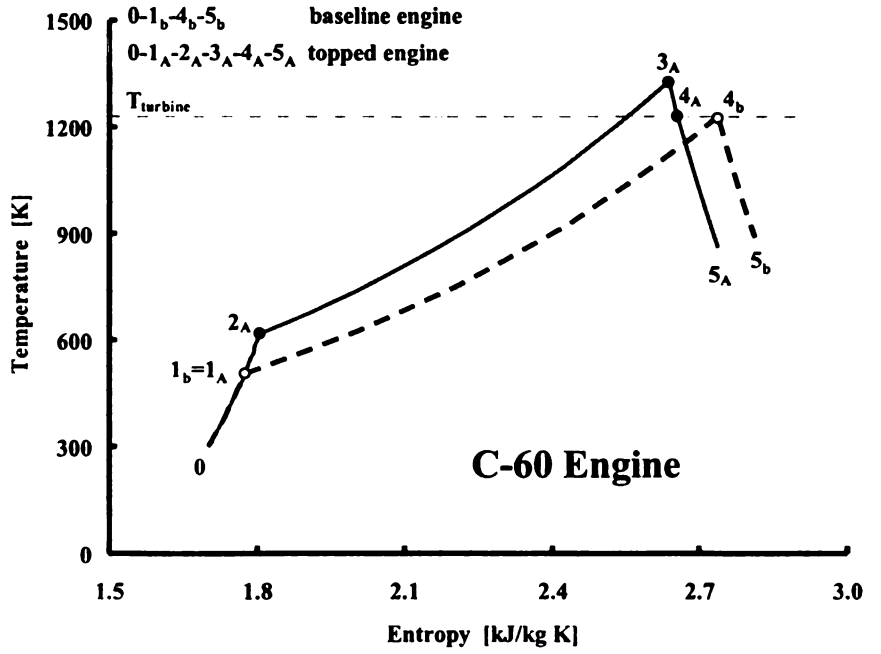

Figure 42: T-s diagrams for the C-30 and C-60 wave-rotor-topped engines for Case A implementation

Figure 43 illustrates the increase of cycle thermal efficiency (dash dot) and specific work (dashed), and the decrease of specific fuel consumption (solid) with increasing wave rotor pressure ratio PR_W for both the C-30 and C-60 topped engines. The plot visualizes how the effect develops from the baseline engine with PR_W =1 until PR_W =2 which might be a practical limit for the investigated application. However, if the wave rotor pressure ratio increases beyond this limit, the trend already shows that the rate of increase of the effect diminishes while technical problems may increase. With a conceivable wave rotor pressure ratio of 1.8, the thermal efficiency of the baseline cycle increases from 14.9% to 20.0% for the C-30 engine and from 19.4% to 24.2% for the C-60 engine. Simultaneously, the specific work increases from 128 kJ/kg to 171 kJ/kg for the C-30 engine and from 184 kJ/kg to 231 kJ/kg for the C-60 engine. The specific fuel consumption (*SFC*) of the C-30 engine decreases from 0.156 kg/kN.s to 0.116 kg/kN.s and it reduces from 0.120 kg/kN.s to 0.095 kg/kN.s for the C-60 engine.

A better picture of the performance improvement is obtained by calculating the relative increases of thermal efficiency, specific work, and the relative decrease of *SFC* as shown in Figure 44. For Case A, the relative increases of thermal efficiency and specific work (dash dot) are precisely the same as it is obvious from Eq. (46) where the heat addition $q=f.h_{PR}$ is the same for both topped and baseline engines. For a wave rotor pressure ratio of 1.8, Figure 44 indicates an attractive relative performance improvement in thermal efficiency and specific work of about 33.8% and a 25.2% reduction in *SFC* (solid) for the C-30 engine. The C-60 engine shows a 25.1% enhancement in thermal efficiency and specific work and a 20.1% reduction in *SFC*.

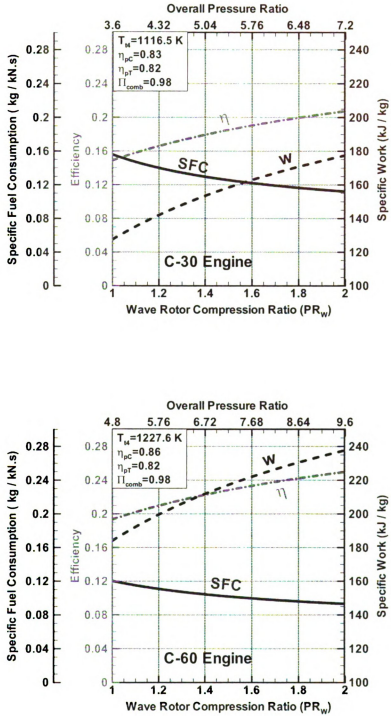

Figure 43: Thermal efficiency, specific work, and *SFC* for the wave-rotor-topped engines versus the wave rotor pressure ratio and overall pressure ratio, Case A consideration

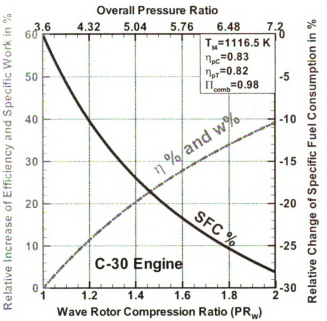

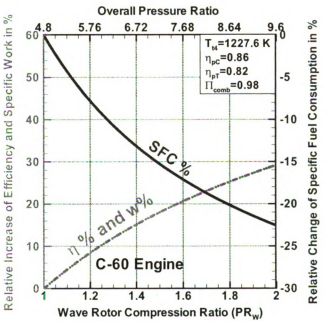

Figure 44: Relative values of thermal efficiency, specific work, and *SFC* for the wave-rotor-topped engines versus the wave rotor pressure ratio and overall pressure ratio, Case A consideration

Case B: As described before, Case B considers another way to implement a wave rotor beneficially. While keeping the overall pressure ratio of the topped engine equal to that of the baseline engine, the compressor pressure ratio is reduced in the wave-rotor-enhanced engine. Lowering the compressor pressure ratio usually leads to a higher isentropic compressor efficiency (for comparable aerodynamic impeller quality, here simulated by using the same polytropic compressor efficiency), less the mass of the compressor, and probably lower manufacturing costs.

Figure 45 depicts the actual T-s diagrams of the baseline engines and the wave-rotor-topped engines for Case B. Now, the overall pressure ratio is fixed at 3.6 and 4.8 for the C-30 and the C-60 engines, respectively. It is evident that the compressor work of the topped engine is less than that of the baseline engine. However, the turbine work is less too, but the heat addition for the topped engine is greater than that of the baseline engine. So, without calculating the thermal efficiency and specific work it is problematical to determine whether the topped engine has a higher performance than the baseline engine. Clearly shown in Figure 45 is that the turbine outlet temperature is considerably higher than that of the baseline engine ($T_{5B}>T_{5b}$), making this case attractive for heat recovery applications due to the available additional thermal energy from the exhaust gas.

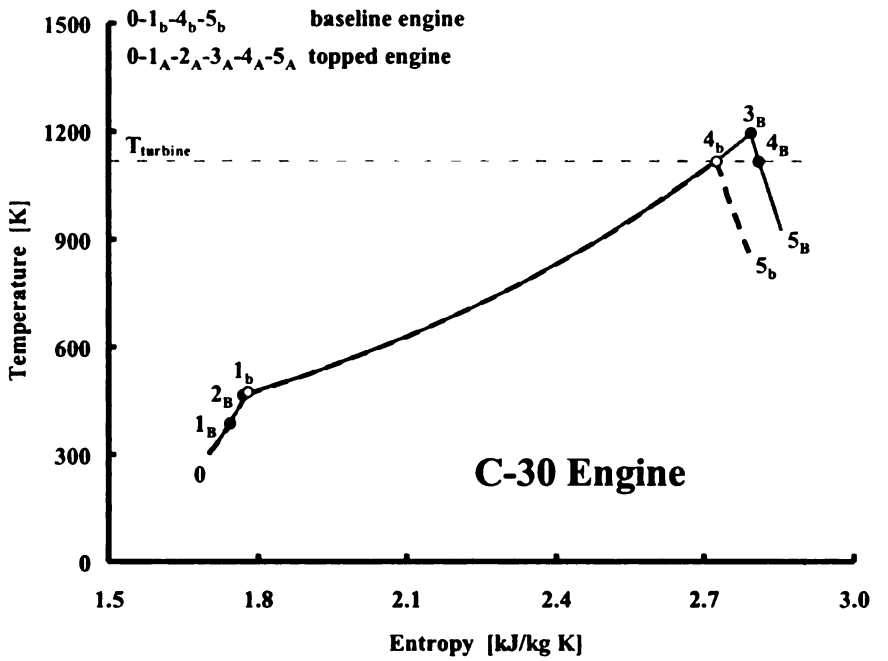

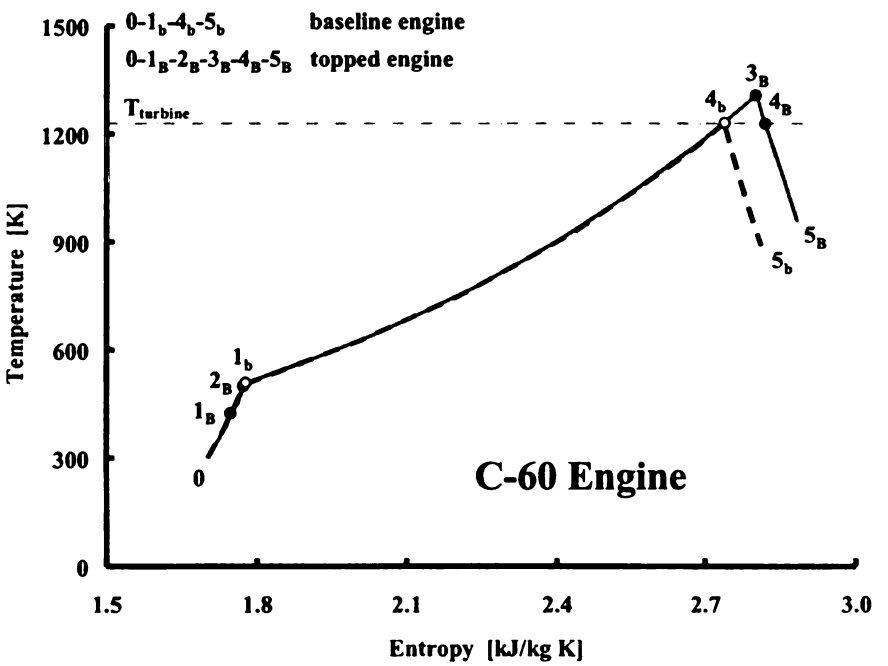

Figure 45: T-s diagrams for the C-30 and C-60 wave-rotor-topped engines for Case B implementation

Values of the thermal efficiency, specific work, *SFC* and as well as their relative increase of the wave-rotor-topped C-30 engine can be obtained from the plots in Figure 46 and Figure 47, respectively. Similar to Case A, both thermal efficiency and specific work are monotonically increasing functions of the wave rotor pressure ratio PR_W while *SFC* is decreased. Now, the relative increase of thermal efficiency (dash dot in Figure 47) is considerably less than the relative increase of the specific work (dashed), because the heat addition is greater in the wave-rotor-topped cycle. Similar results are obtained for the C-60 engine, not shown here.

For Case B, the results show that with a wave rotor pressure ratio of 1.8 the thermal efficiency of the C-30 engine increases from 14.9% to 15.8%, and from 24.8% to 27.3% for the C-60 engine. Similarly, the specific work increases from 128 kJ/kg to 150 kJ/kg for the C-30 engine, and from 116 kJ/kg to 137 kJ/kg for the C-60 engine. Finally, *SFC* of the C-30 engine decreases from 0.156 kg/kN.s to 0.147 kg/kN.s and from 0.094 kg/kN.s to 0.085 kg/kN.s for the C-60 engine.

For the same PR_W = 1.8, wave-rotor-topping of the C-30 engine gives a relative increase of 5.9% and 17.1% for the thermal efficiency and specific work, respectively, and 5.6% reduction in *SFC*. For the C-60 engine, the performance improvement is less with 9.7% and 18.0% increase of thermal efficiency and specific work, respectively, and 8.7% reduction in *SFC* .

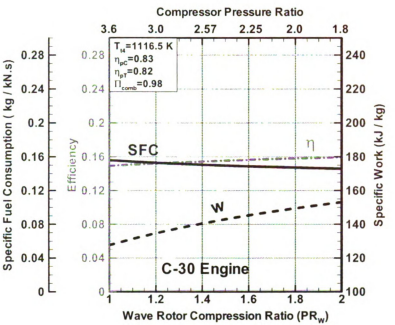

Figure 46: Thermal efficiency, specific work, and *SFC* for the wave-rotor-topped C-30 engine versus the wave rotor pressure ratio and compressor pressure ratio, Case B consideration

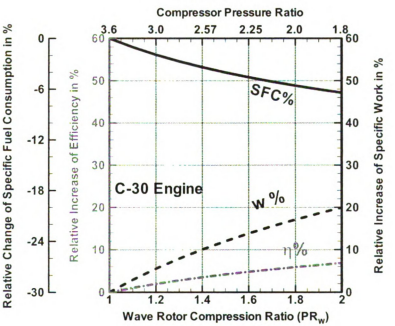

Figure 47: Relative values of thermal efficiency, specific work, and *SFC* for the wave-rotor-topped C-30 engine versus the wave rotor pressure ratio and compressor pressure ratio, Case B consideration

- **Comparison of Case A with Case B**

The performance enhancement of Case A and Case B can be compared visually by using the plots in Figure 48 and Figure 49 for both C-30 and C-60 engines, respectively. For Case B the results are shown with dashed lines and the corresponding compressor ratio is shown in the upper scale in orange. The corresponding overall pressure ratio for Case A is shown in purple and the results are shown with solid lines. Case A clearly shows a more beneficial performance enhancement than Case B.

- **Cases C, D, and E**

The actual T-s diagrams of the baseline engines and the wave-rotor-topped engines for Cases C, D, and E are shown in Figure 50 to Figure 52, respectively. More detailed documentation of these cases are not presented here. The reader is referred to Ref. [230]. Instead, numerical values of the predicted performance enhancement of all five investigated cases with a wave rotor pressure ratio of 1.8 are summarized in Table 2. In this table, Π_T represents the turbine pressure ratio. Subscript "gain" indicates the relative increase of thermal efficiency and specific work and decrease of *SFC*. Table 2 shows that Case A gives the highest performance increase for both baseline engines. After Case A, Case D gives the highest overall performance for the C-30 engine as for the C-60 engine. However, Case E provides the second highest thermal efficiency and the lowest *SFC* for the C-60 engine.

Figure 53 and Figure 54 show maps of the relevant design space for Cases A, B, and D for each engine. The only fixed parameters are turbine inlet temperature, the polytropic efficiencies of the compressor and turbine corresponding to the respective baseline engine, and the combustion chamber pressure loss as indicated in the upper right corner legend of each map. Performance maps valid for Cases C and E of the C-30 and the C-60

engines are shown in Figure 55 and Figure 56 which have lower turbine inlet temperatures than that indicated in Figure 53 and Figure 54. Instead, Cases C and E have the same combustion end temperature as the baseline engine, as indicated in the upper right hand corner of these maps.

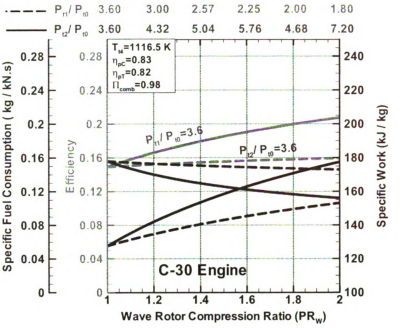

Figure 48: Thermal efficiency, specific work, and *SFC* for the wave-rotor-topped C-30 engine versus the wave rotor pressure ratio and overall pressure ratio for Case A (solid) and versus wave rotor pressure and compressor pressure ratio for Case B (dashed)

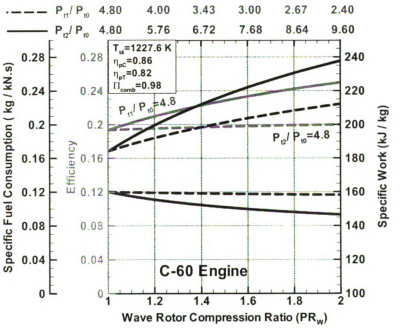

Figure 49: Thermal efficiency, specific work, and *SFC* for the wave-rotor-topped C-60 engine versus the wave rotor pressure ratio and overall pressure ratio for Case A (solid) and versus wave rotor pressure and compressor pressure ratio for Case B (dashed)

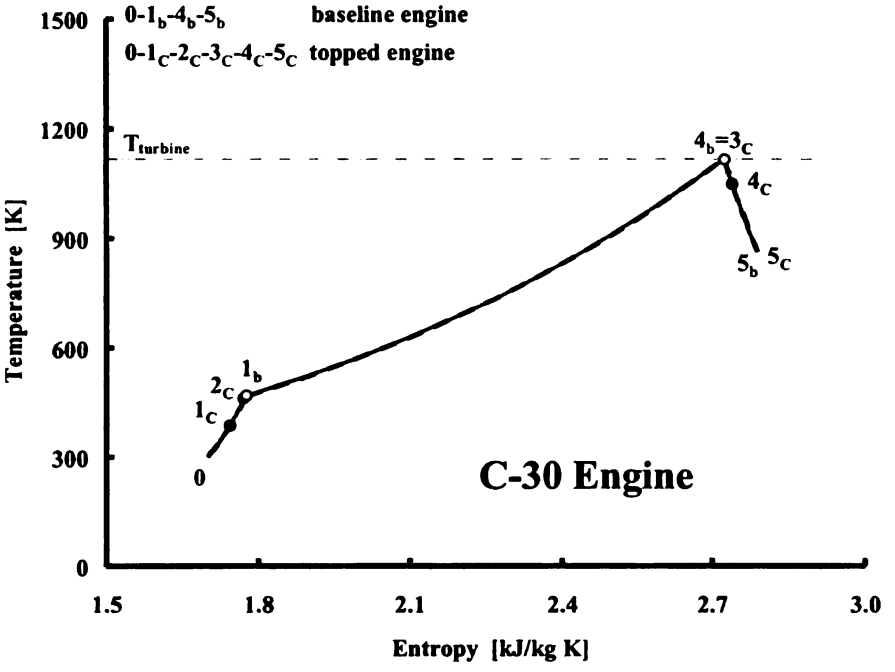

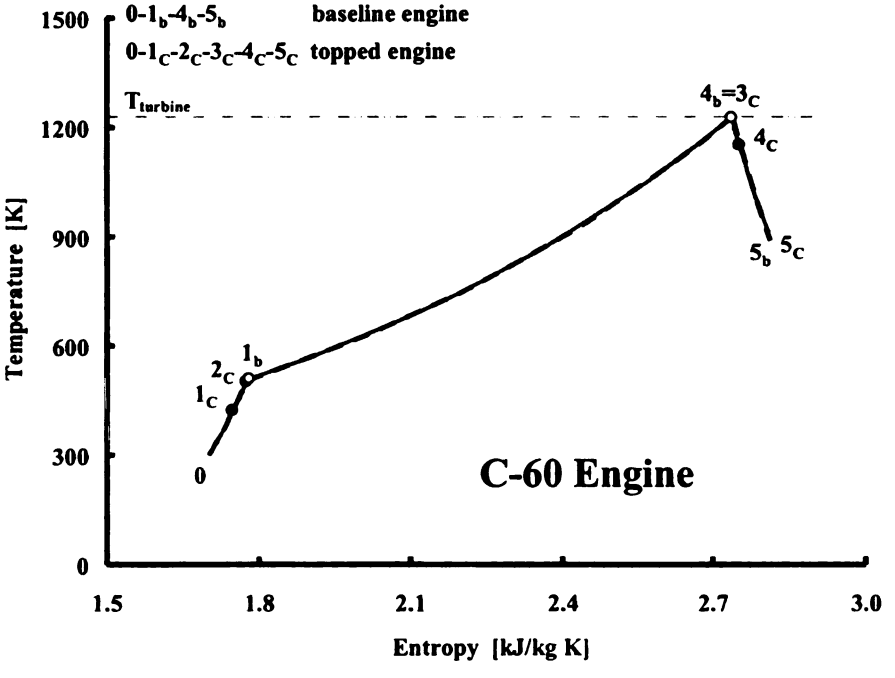

Figure 50: T-s diagrams for the C-30 and C-60 wave-rotor-topped engines for Case C implementation

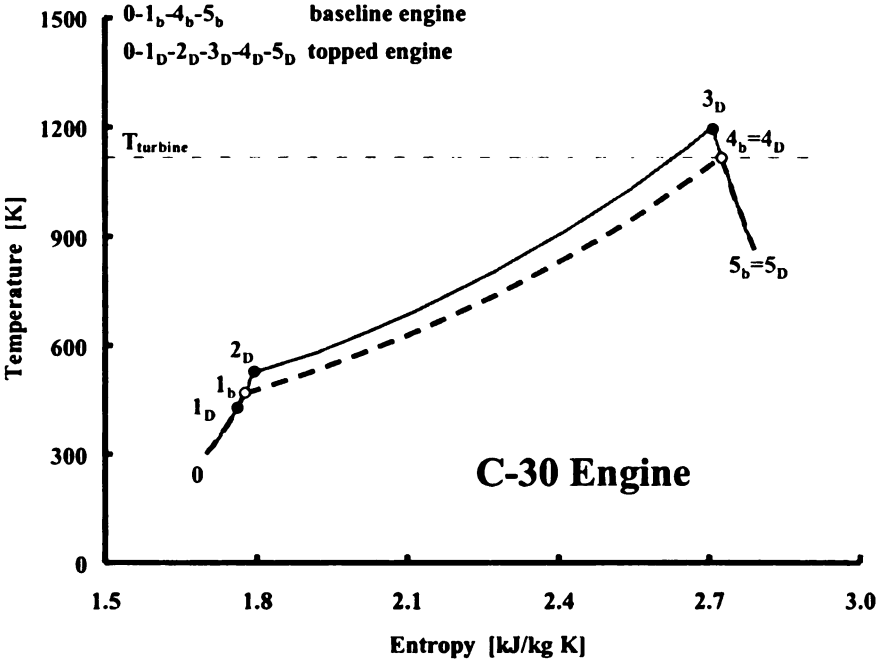

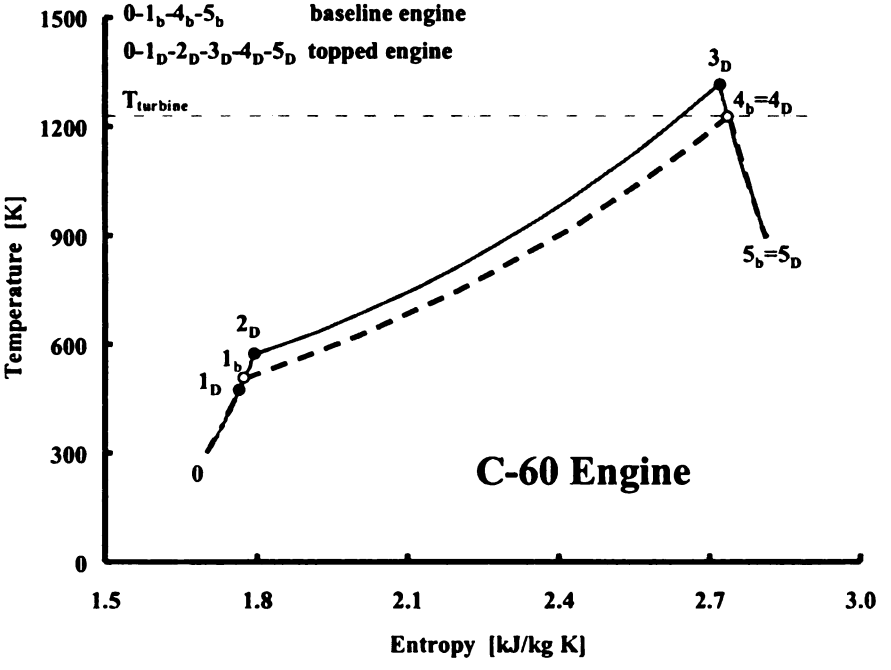

Figure 51: T-s diagrams for the C-30 and C-60 wave-rotor-topped engines for Case D implementation

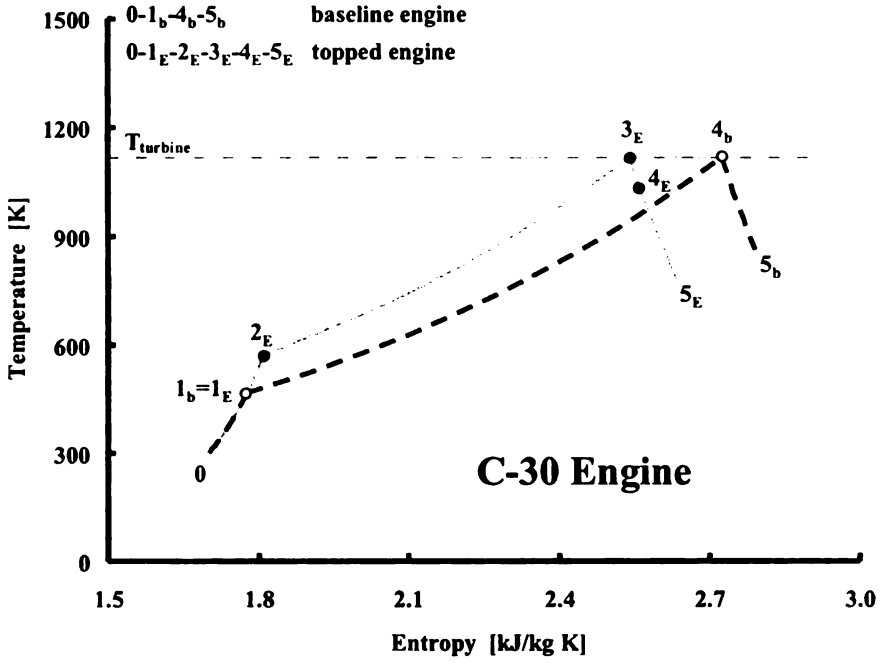

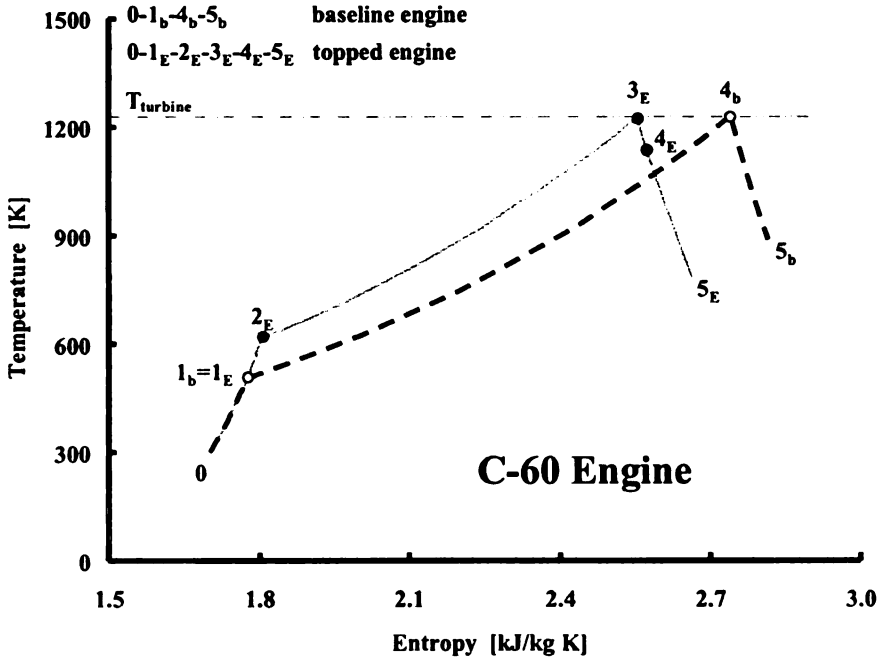

Figure 52: T-s diagrams for the C-30 and C-60 wave-rotor-topped engines for Case E implementation

Table 2: Performance comparison between baseline engines and five cases of wave-rotor-topping with a wave rotor pressure ratio of 1.8

Identical to baseline engine are:	Case **A** • compressor • turbine inlet temp.		Case **B** • overall press. ratio • turbine inlet temp.		Case **C** • combustor		Case **D** • turbine		Case **E** • compressor • combustion end temp.		**Baseline**	
Engines	C-30	C-60	C-30	C-60	C-30	C-60	C-30	C-60	C-30	C-60	C-30	C-60
T_{t4} [K]	1116	1228	1116	1228	1044	1149	1116	1228	1027	1132	1116	1228
q [kJ/kg]	855	952	946	1047	857	950	894	993	747	833	855	952
Π_C	3.60	4.80	2.00	2.67	2.00	2.67	2.84	3.77	3.60	4.80	3.60	4.80
Π_T	4.38	5.87	2.60	3.48	2.55	3.41	3.53	4.70	4.24	5.70	3.53	4.70
w_C [kJ/kg]	167	206	81	116	81	116	131	167	167	206	167	206
w_T [kJ/kg]	338	437	231	324	211	298	295	391	305	396	295	391
w [kJ/kg]	**171**	**231**	**150**	**208**	**130**	**182**	**165**	**224**	**137**	**190**	**128**	**184**
SFC[kg/kN.s]	**0.116**	**0.095**	**0.147**	**0.117**	**0.153**	**0.121**	**0.126**	**0.103**	**0.126**	**0.102**	**0.156**	**0.120**
η	**0.200**	**0.242**	**0.158**	**0.199**	**0.151**	**0.192**	**0.184**	**0.225**	**0.184**	**0.227**	**0.149**	**0.194**
$(w)_{gain}$ [%]	**33.8**	**25.1**	**17.1**	**13.0**	**1.7**	**-1.1**	**29.1**	**21.5**	**7.7**	**2.9**		
$(SFC)_{gain}$ [%]	**25.2**	**20.1**	**5.5**	**2.6**	**1.4**	**-0.8**	**19.0**	**14.1**	**18.9**	**14.9**		
$(\eta)_{gain}$ [%]	**33.8**	**25.1**	**5.9**	**2.7**	**1.5**	**-1.8**	**23.5**	**16.5**	**23.4**	**17.5**		

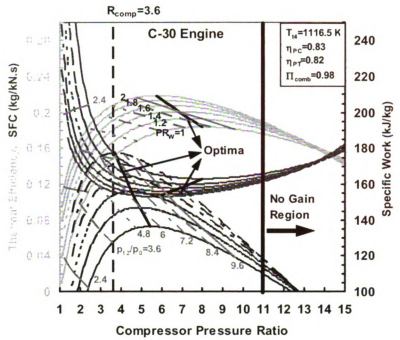

Figure 53: Performance map for wave-rotor-topping of the C-30 engine, Cases A, B, and D

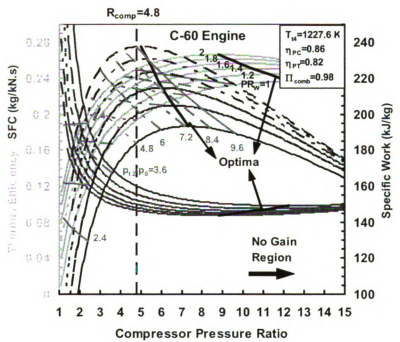

Figure 54: Performance map for wave-rotor-topping of the C-60 engine, Cases A, B, and D

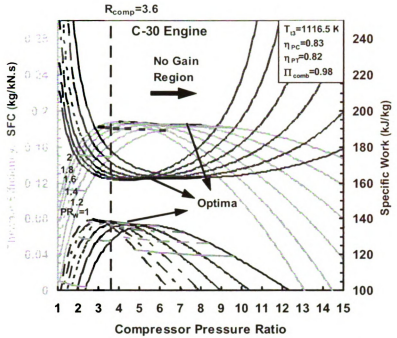

Figure 55: Performance map for wave-rotor-topping of the C-30 engine, Cases C and E

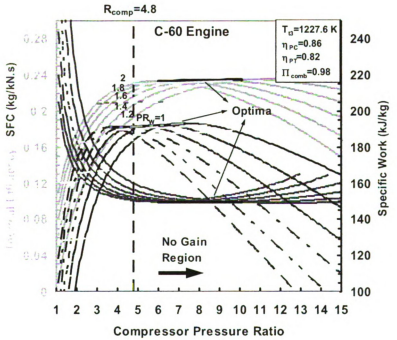

Figure 56: Performance map for wave-rotor-topping of the C-60 engine, Cases C and E

The maps allow predicting the performance of the wave-rotor-enhanced engine in terms of thermal efficiency (green), specific work (blue), and *SFC* (red) for any combination of the compressor pressure ratio (abscissa) and the wave rotor pressure ratio PR_W (parameter labeled in black). In these maps, the multiplication of compressor pressure ratio p_{t1}/p_0 and wave rotor pressure ratio PR_W determines the overall cycle pressure ratio p_{t2}/p_0 (orange). The locus of optimum compressor pressure ratio points (for highest thermal efficiency and specific work at each achievable wave rotor pressure ratio) are connected by black solid lines. The optima for *SFC* are found at the same combination of the compressor pressure ratio and PR_W as the optima of the thermal efficiency.

Such maps are not only very useful to explore the possible enhancement of already existing baseline engines, but they also serve well for selecting a design point or region for designing a new wave-rotor-topped engine. In all plots, the performance points of the baseline engine (PR_W=1) and the wave-rotor-enhanced engines of all cases with a wave rotor pressure ratio of PR_W=1.8 can be found. For instance in Figure 53 and Figure 54, starting from the performance point of the baseline engine, the performance values for Case A are found by moving vertically upwards (e.g. along the dashed line for constant compressor pressure ratio p_{t1}/p_0) until the corresponding performance curve of the expected wave rotor pressure ratio is crossed. Case B is found by moving along a line of constant overall pressure ratio p_{t2}/p_0 (orange).

The results indicate that for every compressor pressure ratio in each design space shown here, the performance of the topped engine is always higher than that of the corresponding baseline engine with the same compressor pressure ratio (Case A

consideration). The increase of PR_W always increases the performance. However, for higher compressor pressure ratios the benefit of using a wave rotor progressively diminishes. In fact, for compressor pressure ratios greater than around 11, almost no benefit can be obtained for the C-30 engine. An identical statement applies to the C-60 engine for compressor pressure ratios above around 15. The benefit is clearly the greatest for lower compressor pressure ratios. This suggests that the wave-rotor-topping for microturbines with low compressor pressure ratios can produce the greatest relative benefit. Moreover, as expected and known for baseline engines ($PR_W = 1$), it is also true for wave-rotor-topped engines that the compressor pressure ratio for the maximum specific work is always less than that of the maximum thermal cycle efficiency. However, with increasing wave rotor pressure ratio, the optima come closer together, while moving towards lower compressor pressure ratio. This can be viewed as an additional advantage for applying wave rotors to small gas turbines with low compressor pressure ratios. So as the plots show, adding a wave rotor with a 1.8 pressure ratio to C-30 or C-60 baseline engines with a compressor pressure ratio $p_{t1}/p_0 = 3.6$ or $p_{t1}/p_0 = 4.8$ respectively, already brings the design point into the optimum range for highest specific work and nearly half way closer to the optimum for highest thermal efficiency.

4.2.4 Comparison Between Adding a Second Compressor Stage with Wave-Rotor-Topping

The wave-rotor-topping competes mainly against adding a second compressor stage to the single stage baseline engine. In this competition one major advantage of the wave-rotor-topping is that the wave rotor favorably operates mechanically independent from the high-speed engine shaft. Therefore, adding a retrofit wave rotor does not require the redesign of the challenging dynamic system. Even if the compressor or turbine wheel is

adapted subsequently to utilize the full potential of the wave-rotor-topping, the dynamic system may change but not as dramatically as if a second compressor stage was added. Thus, by default the wave rotor is a system for achieving similar thermodynamic advantages as by adding a second compressor stage or a high pressure spool, but with many fewer dynamic challenges.

To justify the wave-rotor-topping approach further, the performance results of both competing solutions are compared below. For the addition of a second compressor stage, performance data are calculated for the five most probably relevant pressure ratios of the second stage described here:

- $\Pi_{C2}=PR_W$

A (perhaps) logical way to compare both systems would be to assume the same compression ratio for the second compressor stage as for the wave rotor. Hence the compression ratio of the second compressor stage would be $\Pi_{C2}=1.8$, because the assumed wave rotor compression ratio is $PR_W=1.8$.

- $w_{C2}=w_{C1}$

More likely, when the effort of adding a second compressor stage is undertaken, the designer would not limit the pressure ratio of the second stage to $\Pi_{C2}=1.8$. It might be desired to a add second compressor wheel that is similar to the existing first stage (or the same) for reasons such as using existing experience, or producing both wheels cost effectively as identical wheels, or producing them geometrically similar using the same or slightly modified tools. This approach can be modeled by setting the compressor shaft work of the second stage equal to that of the first stage, simulating the same angular momentum change of the flow in both stages at the same shaft. Because the inlet air

temperature for the second stage is much higher, the pressure ratio of the second stage is less than that of the first stage $\Pi_{C2} < \Pi_{C1}$.

- $\Pi_{C2} = \Pi_{C1}$

Alternatively, it could simply be assumed that the pressure ratio of the second stage is equal to the pressure ratio in the first stage. This is a common design approach.

- $\Pi_C (w)_{opt.}$ and $\Pi_C (\eta)_{opt.}$

It might be desirable to compare the wave-rotor-topped engine with a two-stage compressor engine that has an overall pressure ratio $\Pi_{C2} \cdot \Pi_{C1}$ corresponding to the optimum for maximum specific work $\Pi_C (w)_{opt}$ or the optimum for maximum efficiency $\Pi_C (\eta)_{opt}$. The resulting values for specific work and thermal efficiency respectively are the maximum values actually obtainable by enhancing the pressure ratio of a conventional compressor. The values of $\Pi (w)_{opt}$ and $\Pi (\eta)_{opt}$ can be found by using performance maps in Figure 53-Figure 56 and following the curves for $PR_W = 1$ to their optimum points.

In all performance calculations above, it is assumed that the polytropic compression efficiency of the second stage is equal to that of the single stage baseline compressor. The performance values of all these two-stage-compressor cases as well as intermediate cases can also be read off the performance maps in Figure 53 to Figure 56 following the curves for $PR_W = 1$. The compressor pressure ratio at the abscissa then corresponds to the overall pressure ratio $\Pi_{C2} \cdot \Pi_{C1}$. The performance results are compiled for the C-30 engine in Table 3 and for the C-60 engine in Table 4 for all five two-stage-compressor cases described above. The two-stage-compressor engines are compared with the wave-rotor-topped engine Cases A and E. These cases are more suitably compared with two-stage-

compressor engines for a few reasons. Both cases employ the same compressor as the first stage of the baseline engines. Case A has shown the highest performance improvement and it represents the maximum performance achievable for a wave-rotor-topping cycle. In Case E, the baseline compressor is the same and the combustion end temperature is the same as for the baseline engine, not requiring any thermal enhancement of the combustor. It is understood that this is exactly the case for the two-stage-compressor engine, where the combustion end temperature is simultaneously the turbine inlet temperature (which is never the case for wave-rotor-topping). This has been illustrated in Figure 57 that compares the T-s curves of the baseline cycle, the modified cycle with the two-stage compressor, and the wave-rotor-topped cycle Case E with a wave rotor pressure ratio of 1.8 for the C-30 engine. The two-stage-compressor values may also be compared with the wave-rotor-topping Cases B, C and D using the supplied data in Table 2.

Table 3: Performance comparison between adding a conventional second compressor stage and wave-rotor-topping Case A and E with a wave rotor pressure ratio of 1.8; baseline engine C-30

C-30	Two-Stage Compressor					Wave Rotor Topped		Baseline
Feature	$\Pi_C(w)_{opt.}$	$\Pi_{C2}=PR_W$	$\Pi_C(\eta)_{opt.}$	$w_{C2}=w_{C1}$	$\Pi_{C2}=\Pi_{C1}$	Case **A**	Case **E**	
Π_{C2}	1.52	1.8	2.22	2.42	3.6	1.8	1.8	
w [kJ/kg]	136	135	129	125	95	171	137	128
SFC[kg/kN.s]	0.133	0.128	0.126	0.127	0.141	0.116	0.126	0.156
η	0.175	0.181	0.184	0.183	0.164	0.200	0.184	0.149
$(w)_{gain}$ [%]	**6.3**	**5.5**	**0.8**	**-2.3**	**-25.8**	**33.8**	**7.7**	
$(SFC)_{gain}$ [%]	**14.5**	**17.9**	**18.9**	**18.6**	**9.6**	**25.2**	**18.9**	
$(\eta)_{gain}$ [%]	**17.5**	**21.5**	**23.4**	**22.8**	**10.1**	**33.8**	**23.4**	

Table 4: Performance comparison between adding a conventional second compressor stage and wave-rotor-topping Case A and E with a wave rotor pressure ratio of 1.8; baseline engine C-60

C-60	Two-Stage Compressor					Wave Rotor Topped		Baseline
Feature	$\Pi_C(w)_{opt.}$	$\Pi_{C2}=PR_W$	$\Pi_C(\eta)_{opt.}$	$w_{C2}=w_{C1}$	$\Pi_{C2}=\Pi_{C1}$	Case A	Case E	
Π_{C2}	1.52	1.8	2.55	2.79	4.8	1.8	1.8	
w [kJ/kg]	193	192	179	173	118	231	190	184
SFC[kg/kN.s]	0.105	0.101	0.098	0.098	0.115	0.095	0.102	0.120
η	0.222	0.229	0.236	0.236	0.203	0.242	0.227	0.194
$(w)_{gain}$ [%]	**4.9**	**4.3**	**-2.7**	**-6.0**	**-35.9**	**25.1**	**2.9**	
$(SFC)_{gain}$ [%]	**12.5**	**15.8**	**18.3**	**18.3**	**4.2**	**20.1**	**14.9**	
$(\eta)_{gain}$ [%]	**14.4**	**18.0**	**21.6**	**21.6**	**4.6**	**25.1**	**17.5**	

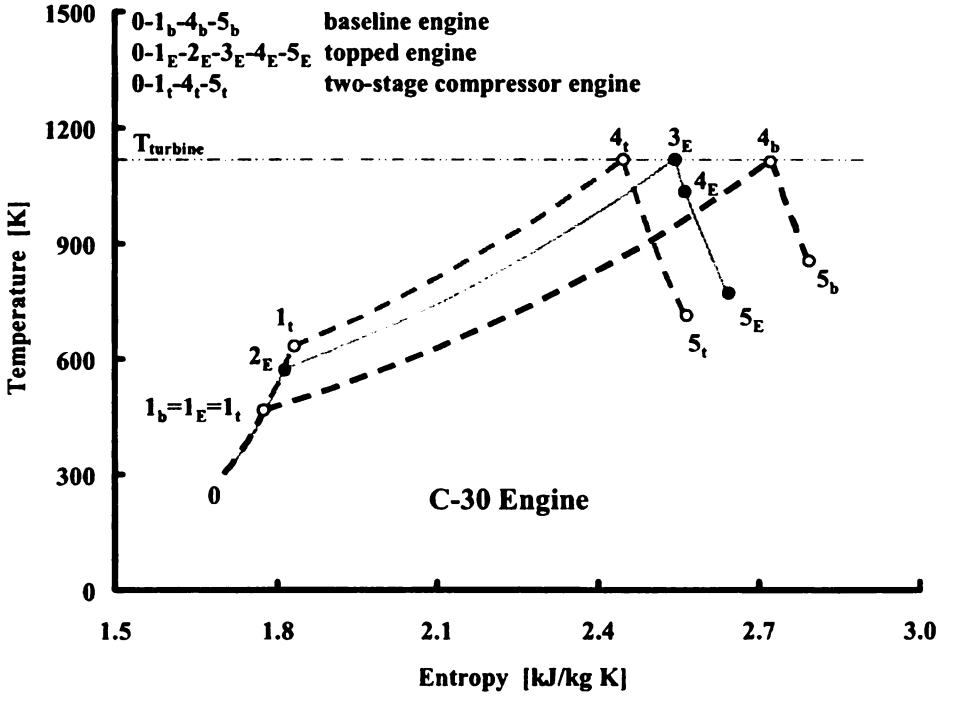

Figure 57: T-s diagrams for baseline cycle, conventional cycle with two-stage compressor (double compression work) and wave-rotor-topped cycle Case E with PR_W=1.8, C-30 engine

Table 3 and Table 4 show that the gain in predicted thermal efficiency, specific shaft work, and *SFC* of the wave-rotor-topped engine in Case A is always greater than any obtainable values for the two-stage-compressor engine. A look at the maps in Figure 53 and Figure 54 clearly verifies this for the relevant design space. In these plots, the performance points for Case A lie well above any point at the curves for $PR_W = 1$ where all the performance data of the two-stage-compressor engine can be found. For the C-30 engine, Case E in Table 3 still shows a higher performance than any two-stage-compressor configuration. For the C-60 engine, however, Case E in Table 4 achieves nearly the same performance as a two-stage-compressor engine with a second-stage compression ratio in the range between the two optima for maximum specific work and maximum thermal efficiency (minimum *SFC*), Π_{C2}=1.52...2.55. Finally, the results show again that the compressor pressure ratio for the maximum specific work is always less than that of the maximum thermal cycle efficiency (minimum *SFC*).

Besides the drawbacks of the two-stage-compressor implementation already mentioned, a second compressor stage adds not only a second compressor wheel, it always requires an enhanced combustor capable for higher combustion pressure and a turbine adapted to considerably a higher pressure ratio. Finally it requires an enhanced engine shaft, transmitting much more compression work. This situation is quite opposite for the wave-rotor-enhanced engine in which the transmitted compression work for all considered wave-rotor-topping cases is always either less (Cases B, C, and D) or the same as for the baseline engine (Cases A and D). The combustion pressure ratio can be kept the same (Cases B and C). Furthermore, the pressure ratio that has to be accommodated in the turbine is always less for the wave-rotor-topped engine than for the

two-stage-compressor engine with the same or greater overall pressure ratio, likely causing fewer problems when adapting the turbine. For the wave-rotor-topping Cases B and C, the turbine pressure ratio is even less than that of the single stage baseline engine. Additionally, in Cases C and E the wave-rotor-topping even lowers the turbine inlet temperature, which allows the designer to use a turbine made of a cheaper material.

4.2.5 Substituting the Compressor in the C-60 Engine with the C-30 Compressor plus Wave Rotor

An interesting practical engineering option is to substitute the current compressor of the C-60 microturbine with the smaller and cheaper compressor designed for the C-30 microturbine by adding a wave rotor to obtain the same overall compression ratio of 4.8 required for the C-60 engine. This case is similar to the Case E shown in Table 2, only the compressor polytropic efficiency is switched from 85.9% for the C-60 compressor to 82.9% for the C-30 compressor. Also different from the Case E, the wave rotor pressure ratio needs to be adapted to 1.33 (instead of the value 1.8 in Table 2) to obtain the C-60 baseline overall pressure ratio of 4.8 in combination with the C-30 compressor that has a compression ratio of 3.6. For such a modified C-60 engine, Figure 58 shows the thermal efficiency, specific work, and *SFC* as a function of wave rotor compression ratio (lower abscissa) and compressor pressure ratio (upper abscissa) if the overall compression ratio is fixed at 4.8 and the compressor has a polytropic efficiency of η_{PC}=0.829 of the C-30's compressor. It is seen that by using a wave rotor with a pressure ratio of 1.33 (orange points), the modified C-60 engine would have an thermal efficiency of 19.1%, a specific work of 190 kJ/kg, and *SFC* of 0.122 kg/kN.s. Compared to the C-60 baseline engine (yellow points where PR_W =1) with a thermal efficiency, specific work, and *SFC* of 19.4% and 184 kJ/kg, and 0.120 kg/kN.s, respectively, the topped engine would not

enhance the efficiency and *SFC*, but the specific work would increase by about 3%. Furthermore, this engine would use a smaller compressor that has a lower manufacturing cost and already exists. Other, more advantageous combinations with an even smaller but newly designed compressor and higher wave rotor pressure ratio are also conceivable, as shown in Figure 58.

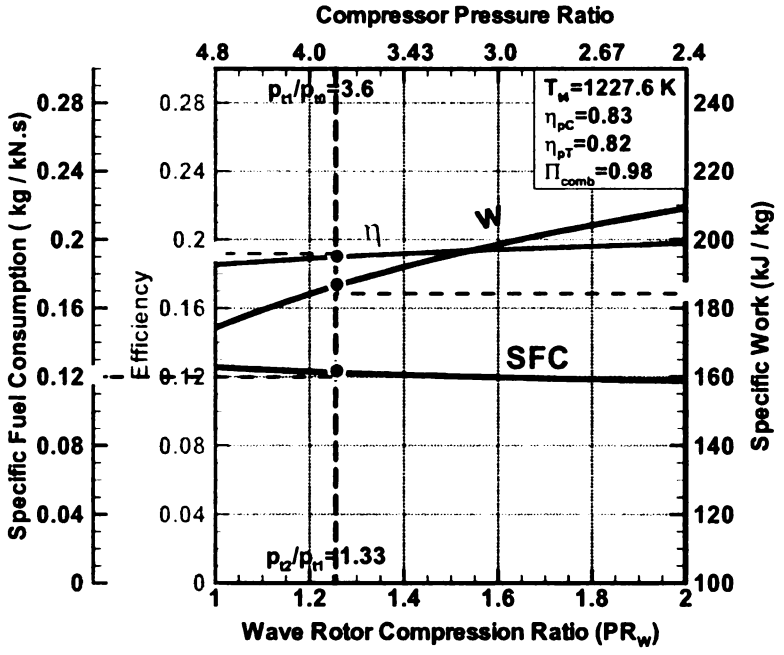

Figure 58: Thermal efficiency, specific work, and specific fuel consumption of the wave-rotor-topped C-60 engine using the C-30 compressor versus wave rotor compression ratio and compressor pressure ratio for an overall pressure ratio fixed at 4.8 (yellow points for original C-60 baseline engine, orange points for wave-rotor-topped C-60 engine with C-30 compressor)

4.2.6 Effect of Compressor Inlet Temperature

It is well known that the performance of gas turbines is affected by varying the ambient conditions [231]. For instance, both the thermal efficiency and output power of a gas turbine engine with a fixed turbine inlet temperature decrease when the compressor inlet temperature rises. This is disadvantageous if a stationary gas turbine is installed in

hot-weather locations. Under these conditions, it is proved in the following that the wave-rotor-topping is even more advantageous.

For simulation it is assumed that the compressor isentropic efficiency stays constant although a slight decrease might be expected. It is furthermore assumed that the specific compression work stays constant since the compressor geometry does not change. Hence, the compressor pressure ratio decreases upon increase of the ambient temperature from basic thermodynamics. For the baseline engine it is obvious that this results in a lower turbine pressure ratio and lower specific work produced by the engine. The results for compressor inlet temperatures of 250 K, 300 K, and 350 K are compiled in Table 5 for the C-30 engine and in Table 6 for the C-60 engine. The corresponding performance values of the wave-rotor-enhanced engines of Cases A and B, which are the most considered cases discussed in the literature, are also shown in these tables.

For the wave-rotor-enhanced engines the general trend is the same. However, while the absolute performance degrades at higher ambient temperatures for baseline and topped engines, the performance gains of the enhanced engines relative to the baseline engines increase, making this technology more desirable for applications under hot-weather conditions. For a range of wave rotor compression ratios PR_W =1...2, this reversed effect is visualized in Figure 59 and Figure 60, especially in the lower part showing the relative gains of the topped engines. While Figure 59 shows the absolute gain and the relative performance enhancement for Case A, Figure 60 illustrates similar results for Case B.

Table 5: Ambient temperature effect on performance - comparison between baseline engines and Cases A and B of wave-rotor-topping with PR_W =1.8; baseline engine C-30

C-30	T_0 = 250 K			T_0 = 300 K			T_0= 350 K		
Cases	Baseline	Case **A**	Case **B**	Baseline	Case **A**	Case **B**	Baseline	Case **A**	Case **B**
w [kJ/kg]	168	217	190	128	171	150	95	132	117
SFC[kg/kN.s]	0.125	0.097	0.121	0.156	0.116	0.147	0.195	0.141	0.179
η	0.185	0.239	0.192	0.149	0.200	0.158	0.119	0.165	0.130
$(w)_{gain}$ [%]		29.0	13.0		33.8	17.1		38.6	23.1
$(SFC)_{gain}$ [%]		22.5	3.6		25.2	5.5		27.8	8.6
$(\eta)_{gain}$ [%]		29.0	3.8		33.8	5.9		38.6	9.4

Table 6: Ambient temperature effect on performance - comparison between baseline engines and Cases A and B of wave-rotor-topping with PR_W =1.8; baseline engine C-60

C-60	T_0 = 250 K			T_0 = 300 K			T_0= 350 K		
Cases	Baseline	Case **A**	Case **B**	Baseline	Case **A**	Case **B**	Baseline	Case **A**	Case **B**
w [kJ/kg]	234	285	258	184	231	208	144	185	168
SFC[kg/kN.s]	0.010	0.082	0.098	0.120	0.095	0.117	0.144	0.113	0.139
η	0.232	0.283	0.237	0.194	0.242	0.199	0.161	0.206	0.167
$(w)_{gain}$ [%]		21.8	10.5		25.1	13.0		28.2	16.4
$(SFC)_{gain}$ [%]		17.9	1.8		20.1	2.6		22.0	4.0
$(\eta)_{gain}$ [%]		21.8	1.8		25.1	2.7		28.2	4.2

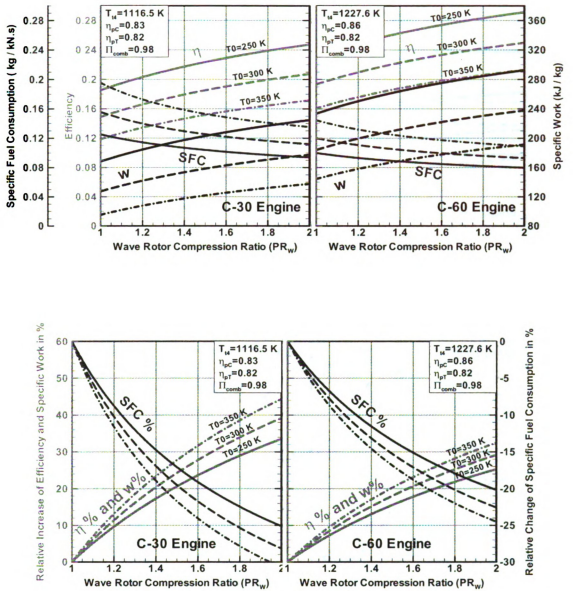

Figure 59: Effect of ambient temperature: absolute and relative changes of thermal efficiency, specific work, and *SFC* versus wave rotor pressure ratio for Case A

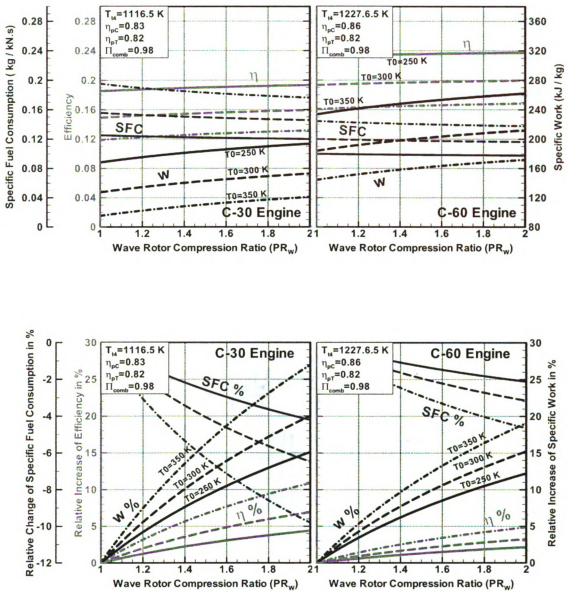

Figure 60: Effect of ambient temperature: absolute and relative changes of thermal efficiency, specific work, and *SFC* versus wave rotor pressure ratio for Case B

4.3 Gas Turbine with Recuperation

Figure 61 shows a block diagram of a recuperated gas turbine topped with a four-port wave rotor. The wave rotor is placed after the compressor and before the recuperator. Figure 62 and Figure 63 show T-s diagrams for the C-30 baseline engine and the corresponding wave-rotor-topped engine for Cases A and B, respectively. Path $0\text{-}1_b\text{-}2_b^*\text{-}4_b\text{-}5_b\text{-}5_b^*$ represents the baseline cycle and path $0\text{-}1_i\text{-}2_i\text{-}2_i^*\text{-}3_i\text{-}4_i\text{-}5_i\text{-}5_i^*$ (i=A and B) indicates the wave-rotor-topped cycles. Only Cases A and B are considered in this study due to their high potential for performance improvement under recuperated conditions. All calculations have been presented only for the C-30 engine, while the conclusions are valid for the C-60 engine, too.

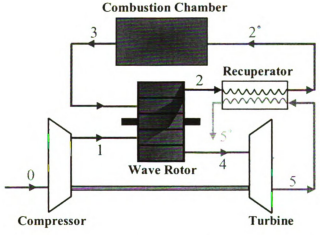

Figure 61: Schematic of a recuperated gas turbine topped by a four-port wave rotor

Compared to the baseline engine without the recuperator, the recuperated baseline engine here has a lower turbine inlet pressure due to the pressure loss of the recuperator air-side. However, it has a higher turbine outlet pressure due to the pressure loss of the recuperator gas-side.

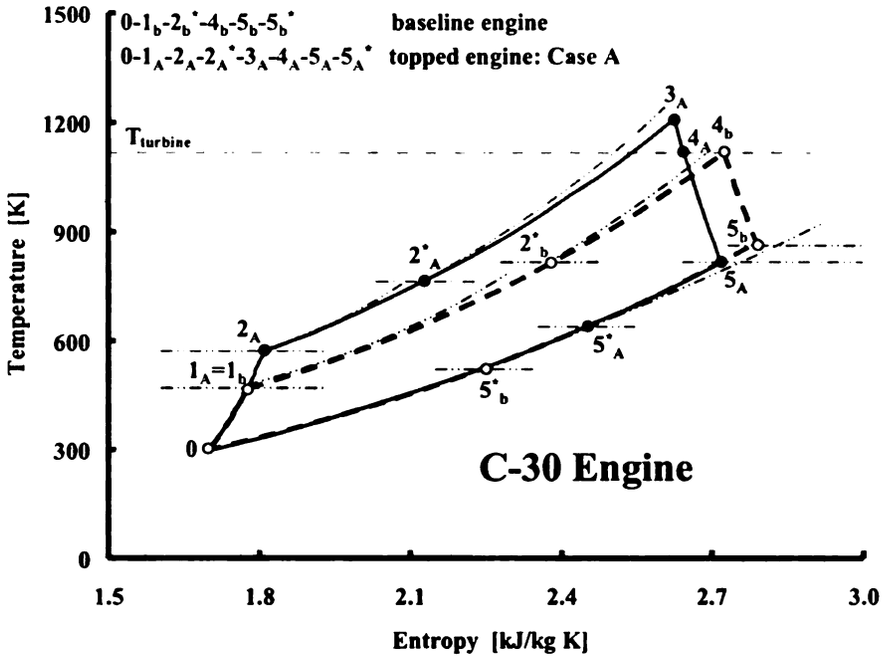

Figure 62: T-s diagrams for recuperated baseline and wave-rotor-topped cycles, Case A

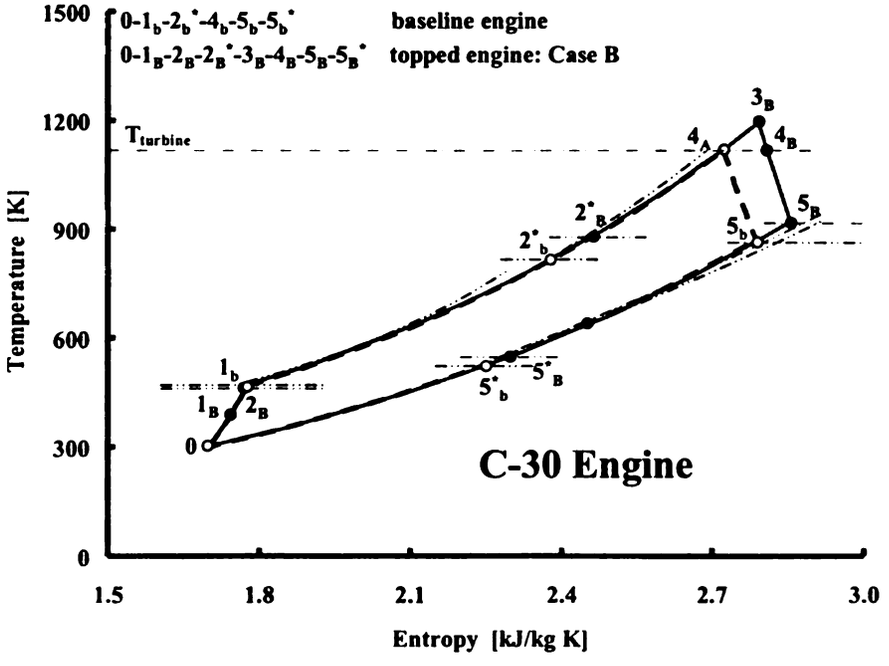

Figure 63: T-s diagrams for recuperated baseline and wave-rotor-topped cycles, Case B

4.3.1 Thermodynamic Calculations

In this section, calculations have been performed for both Cases A and B of the C-30 engine equipped with a recuperator. As before, in the wave-rotor-topping cycle, it is assumed that the compressor inlet condition, turbine inlet temperature, compressor and turbine polytropic efficiencies remain unchanged and are the same as for the baseline engines.

For the recuperated cycle, the pressure losses across the air and gas sides of the recuperator are assumed the same and equal to 2% ($\Pi_{recup\text{-}air} = \Pi_{recup\text{-}gas} = 0.98$). The effectiveness of the recuperator is considered to be η_{recup}=90%. These values have been selected based on typical existing recuperators. The major challenges in providing a recuperator with greater effectiveness are size and cost. For stationary applications, size and weight are not critical, but for mobile applications these limitations produce recuperator effectiveness commonly less than 90% [224].

Complying with Figure 61, the following steps are used to calculate the thermodynamic properties of the gases in different states of the topped cycle [232]:

- **Path 0-1: Compressor**

Equations (21) to (24) are again used to calculate the air properties at the compressor exit.

- **Path 1-2: Compression in the Wave Rotor**

As shown before, Eqs. (25) and (26) are used to calculate the air properties after the wave rotor compression process.

- **Path 2-2*: Recuperator Air-Side**

The recuperator effectiveness based on the actual and maximum heat transfer from the turbine exhaust gas to the air can be expressed as:

$$\eta_{recup} = \frac{T_{t2^*} - T_{t2}}{T_{t5} - T_{t2}} \tag{48}$$

Using this equation, the temperature at the exit of the recuperator air-side (T_{t2^*}) becomes:

$$T_{t2^*} = T_{t2} + \eta_{recup}(T_{t5} - T_{t2}) \tag{49}$$

In this equation, the turbine outlet temperature (T_{t5}) is still an unknown parameter. More equations are required to find the unknown values T_{t2^*} and T_{t5}. These additional equations will be derived later. The corresponding pressure at state 2^* is:

$$\frac{p_{t2^*}}{p_0} = \Pi_{recup-air}\frac{p_{t2}}{p_0} = \Pi_{recup-air} PR_W \Pi_C \tag{50}$$

where $\Pi_{recup\text{-}air} = p_{t2^*}/p_{t2}$ represents the pressure loss across the air side of the recuperator.

- **Path 2^*-3: Combustion Chamber**

Similar to Eq. (27), the following equation is used to calculate the fuel/air ratio:

$$\eta_Q f\, h_{PR} = (1+f)Cp_{gas}T_{t3} - Cp_{air}T_{t2^*} \tag{51}$$

where T_{t3} is an unknown value. However, f can be alternatively expressed as follows:

$$\eta_Q f\, h_{PR} = (1+f)Cp_{gas}T_{t4} + w_{WE} - w_{WC} - Cp_{air}(T_{t2^*} - T_{t2}) - Cp_{air}T_{t1} \tag{52}$$

Since the net output work of the wave rotor is zero, f can be expressed as:

$$f = \frac{Cp_{gas}T_{t4} - Cp_{air}(T_{t2^*} - T_{t2}) - Cp_{air}T_{t1}}{\eta_Q h_{PR} - Cp_{gas}T_{t4}} \tag{53}$$

This expression also will be later used to find T_{t2^*}, T_{t5}, and f.

Now, the total pressure after the combustion chamber is obtained by:

$$\frac{p_{t3}}{p_0} = \frac{p_{t3}}{p_{t2^*}}\frac{p_{t2^*}}{p_0} = \Pi_{comb}\Pi_{recup-air} PR_W \Pi_C \tag{54}$$

- **Path 3-4: Expansion in the Wave Rotor**

The wave-rotor characteristic equation (38) is used to calculate the turbine inlet total pressure expressed in Eq. (41).

- **Path 4-5: Turbine**

The turbine total outlet pressure is:

$$\frac{p_{t5}}{p_0} = \frac{1}{\Pi_{recup-gas}} \frac{p_{t5^*}}{p_0} = \frac{1}{\Pi_{recup-gas}} \tag{55}$$

where $\Pi_{recup-gas} = p_{t5^*}/p_{t5}$ represents the pressure loss across the gas side of the regenerator. It is justified to assume that the total pressure of the gas leaving the recuperator (p_{t5^*}) is equal to the ambient pressure (p_0).

The turbine specific work according to pressure ratio across the turbine is calculated by using Eq. (42) where p_0 must be substituted by p_{t5}.

By obtaining the turbine specific work, the turbine total exit temperature (T_{t5}) is given as:

$$T_{t5} = T_{t4} - \frac{w_T}{(1+f)Cp_{gas}} = T_{t4} - \eta_T T_{t4} \left[1 - \left(\frac{p_{t5}/p_0}{p_{t4}/p_0} \right)^{\frac{\gamma_{gas}-1}{\gamma_{gas}}} \right] \tag{56}$$

Now, to find values of T_{t2^*}, T_{t5}, and f, it is necessary to use Eqs. (49), (53), and (56), along with Eqs. (38), (41), and (55). The procedure is now explained. Substituting Eq. (49) into (53) gives:

$$f = \frac{Cp_{gas} T_{t4} - \eta_{recup} Cp_{air} (T_{t5} - T_{t2}) - Cp_{air} T_{t1}}{\eta_Q h_{PR} - Cp_{gas} T_{t4}} \tag{57}$$

or,

$$T_{t5} = T_{t2} + \frac{Cp_{gas}\, T_{t4} - f(\eta_Q\, h_{PR} - Cp_{gas}\, T_{t4}) - Cp_{air}\, T_{t1}}{\eta_{recup}\, Cp_{air}} \tag{58}$$

Now, equating this equation with Eq. (56) results in:

$$T_{t2} + \frac{Cp_{gas}\, T_{t4} - f(\eta_Q\, h_{PR} - Cp_{gas}\, T_{t4}) - Cp_{air}\, T_{t1}}{\eta_{recup}\, Cp_{air}} = T_{t4} - \eta_T\, T_{t4}\left[1 - \left(\frac{p_{t5}/p_0}{p_{t4}/p_0}\right)^{\frac{\gamma_{gas}-1}{\gamma_{gas}}}\right] \tag{59}$$

Using Eqs. (41) and (55) gives:

$$\begin{aligned} &T_{t2} + \frac{Cp_{gas}\, T_{t4} - f(\eta_Q\, h_{PR} - Cp_{gas}\, T_{t4}) - Cp_{air}\, T_{t1}}{\eta_{recup}\, Cp_{air}} \\ &= T_{t4} - \eta_T\, T_{t4}\left[1 - \left(\frac{1}{\Pi_{recup-gas}\, PO \cdot \Pi_C}\right)^{\frac{\gamma_{gas}-1}{\gamma_{gas}}}\right] \end{aligned} \tag{60}$$

where PO is a function of f and is obtained from Eq. (38). The above equation computes f as a function of other known cycle parameters.

- **Path 5-5*: Recuperator Gas-Side**

The temperature of the gas leaving the recuperator (T_{t5*}) can be calculated by using the energy equation across the regenerator as follows:

$$Cp_{air}(T_{t2^*} - T_{t2}) = (1+f)\, Cp_{gas}(T_{t5} - T_{t5^*}) \tag{61}$$

This yields:

$$T_{t5^*} = T_{t5} - \frac{Cp_{air}}{Cp_{gas}} \frac{T_{t2^*} - T_{t2}}{1+f} \tag{62}$$

Now, it is possible to calculate the engine performance parameters as described before.

4.3.2 Predicted Performance Results

Implementing Case A for the C-30 recuperated engine, Figure 64 illustrates the variations of the cycle thermal efficiency (dash dot), specific work (dashed), and *SFC* (solid) with increasing wave rotor pressure ratio PR_W. For the baseline engines (without

the wave rotor, $PR_W = 1$), whereas the thermal efficiency of the recuperated cycle is much greater than that of the simple cycle (without the recuperator) its specific work is slightly less due to the pressure losses across the recuperator. With a conceivable wave rotor pressure ratio of 1.8, the thermal efficiency of the recuperated engine increases slightly from 24.8% to 26.6%. However, the specific work increases from 116 kJ/kg to 160 kJ/kg. The thermal efficiency of the recuperated cycle remains almost unchanged when the wave rotor is used, because the temperature difference between the air and the gas entering the recuperator of the topped engine (T_{t5A}-T_{t2A}) is much less than that of the baseline engine (T_{t5b}-T_{t1b}). This results in reduced recuperation, and hence the greater heat addition into the topped engine offsets the increased work output. This is in contrast to the unrecuperated engine where both the baseline and topped cycles have the same heat addition, as explained before. *SFC* for the recuperated engine slightly decreases from 0.094 kg/kN.s to 0.087 kg/kN.s. Again the increased heat addition into the recuperated topped cycle keeps *SFC* almost constant compared with the simple cycle, which is seen is Eq. (47).

The relative increases of thermal efficiency, specific work, and relative decreases of *SFC* are shown in Figure 65. Even higher than the unrecuperated engine discussed before, the specific work of the recuperated cycle shows a significant improvement of about 37.6%, but thermal efficiency and *SFC* are only about 7% greater than those for the baseline engine.

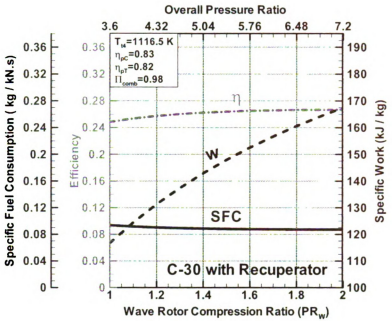

Figure 64: Thermal efficiency, specific work, and *SFC* of the enhanced C-30 recuperated engine versus the wave rotor pressure ratio and overall pressure ratio for Case A

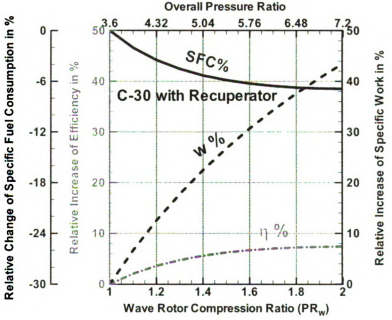

Figure 65: Relative values of thermal efficiency, specific work, and *SFC* of the enhanced C-30 recuperated engine versus the wave rotor pressure ratio and overall pressure ratio for Case B

Similar to Figure 64 and Figure 65, now Figure 66 and Figure 67 show the absolute and relative increases of the thermal efficiency (dash dot) and specific work (dashed), and the decrease of *SFC* (solid) upon implementing Case B to the C-30 recuperated engine. Similar to Case A, both the thermal efficiency and specific work are increasing functions of PR_W while *SFC* decreases. For $PR_W = 1.8$, the thermal efficiency of the simple cycle is increased from 24.8% to 27.3%. Similarly, the specific work is increased from 116 kJ/kg to 137 kJ/kg. Finally, the *SFC* is decreased from 0.094 kg/kN.s to 0.085 kg/kN.s for the recuperated cycle. Therefore, wave-rotor-topping of the recuperated engine gives a relative increase of 9.7% and 18% for the thermal efficiency and specific work, respectively, and an 8.7% reduction in *SFC*.

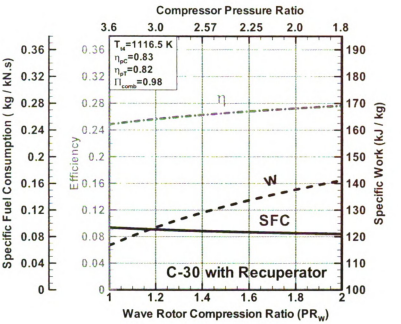

Figure 66: Thermal efficiency, specific work, and *SFC* of the enhanced C-30 recuperated engine versus the wave rotor pressure ratio and compressor pressure ratio for Case B

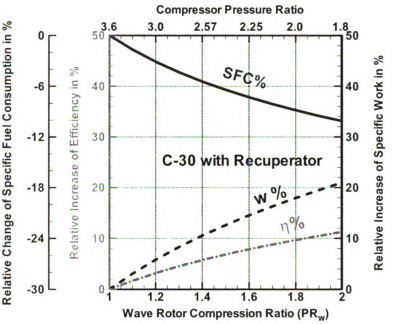

Figure 67: Relative values of thermal efficiency, specific work, and *SFC* of the C-30 recuperated engine topped with a wave rotor versus the wave rotor pressure ratio and compressor pressure ratio for Case B

Table 7 summarizes the results showing a comparison between performance improvements for these for implementations of both Cases A and B. It is seen from the table that the baseline engine with recuperation has a much higher efficiency (about twice) and lower *SFC* than those of the unrecuperated engine due to the heat addition reduction in the combustion process. Implementation of Case A into the baseline engine results in a significant performance improvement of the unrecuperated engine, however, the thermal efficiency and *SFC* improvements of the recuperated engine are lower than that of the specific work. In Case B, the topped cycle without the recuperator still benefits from the wave rotor even though the performance enhancement is less than that of Case A. However, the topped recuperated cycle has a higher performance compared to the unrecuperated engine and its thermal efficiency and *SFC* gains are even more than those of Case A. The results clearly demonstrate the benefit of implementing Case A for unrecuperated engines and implementing Case B for recuperated engines. Among all topping cycles, the best relative performance improvement is obtained with Case A topping of the unrecuperated engine.

A comparison between the recuperated baseline engine and the topped simple cycle engine (PR_W =1.8) reveals that for the specific example, the recuperator enhances the thermal efficiency and *SFC*, while the wave-rotor mostly enhances the specific work output. Therefore, substituting a recuperator with a wave rotor may be guided by a preference for high power output and reduced unit cost, considering that a recuperator contributes about 25-30% to the unit cost and a wave rotor may be cheaper. Finally, topping a recuperated gas turbine with a wave rotor can increase the performance especially if the topping cycle operates with the same turbine inlet temperature and same

overall pressure of the baseline engine (Case B implementation), which is preferable for the combustor and fuel injection design.

Table 7: Performance comparison between baseline engines and two cases of wave-rotor-topping with a wave rotor pressure ratio of 1.8

	Case **A**		Case **B**		**Baseline**	
Engines	Simple	Recuperated	Simple	Recuperated	Simple	Recuperated
Π_C	3.60	3.60	2.00	2.00	3.60	3.60
Π_T	4.38	4.19	2.60	2.49	3.53	3.39
q [kJ/kg]	855	603	946	505	855	470
w_C [kJ/kg]	167	167	81	81	167	167
w_T [kJ/kg]	338	328	231	219	295	284
w [kJ/kg]	**171**	**161**	**150**	**138**	**128**	**117**
SFC	**0.116**	**0.087**	**0.147**	**0.085**	**0.156**	**0.094**
η	**0.200**	**0.266**	**0.158**	**0.273**	**0.149**	**0.248**
$(w)_{gain}$ [%]	**33.8**	**37.6**	**17.1**	**18.0**		
$(SFC)_{gain}$ [%]	**25.2**	**6.7**	**5.5**	**8.7**		
$(\eta)_{gain}$ [%]	**33.8**	**7.2**	**5.9**	**9.7**		

4.4 Turbojet Engines Topped with Wave Rotors

Figure 68 illustrates how a four-port wave rotor is used to top a simple turbojet engine (without afterburner). Point "a" here refers to the ambient condition at the inlet diffuser. Thermodynamic analysis of such a topped cycle is different form that of a stationary topped cycle due to the presence of the inlet (diffuser) and nozzle and the fact that in a turbojet cycle the net output work is zero, whereas in a grounded gas turbine the turbine work is greater than the compressor shaft work.

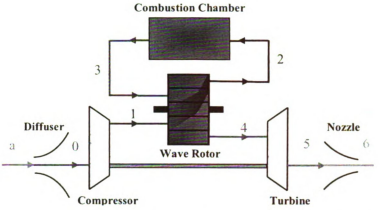

Figure 68: Schematic of a turbojet engine topped by a four-port wave rotor

Figure 69 visualizes all five wave rotor implementations in a schematic T-s diagrams. Path a-0-1_b-4_b-5_b-6_b represents the baseline cycle and path a-0-1_i-2_i-3_i-4_i-5_i-6_i (i=A, B, C, D, E) indicates the wave-rotor-topped cycles.

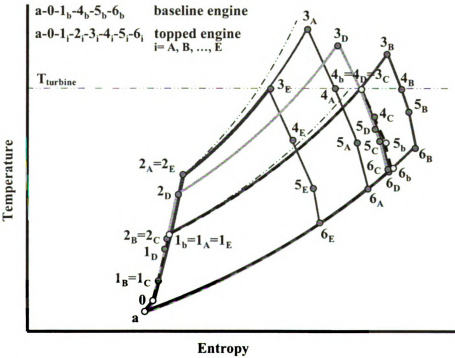

Figure 69 : Schematic T-s diagrams for a baseline turbojet cycle and five different wave-rotor-topped cycles

4.4.1 Thermodynamic Calculations

For the thermodynamic calculations, a reasonable case considered here is an aircraft equipped with a simple turbojet engine flying at an altitude of 10,000 m at Mach 0.8 . The component performance parameters of the C-30 engine are used as the baseline engine. Other component efficiencies are listed in Table 8. Now, a higher pressure drop of 5% in the combustion chamber (Π_{comb} = 0.95) is considered in the calculations. It simulates a higher pressure drop in the combustor due to a possible size reduction of the combustion chamber which is attractive for small propulsion systems. At the altitude of 10,000 m, ambient air enters the inlet diffuser at T_a=223 K and p_a=26.5 kPa .

Table 8: Turbojet baseline engine data, assuming T_0=300 K, Cp_{air}=1.005 kJ/kgK, Cp_{gas}=1.148 kJ/kgK, γ_{air}=1.4 , γ_{gas}=1.33

Baseline Engine		
Turbine inlet temperature	T_{4b}	1116.5K
Compressor pressure ratio	p_{t1b}/p_{t0}	3.6
Diffuser isentropic efficiency	η_D	93%
Compressor isentropic efficiency	η_C	80%
Compressor polytropic efficiency	η_{PC}	83%
Combustion efficiency	η_Q	98%
Combustor pressure loss	Π_{comb}	0.95
Mechanical transmission efficiency	η_M	99%
Turbine isentropic efficiency	η_T	84%
Turbine polytropic efficiency	η_{PT}	83%
Nozzle isentropic efficiency	η_N	95%

- **Path a-0: Inlet Diffuser**

With the given flight Mach number M, the stagnation temperature across the diffuser (T_{ta}=T_{t0}) is:

$$T_{t0} = T_{ta} = T_a\left(1 + \frac{\gamma_{air} - 1}{2} M^2\right) \tag{63}$$

Using the definition of the diffuser isentropic efficiency (η_D), the diffuser outlet total pressure is obtained from the equation :

$$\frac{p_{t0}}{p_a} = \left(1 + \eta_D \frac{u_a^{\,2}}{2 Cp_{air} T_a}\right)^{\gamma_{air}/\gamma_{air}-1} \tag{64}$$

- **Path 0-1: Compressor**

The approach used before is implemented for this stage.

- **Path 1-2: Compression in the Wave Rotor**

The approach used before is implemented for this stage.

- **Path 2-3: Combustion Chamber**

The approach used before is implemented for this stage.

- **Path 3-4: Expansion in the Wave Rotor**

The approach used before is implemented for this stage.

- **Path 4-5: Turbine**

In turbojet engines, considering the mechanical transmission efficiency, the compressor shaft work equals the turbine output work:

$$Cp_{air}(T_{t1} - T_{t0}) = \eta_M (1+f) Cp_{gas}(T_{t4} - T_{t5}) \tag{65}$$

Therefore, the total temperature of the gas leaving the turbine can be calculated as:

$$T_{t5} = T_{t4} - \frac{Cp_{air}(T_{t1} - T_{t0})}{\eta_M (1+f) Cp_{gas}} \tag{66}$$

To find the total pressure of the gas leaving the turbine (p_{t5}), the value of the turbine isentropic efficiency (η_T) is needed. There are two ways to calculate η_T for a turbine:

$$\eta_T = \frac{(\frac{p_{t5}}{p_{t4}})^{(\gamma_{gas}-1)\eta_{PT}/\gamma_{gas}} - 1}{(\frac{p_{t5}}{p_{t4}})^{(\gamma_{gas}-1)/\gamma_{gas}} - 1} \tag{67}$$

and,

$$\eta_T = \frac{(\frac{T_{t5}}{T_{t4}}) - 1}{(\frac{p_{t5}}{p_{t4}})^{\gamma_{gas}-1/\gamma_{gas}} - 1} \tag{68}$$

It is preferred to use the turbine polytropic efficiency η_{PT} to obtain p_{t5} . Therefore, by equating the above two equations, one finds:

$$\frac{p_{t5}}{p_{t4}} = (\frac{T_{t5}}{T_{t4}})^{\frac{\gamma_{gas}}{(\gamma_{gas}-1)\eta_{PT}}} \tag{69}$$

or,

$$\frac{p_{t5}}{p_a} = \frac{p_{t4}}{p_a}(\frac{T_{t5}}{T_{t4}})^{\frac{\gamma_{gas}}{(\gamma_{gas}-1)\eta_{PT}}} \tag{70}$$

- **Path 5-6: Nozzle**

For a given local pressure ratio at the nozzle exit (p_6/p_a), it is true that:

$$\frac{p_{t5}}{p_6} = \frac{p_{t4}}{p_a}\frac{p_{t5}}{p_{t4}}\frac{p_a}{p_6} = \frac{p_{t4}}{p_a}\frac{p_{t5}/p_a}{p_{t4}/p_a}\frac{1}{p_6/p_a} \tag{71}$$

Parameter p_{t5}/p_6 is a useful quality for calculating the local gas temperature leaving the nozzle (T_6) by using the definition of the nozzle isentropic efficiency (η_N):

$$T_6 = T_{t5} - \eta_N T_{t5}\left[1 - \left(\frac{1}{p_{t5}/p_6}\right)^{\frac{\gamma_{gas}-1}{\gamma_{gas}}}\right] \tag{72}$$

Since $T_{t5}=T_{t6}$, the nozzle exit velocity (u_6) can be calculated from the expression:

$$u_6 = \sqrt{2Cp_{gas}(T_{t5} - T_6)} \tag{73}$$

Therefore, the nozzle exit Mach number is obtained:

$$M_6 = \frac{u_6}{\sqrt{\gamma_{gas} R_{gas} T_6}} \tag{74}$$

Finally, for the given p_6/p_a , the ratio of p_{t6}/p_a is calculated from the expression:

$$\frac{p_{t6}}{p_a} = \frac{p_{t6}}{p_6}\frac{p_6}{p_a} = (1 + \frac{\gamma_{gas} - 1}{2} M_6^{\,2})^{\frac{\gamma_{gas}}{\gamma_{gas}-1}} \frac{p_6}{p_a} \tag{75}$$

After calculating the thermodynamic properties of all states in the cycle, it is possible to evaluate the engine performance parameters. For instance, the thrust produced by the engine is given by:

$$T = (\dot{m}_{air} + \dot{m}_f) u_6 - \dot{m}_{air} u_a + (p_6 - p_a) A_N \tag{76}$$

where A_N is the exhaust area of the nozzle. Thus, the specific thrust (thrust per unit mass flow of air) can be written as:

$$ST = (1+f) u_6 - u_a + (p_6 - p_a)\frac{A_N}{\dot{m}_{air}} \tag{77}$$

The pressure term in the above equation can be presented [233] as:

$$(p_6 - p_a)\frac{A_N}{\dot{m}_{air}} = a_a \left[(1+f)\frac{R_{gas}}{R_{air}} \frac{T_6/T_a}{u_6/a_a} \frac{1 - p_a/p_6}{\gamma_{air}} \right] \tag{78}$$

where a_a is the sound velocity of the entering air. Therefore, the specific thrust can be calculated as:

$$ST = (1+f) u_6 - u_a + a_a \left[(1+f)\frac{R_{gas}}{R_{air}} \frac{T_6/T_a}{u_6/a_a} \frac{1 - p_a/p_6}{\gamma_{air}} \right] \tag{79}$$

The thrust pressure term $(p_6\text{-}p_a)A_N$ is non-zero only if the exhaust jet is supersonic. In this study, all calculations have been performed for p_6/p_a =1 resulting in zero value for the thrust pressure term.

The specific fuel consumption is given by:

$$SFC = \frac{f}{ST} \tag{80}$$

Finally, the overall efficiency is derived as:

$$\eta_O = \frac{ST\,u_a}{f\,h_{PR}} \tag{81}$$

4.4.2 Predicted Performance Results

A detailed documentation of the results is not presented here. The reader is referred instead to Ref. [234]. However, numerical values of the relevant cycle data and the performance enhancement are summarized in Table 9, where indicates an attractive relative performance improvement in overall efficiency and specific thrust of about 15.4% and a 13.3% reduction in specific fuel consumption using a wave rotor pressure ratio of 1.8. Table 9 shows that for Case A perhaps the best combination of high overall efficiency, specific thrust and low specific fuel consumption is achieved. However, Case E provides the lowest value of the specific fuel consumption and the highest overall efficiency.

Table 9: Performance comparison between baseline turbojet engine and five cases of wave-rotor-topping with a wave rotor pressure ratio of 1.8

Same as baseline engine	Case **A** • compressor • turbine inlet temp.	Case **B** • overall press. ratio • turbine inlet temp.	Case **C** • combustor	Case **D** • turbine inlet pressure • turbine inlet temp.	Case **E** • compressor • combustor end temp.	**Baseline**
T_4 [K]	1116.5	1116.5	1056.2	1116.5	1042.5	1116.5
Π_C	3.60	2.00	2.00	2.65	3.60	3.60
Π_T	1.73	1.30	1.32	1.47	1.81	1.73
w_C [kJ/kg]	140	68	68	100	140	140
ST [N s/kg]	**566**	**525**	**493**	**550**	**518**	**491**
SFC [kg/kN s]	**0.0383**	**0.0446**	**0.0441**	**0.0412**	**0.0378**	**0.0442**
η_o	**0.145**	**0.125**	**0.126**	**0.135**	**0.147**	**0.126**
$(ST)_{gain}$ [%]	**15.4**	**7.1**	**0.46**	**12.1**	**5.6**	
$(SFC)_{gain}$ [%]	**13.3**	**0.1**	**-0.3**	**6.9**	**14.5**	
$(\eta_o)_{gain}$ [%]	**15.4**	**-0.9**	**0.3**	**7.4**	**17.0**	

It is interesting to note that for Case A the turbine pressure ratio is the same for both the baseline and enhanced engines (Π_T =1.73) since the compressor is unchanged. However, due to the higher turbine inlet pressure, the turbine inlet volume flow is lower, which may require an adaptation of the turbine. Also, Case D here uses only the same turbine inlet temperature and inlet pressure of the baseline engine. Note that for the case of a stationary gas turbine, the same physical turbine as the corresponding baseline engine can be used because the inlet and outlet turbine conditions remain unchanged, which is different from the turbojet cycle considered here.

Figure 70 shows a map of the relevant design space for Cases A, B, and D. Again, Cases C and E can not be shown on the same map because in both cases the turbine inlet temperature is less than indicated in the upper right corner of the map. Therefore, the performance map of Cases C and E is shown instead in Figure 71, where both cases have

the same combustion end temperature as the baseline engine, as indicated in the upper right corner of the map.

The same trend as observed for stationary gas turbines is seen here again. For higher compressor pressure ratios, the benefit of using a wave rotor diminishes. Figure 70 shows that for compressor pressure ratios greater than about 20, almost no benefit can be obtained for Cases A, B, and D. The benefit is the greatest for lower compressor pressure ratios. Implementing Cases C and E even results in performance enhancement for compressor pressure ratios just lower than about 10, as seen from Figure 71.

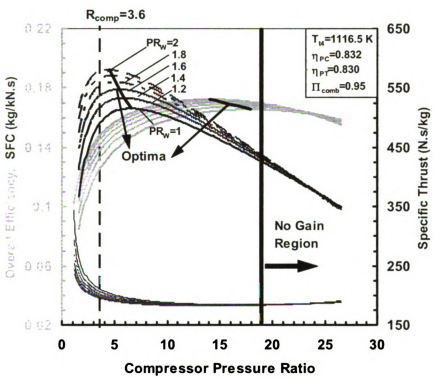

Figure 70: Performance maps for wave-rotor-topping of the C-30 turbojet engine, Cases A, B, and D

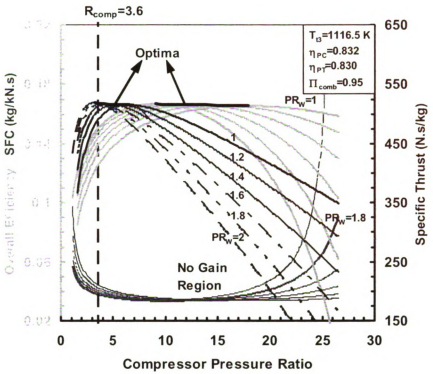

Figure 71: Performance map for wave-rotor-topping of the C-30 turbojet engine, Cases C and E

CHAPTER 5: PRELIMINARY WAVE ROTOR DESIGN

5.1 Analytical Approach

The first step in designing a wave rotor is to decide on a TF or RF wave rotor configuration. One problem with TF and RF wave rotor configurations is that fully purged processes are not often achieved due to a high turbine inlet pressure. As an example, Figure 35 shows fluid flow patterns which clearly indicate that the high pressure part (charging process) in both the TF and RF configurations does not start with channels filled uniformly with fresh air. In the case of the TF wave rotor, the channels are already filled with fresh air received from the compressor and residual burned gas from the low-pressure part of the cycle, resulting in exhaust gas recirculation back to the combustor which in turn causes excessive temperatures in the discharge ducts and parts of the end wall. In the RF configurations, the channels are filled with the fresh air and some residual air and gas from the low-pressure part of the cycle known as the buffer layer [180]. This residuum can remain permanently in the channels. Repeated compression waves increase the temperature of this buffer layer. This leads to high wall temperatures in the center of the channels [179]. It is possible to achieve a full scavenging process for both the TF and RF configurations using bypassing or bleeding of certain mass flows [9, 178, 179]. However, all of this leads to more complex configurations.

Knowing the above challenges, one-dimensional analytical gasdynamic models are used here to analyze the high-pressure phase of four-port wave rotors. Two approaches can be considered. The simplest way is to assume that the high-pressure cycle begins with channels fully filled with air at the ambient state for a Comprex or the state of the

compressor discharge in the case of a gas turbine application. This approach gives reasonable results for the Comprex analysis where the charging process begins when the channels are fully filled with fresh ambient air. This approach has been discussed in detail in our previous publications [235, 236]. A similar approach, which is a more realistic model for most gas turbine applications, calculates the channel temperature and pressure at the beginning of the high pressure part, which are mostly different from those of the compressor discharge air (as will be described in this Chapter). The overall procedure allows a fast estimate of the wave rotor dimensions which is useful for preliminary design considerations. The accuracy of this approach can be enhanced by solving the flow field in the low-pressure cycle and using the results as the initial state at the beginning of the high-pressure part. The difference with the initially obtained values is then an indicator of the accuracy and convergence of the calculations.

Even though all these approaches can be applied to the TF and RF configurations, they may be more suitable for the RF configurations where the channels are filled mostly with air at the beginning of the charging process. When applied to the TF configurations, however, the models are still consistent with the thermodynamic performance calculations. Performance calculations for the TF configurations sometimes do not account for the pre-burned gas contained in the combustor inlet flow and the flow is considered only to be air (similar to the previous chapter). If the gas recirculation is considered, higher accuracy could be obtained for the thermodynamic performance calculation and the wave rotor design.

The present work follows a methodology similar to that used by Keller [44] with several modifications. Keller does not consider tuning of the reflected shock wave as

does the current work. As a result, Keller's approach obtains only a relative small gas penetration length as shown later. Two main cases are considered: a charging process (1) with a single shock wave (2) with two shock waves. The first is simpler, but gives less favorable results. Furthermore, two different wave patterns are considered in the more complex second case. For low wave rotor compression ratios, the idea of using weak shock waves (isentropic) relations instead of existing normal shock wave equations has been implemented by Selerowicz and Piechna to simplify the gasdynamic calculations [85]. For beneficial high values of wave rotor compression ratios, however, the assumption of weak shock waves inside channels is not accurate and jump relations across the shock waves are necessary for the calculations [6, 85, 91, 93]. Gyarmathy emphasizes the importance of using jump relations across the shock waves when describing the operation of a conventional Comprex [6], but he performs no calculations. Taking into account the jump conditions, Weber et al. [91, 93] describe a design procedure for a type of Comprex which is different from the conventional Comprex as Keller has considered [44]. The procedure described here calculates wave speeds, the location of air/gas interface, and port widths in the high-pressure phase. Other useful design parameters including channel height and rotor size can be subsequently estimated. Besides the assumptions described in Chapter 3, it is assumed that pressure equalization occurs faster than mixing. Thus, the thickness of the mixing layer between the burned gas and the fresh air inside the channels is negligibly small and mixing between the gases is therefore ignored.

5.1.1 Charging Process with a Single Shock Wave

As a first step, the charging process is considered in the absence of the secondary shock wave. This situation may occur when the combustor pressure loss is relatively

small and hence the total pressure difference between the incoming hot gas and outgoing compressed air is small. For a particular level of combustor pressure drop, this may lead to equal static pressures at the high-pressure gas inlet and high-pressure air outlet, avoiding the primary shock reflection off the outlet port. The wave diagram of the charging process is shown in Figure 72 which is the same as Figure 33 with some additional information.

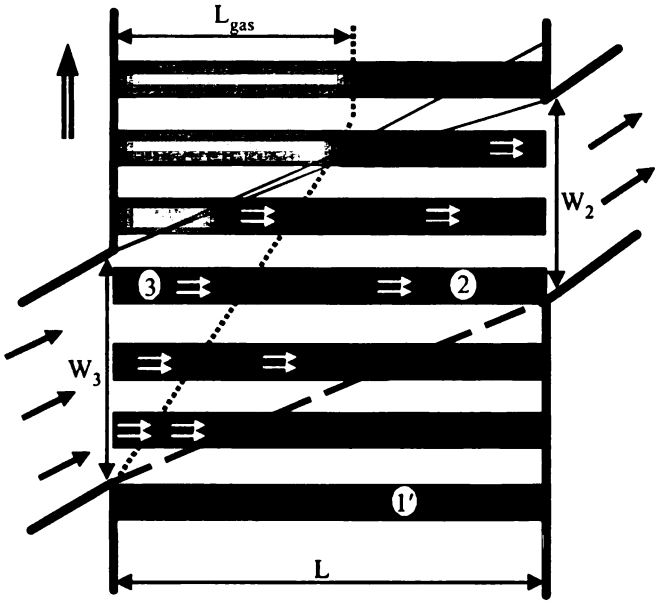

Figure 72: Wave diagram of high-pressure part with only one shock wave

As explained in Chapter 3, the burned gas coming from the combustor enters the rotor through the inlet port 3. The air, compressed by the hot gas, leaves the channels through the outlet port 2. Region 1′ represents the channel closed at both ends, containing only air. By further rotation, the hot burned gas (region 3) penetrates the channel triggering a shock wave (dashed line). The air/gas interface (dotted line) follows the shock wave with an induced velocity u_2. Behind the shock wave (region 2), the compressed air has the same local pressure and speed as the inlet exhaust gas ($p_2=p_3$ and $u_2=u_3$). As the shock

wave reaches the right end of the channel, the compressed air flows out into the combustion chamber. This is usually called the tuning condition for the primary shock wave [6, 40, 44, 79]. In the following it is referred to as the tuning condition 1 (TC 1). The tuning condition 2 (TC 2) dealing with the generation of a reflected shock wave will be introduced in the next section.

When the air/gas interface approaches a timed location, typically around the middle of the channel, the flow is stopped by closing the gas inlet port. An expansion wave originates from the upper corner of the inlet port and propagates toward the right end of the channel. In Figure 72, L_{gas} denotes the gas penetration length indicating how far the burned gas can penetrate the rotor channels. It is nearly the location where the first disturbance of the expansion wave catches the air/gas interface. W_3 and W_2 are the inlet and outlet port widths, respectively. Tuning condition 3 (TC 3) is fulfilled if the expansion wave reaches the right end of the channel at the moment when the upper edge of the outlet port closes the channel [6, 40, 44, 79].

To calculate an example of the flow properties in the channels shown in Figure 72, the inlet and outlet stagnation pressures and temperatures listed in Table 10 are used as port boundary conditions, assuming air enters the compressor at atmospheric pressure. These data are obtained from the results of the thermodynamic calculations performed in Chapter 4 for the wave rotor implementation of Case A into the C-30 engine.

Table 10: Enhanced engine data, assuming $PR_W = p_{t2}/p_{t1} = 1.8$ for Case

Port Thermodynamic States		Enhanced C-30
Inlet air pressure	p_{t1}	3.60×101 kPa
Outlet air pressure	p_{t2}	6.48×101 kPa
Inlet gas pressure	p_{t3}	6.35×101 kPa
Outlet gas pressure	p_{t4}	4.38×101 kPa
Inlet total air temperature	T_{t1}	466.6 K
Outlet total air temperature	T_{t2}	569.3 K
Inlet total gas temperature	T_{t3}	1204.7 K
Outlet gas total temperature	T_{t4}	1116.5 K

The following five equations are used to find the five unknown parameters p_3, T_3, u_2, $p_{1'}$, $T_{1'}$:

$$u_2 = \frac{\sqrt{\gamma_{air} R_{air} T_{1'}}}{\gamma_{air}} \left(\frac{p_3}{p_{1'}} - 1 \right) \sqrt{\frac{\frac{2\gamma_{air}}{\gamma_{air}+1}}{\frac{p_3}{p_{1'}} + \frac{\gamma_{air}-1}{\gamma_{air}+1}}} \tag{82}$$

$$T_{t2} = T_2 + \frac{u_2^2}{2Cp_{air}} \tag{83}$$

$$\frac{p_{t2}}{p_2} = \left(\frac{T_{t2}}{T_2} \right)^{\frac{\gamma_{air}}{\gamma_{air}-1}} \tag{84}$$

$$T_{t3} = T_3 + \frac{u_2^2}{2Cp_{gas}} \tag{85}$$

$$\frac{p_{t3}}{p_3} = \left(\frac{T_{t3}}{T_3} \right)^{\frac{\gamma_{gas}}{\gamma_{gas}-1}} \tag{86}$$

Note that $p_2 = p_3$, $u_2 = u_3$, and T_2 is obtained by using Eq. (5) derived in Chapter 3. Also, the velocity of the flow in the inlet duct is $(u_2^2 + V^2)^{1/2}$ where V stands for the tangentially averaged rotor speed. However, it has been justified [44] that the rotor speed

is small compared with the flow sound speeds, i.e. $V/a_2 << u_2/a_2$. Therefore, V has been omitted on the right sides of Eqs. (83) and (85).

For Case A described before, the above five unknowns are calculated as: p_3=6.24×101 kPa , T_3=1199.3 K , u_2=111.8 m/s , $p_{1'}$= 4.45×101 kPa , and $T_{1'}$=510.8 K.

The results can be further used to calculate the gas penetration length (nearly exactly L_{gas}). It is an important design parameter which will be used to determine the required rotor port widths. The maximum possible value of the compressed air mass flow is reached when the gas penetration length becomes equal to the rotor channel (L_{gas}/L=1). The two following equalities are used to find the dimensionless penetration length L_{gas}/L:

$$\frac{L_{gas}}{u_2} = \frac{W_3}{V} + \frac{L_{gas}}{u_2 + a_3} \tag{87}$$

$$\frac{W_3}{V} + \frac{L_{gas}}{u_2 + a_3} + \frac{L - L_{gas}}{u_2 + a_2} = \frac{L}{w_S} + \frac{W_2}{V} \tag{88}$$

Equation (87) results by equating the time required for the air/gas interface originating from the lower corner of the inlet port to be overtaken by the expansion wave (L_{gas}/u_2) with the opening time of the inlet port (W_3/V) plus the time required for the expansion wave to catch the air/gas interface (L_{gas}/u_2+a_3). Tuning conditions TC 1 and TC 3 result in Eq. (88). Note that when the expansion wave meets the air/gas interface, its velocity reduces from $u_2 + a_3$ to $u_2 + a_2$. Multiplying both sides of Eqs. (87) and (88) by $a_{1'}$ and dividing them by length L and simplifying gives:

$$\frac{L_{gas}}{L} = \frac{\dfrac{1}{M_S} - \dfrac{1}{M + \dfrac{a_2}{a_1}}}{1 - \dfrac{W_2}{W_3}\left[\dfrac{1}{M(1+M_3)} + \dfrac{1}{M + \dfrac{a_3}{a_2}\dfrac{a_2}{a_1}} - \dfrac{1}{M + \dfrac{a_2}{a_1}}\right]} \tag{89}$$

where $M = u_2/a_1$, and $M_3 = u_2/a_3$ are the flow Mach number and the Mach number of the burned gas in region 3, respectively. $M_S = w_S/a_1$, is the shock Mach number where w_S represents the shock wave velocity. The only unknown term here is the port width ratio W_2/W_3. It is obtained by writing the continuity equation across the combustion chamber which gives:

$$\dot{m}_3 = \dot{m}_2 + \dot{m}_f \tag{90}$$

or,

$$\rho_3 u_3 A_3 = \rho_2 u_2 A_2 + \dot{m}_f \tag{91}$$

Because $u_2 = u_3$ and $A_3 = W_3 \cdot z$, $A_2 = W_2 \cdot z$ where z is the height of the channel, the above equation can be simplified to:

$$\frac{\rho_3}{\rho_2}\frac{W_3}{W_2} = 1 + f \tag{92}$$

Here, it is assumed that $\dot{m}_1 = \dot{m}_{air} = \dot{m}_2$. Other cycles can exist in which the mass flow rates $\dot{m}_1$ and $\dot{m}_2$ are not the same, but they are not considered here. By using the ideal gas equation, Eq. (92) transforms to:

$$\frac{W_2}{W_3} = \frac{R_{air}}{R_{gas}}\frac{T_2}{T_3}\frac{1}{(1+f)} = \left(\frac{R_{gas}}{R_{air}}\frac{T_3}{T_2}(1+f)\right)^{-1} \tag{93}$$

Thus, substituting this equation into Eq. (89) estimates the gas penetration length. L_{gas}/L as a function of the initial cycle thermodynamics and the port boundary conditions. For Case A and corresponding thermodynamic parameters listed in Table 10, a very low value of L_{gas}/L =0.05 is obtained. Similar to Keller's results [44], the present result indicates that for typical wave rotor pressure ratios, e.g. $PR_W < 3$, the gas penetration length L_{gas}/L is very small, e.g. less than 0.2 for such tuned wave rotors. Hence a relative small amount of air compared to the wave rotor channel volume is delivered to the outlet port. Furthermore, it leads to very small and unrealistic port width W_3 and W_2 . For instance, inlet gas port width can be found by using Eq. (87) as:

$$W_3 = L_{gas}\left(\frac{1}{u_2} + \frac{1}{u_2 + a_3}\right)V \tag{94}$$

Also, Eq. (93) gives the port width ratio W_2/W_3 from which the absolute value of W_2 can be obtained, by using W_3 from Eq. (94). In this study, W_3 = 0.45 cm and W_2 = 0.21 cm are obtained for a rotor with a channel length of L = 20 cm and a rotational speed of V=50 m/s. A huge (and unrealistic) channel height of H_{cell} = 35 cm would be then necessary for the desired volume flow, resulting in an undesirably bulky wave rotor. An alternative solution should be sought to increase the gas penetration length. This is the topic of the next section.

5.1.2 Charging Process with Two Shock Waves

Several wave diagrams can be introduced that employ two shock waves. Two of these wave patterns were introduced in Chapter 3 and they are studied in more detail in this section. As it will be shown in the following, considering a secondary wave inside the channels results in reasonable geometry parameters with a greater relative gas penetration length.

- **Charging Process with Two Primary Shock Waves**

Figure 73 depicts a wave diagram which employs two shock waves. It is similar to the previous wave diagram sketched in Figure 72, but both inlet and outlet port widths have been proportionally extended and a shorter rotor height is used, matching the same mass flow rate through the rotor as considered before. Also, the gas inlet port becomes much greater than the air outlet port keeping the same port width ratio as before to allow more gas to penetrate the rotor channels.

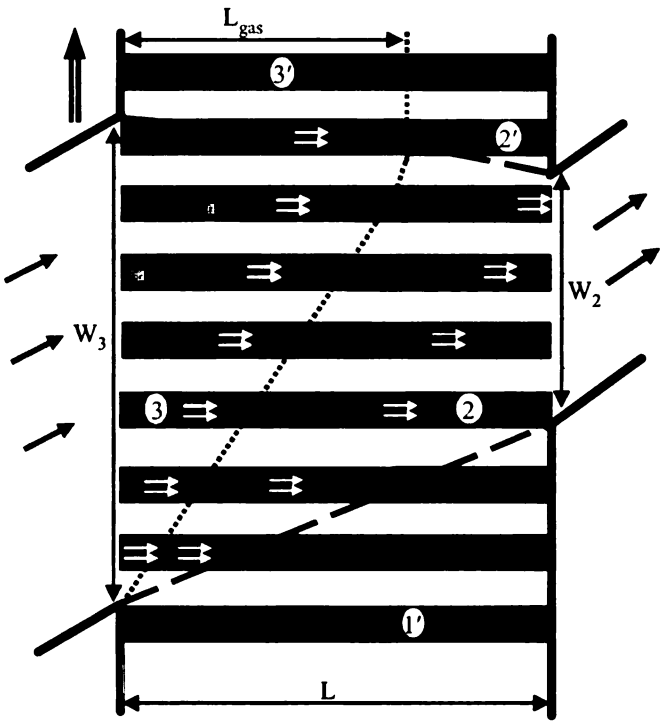

Figure 73: Wave diagram of high-pressure part with two primary shock waves

By closing the outlet port, a second primary shock wave originates at the upper outlet edge and propagates from the right to the left with velocity $w_{S\text{-}air}$ into the part of the channel that contains air flowing with velocity u_2 from left to right. It reduces the velocity of the air to zero to satisfy the zero-slip boundary condition at the end wall. After

crossing the air/gas interface, the velocity of the second primary shock wave increases from $w_{S\text{-}air}$ to $w_{S\text{-}gas}$, where the latter is the velocity of the shock wave in gas region 3. The increase in the velocity is mainly due to the fact that the burned gas has a higher temperature than the compressed air. The double-compressed air region and the compressed gas region after the second primary shock wave are introduced as regions 2′ and 3′, respectively. Here, a favorite case is considered where the closure of the gas inlet port is timed with the arrival of the second primary shock wave. This is called the tuning condition 2 (TC 2) [6, 40, 79]. Hence, expansion waves are not generated after closing the gas inlet port.

To find the useful design parameters for such a wave diagram, all previous derived equations are used again, but new expressions must be derived for W_3, W_2, and L_{gas}/L. Hence, the two following equalities are used to find the new value of dimensionless penetration length L_{gas}/L:

$$\frac{L_{gas}}{u_2} = \frac{L}{w_S} + \frac{W_2}{V} + \frac{L - L_{gas}}{w_{S-air}} \tag{95}$$

$$\frac{W_3}{V} = \frac{L_{gas}}{u_2} + \frac{L_{gas}}{w_{S-gas}} \tag{96}$$

The first equation is found by equating the time required for the air/gas interface originating from the lower corner of the inlet port to reach the second primary shock wave (L_{gas}/u_2) with the time required for the first primary shock wave to run through the channel (L/w_S) plus the outlet port opening time (W_2/V) plus the time required for the second primary shock wave to meet the air/gas interface ($(L\text{-}L_{gas})/w_{S\text{-}air}$). The second equation is obtained by equating the inlet port opening time (W_3/V) with the time required for the air/gas interface originating from the lower corner of the inlet port to

reach the second primary shock wave (L_{gas}/u_2) plus the time required for the second primary shock wave to travel through the gas region and to meet the upper corner of the inlet port ($L_{gas}/w_{S\text{-}gas}$). Multiplying both sides of Eqs. (95) and (96) by $a_{1'}$ and dividing them by length L and simplifying gives:

$$\frac{L_{gas}}{L} = \frac{\dfrac{1}{M_S} + \dfrac{a_{1'}}{w_{S-air}}}{\dfrac{1}{M} + \dfrac{a_{1'}}{w_{S-air}} - \dfrac{W_2}{W_3}\left(\dfrac{1}{M} + \dfrac{a_{1'}}{w_{S-gas}}\right)} \tag{97}$$

In this expression, $w_{S\text{-}air}$ and $w_{S\text{-}gas}$ are unknown and must be found. To find $w_{S\text{-}air}$, the strength of the second primary shock wave propagating in the air region 2 ($\Pi_{S\text{-}air} = p_{2'}/p_2$) is first obtained by using Eq. (7):

$$u_2 = \frac{a_{2'}}{\gamma_{air}}\left(\Pi_{S-air} - 1\right)\sqrt{\frac{\dfrac{2\gamma_{air}}{\gamma+1}}{\Pi_{S-air} + \dfrac{\gamma_{air}-1}{\gamma_{air}+1}}} \tag{98}$$

Then $w_{S\text{-}air}$ is found by using Eq. (9):

$$w_{S-air} = a_{2'}\sqrt{\frac{\gamma_{air}+1}{2\gamma_{air}}\left(\Pi_{S-air} - 1\right) + 1} \tag{99}$$

Finally, the corresponding Mach number can be calculated by using Eq. (11):

$$M_{S-air} = \sqrt{\frac{\gamma_{air}+1}{2\gamma_{air}}\left(\Pi_{S-air} - 1\right) + 1} \tag{100}$$

A similar approach is used to find $\Pi_{S\text{-}gas} = p_{3'}/p_3$ (strength of the second primary shock wave propagating in the gas region 3), $w_{S\text{-}gas}$, and $M_{S\text{-}gas}$ using the gas properties. Therefore, Eq. (97) calculates the dimensionless penetration length for the wave diagram shown in Figure 73. For the case considered in this study $L_{gas}/L = 0.66$ is calculated which

is a considerably greater value than that calculated for the wave diagram with the single shock shown in Figure 72. The higher value of this parameter is due to the extension of the gas inlet port width, allowing more burned gas to enter the rotor channels. By obtaining L_{gas}/L it is now possible to estimate the rotor geometry, as described before.

By obtaining W_2 and W_3 using Eqs. (95) and (96), respectively, the inlet opening time (t_3) and outlet opening time (t_2) become:

$$t_3 = \frac{W_3}{V} \tag{101}$$

and,

$$t_2 = \frac{W_2}{V} \tag{102}$$

Additionally, the time required for the primary shock wave to run through the channel (t_1) is simply equal to L/w_S.

To find the other geometry characteristics, the following procedure is described. For a given baseline air volume flow rate, Q_2, the cross-sections of the outlet port 2 and inlet port 3 can be obtained from:

$$A_2 = \frac{Q_2}{u_2} \tag{103}$$

and,

$$A_3 = \frac{Q_3}{u_3} = \frac{Q_3}{u_2} \tag{104}$$

where Q_3 is the volume flow rate of the burned gas, which is different from the air volume flow rate Q_2. Considering the mass added from the fuel, the continuity equation relates Q_2 and Q_3 as follows:

$$Q_3 = \frac{\rho_2}{\rho_3} Q_2 (1 + f) \tag{105}$$

The cross-section of the outlet port A_2 is typically 10% of the frontal area of the rotor [6]. Therefore, the diameter of the rotor represented by D_{rotor} can be found from:

$$A_2 \cong \frac{10}{100} \left(\pi \frac{D_{rotor}^{\ 2}}{4} \right) \tag{106}$$

Assuming a rectangular cross-sectional channel, the channel height is given by:

$$H_{cell} = \frac{A_2}{W_2} \tag{107}$$

which is identical to $H_{cell} = A_3/W_3$ due to the continuity equation used in the derivations above.

The rotational speed of the rotor (n_{rotor}), which is a variable to be chosen by the designer, is related to the rotor angular speed (ω) by:

$$n_{rotor} = \frac{\omega}{2\pi} \tag{108}$$

where $\omega = V/D_{rotor}/2$. Finally, the channel width can be found from the expression:

$$W_{cell} = \frac{\pi D_{rotor}}{N} \tag{109}$$

where N is the number of channels for a one-row rotor, e.g., in the order of 30.

Implementing the procedure explained in this study for Case A, the discussed channel and port parameters were calculated and are listed in Table 11 and Table 12. Results clearly show that the scenario employing two primary shock waves provides realistic results. Figure 74 shows the location and size of inlet and outlet ports of the charging process based on the results obtained in the present study.

Table 11: Flow properties inside rotor channels for L=20 cm

Flow properties	Two shocks
Channel pressure in region 1′ ($p_{1'}$)	4.45×101 kPa
Channel temperature in region 1′ ($T_{1'}$)	511 K
Inlet and outlet flow velocity ($u_3 = u_2$)	112 m/s
Outlet air Mach number (M_2)	0.24
Inlet gas Mach number (M_3)	0.17
Static pressure ratio across the primary shock (Π_S)	1.40
Velocity of the first primary shock (w_S)	525 m/s
Mach number of the first primary shock (M_S)	1.16
Static pressure ratio across the second primary shock in the air region ($\Pi_{S\text{-}air}$)	1.38
Static pressure ratio across the second primary shock in the gas region ($\Pi_{S\text{-}gas}$)	1.24
Velocity of the second primary shock in the air region ($w_{S\text{-}air}$)	436 m/s
Velocity of the second primary shock in the gas region ($w_{S\text{-}gas}$)	630 m/s
Mach number of the second primary shock in the air region ($M_{S\text{-}air}$)	1.15
Mach number of the second primary shock in the gas region ($M_{S\text{-}gas}$)	1.10
Penetration length (L_{gas})	13 cm

Table 12: Wave rotor design parameters for L=20 cm, N=30, n_{rotor}=10000 rpm, and $\dot{m}_2$=0.318 kg/s,

Geometry and port characteristics	Two shock
Rotor tangential speed (V)	50 m/s
Rotor diameter (D_{rotor})	9.63 cm
Cell width (W_{cell})	1.01 cm
Cell height (H_{cell})	2.23 cm
Circumferential length from 0 to opening of air outlet port (W_1)	1.92 cm
Width of high pressure air outlet port (W_2)	3.26 cm
Width of high pressure gas inlet port (W_3)	7.02 cm
Port width ratio (W_2/W_3)	0.46
Angle from 0° until opening high pressure air outlet (α_1)	22.85 °
Opening angle of high pressure air outlet (α_2)	38.76 °
Opening angle of high pressure gas inlet (α_3)	83.52 °
Time from 0 until opening of high pressure air outlet (t_1)	0.38 ms
Outlet air opening time (t_2)	0.65 ms
Inlet gas opening time (t_3)	1.39 ms

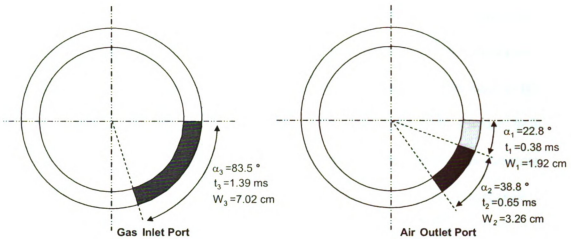

Figure 74: Preliminary port designs of the charging process, corresponding to the wave diagram sketched in Figure 73

- **Charging Process with Two Shock Waves and an Expansion Wave**

Figure 75 shows a second different wave diagram that also utilizes a secondary shock wave, but now as a reflected shock wave. Compared with the wave diagram shown in Figure 72, this wave diagram has a shorter (more compact) wave rotor design as seen in the figure and a relatively great gas penetration length. Creating such a reflected shock wave always implies that the static pressure in the high-pressure air outlet port is greater than that of the high-pressure gas inlet port. This can easily be the case when using a combustion chamber with a higher pressure loss as discussed further below in Figure 77. Here, for the same combustor pressure loss as considered before, employing a reflected shock wave results in a shorter wave rotor and a reduced velocity of the leaving high-pressure air. Because of mass continuity, the high-pressure air outlet port is now wider.

Figure 75 shows that with a reflected shock wave and a shorter rotor, the expansion wave arrives after the upper outlet edge, if the tuning condition for the shock wave at lower outlet edge (TC 1) is kept and the inlet width remains unchanged. This also has been mathematically proved by Keller [44]. In this figure W_2 is still the outlet port width

before shortening the rotor (in the absence of a reflected shock wave as discussed before). Here, W_{out} is defined as the outlet port width and W_T is introduced as the outlet port width at which the tuning condition for the expansion wave at the upper outlet edge is fulfilled (TC 3). Thus, the actual outlet port width W_{out} for the shortened rotor is wider. In fact, it is in the domain of $W_2 \leq W_{out} \leq W_T$. For a perfectly tuned design, W_{out} should equal W_T, however it is highly possible that for a given PR_W, TC 3 might not be achieved. Then, another shock wave would originate from the upper corner of the outlet port in order to satisfy the zero-slip boundary condition at the end wall. This is undesirable and not shown in Figure 75, although it describes a general case where TC 3 is not fulfilled. For such an untuned situation, the restriction $W_2 \leq W_{out} \leq W_T$ must still be satisfied.

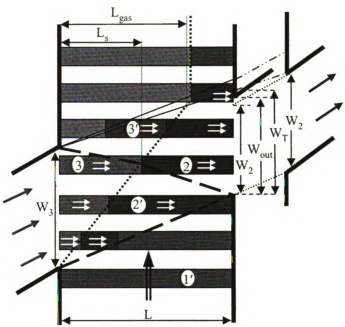

Figure 75: Outlet port width comparison before and after rotor shortening

In the shown case, to reduce the outlet velocity, the reflected shock wave originates at the lower outlet edge and propagates from the right to the left. The double-compressed air

after the reflected shock wave leaving the wave rotor toward the combustion chamber is region 2. In Figure 75, L_s represents the location where the reflected shock wave intersects the air/gas interface. The compressed gas region after the reflected shock wave is named region 3′. The reflected shock wave reduces the speed of the flow leaving the channel from $u_{2'}$ to u_2 and causes a further local pressure rise within the channel from $p_{2'}$ to p_2. By fulfilling TC 2, the entire fluid column in the channel consisting of two different fluids moves to the right with the pressure and velocity of the outlet air. In this way, the entire fluid column is compressed by the reflected shock allowing more gas to enter the channel.

Similar to the same approach described for the charging process without a secondary shock wave, again Eqs. (82)-(86) are used but with some modifications:

$$u_{2'} = \frac{\sqrt{\gamma_{air} R_{air} T_{1'}}}{\gamma_{air}} \left(\frac{p_3}{p_{1'}} - 1 \right) \sqrt{\frac{\frac{2\gamma_{air}}{\gamma_{air}+1}}{\frac{p_3}{p_{1'}} + \frac{\gamma_{air}-1}{\gamma_{air}+1}}} \tag{110}$$

$$T_{t2} = T_2 + \frac{\left(u_{2'} - u_{R-air}\right)^2}{2Cp_{air}} \tag{111}$$

$$\frac{p_{t2}}{p_2} = \left(\frac{T_{t2}}{T_2} \right)^{\frac{\gamma_{air}}{\gamma_{air}-1}} \tag{112}$$

$$T_{t3} = T_3 + \frac{u_{2'}^{\ 2}}{2Cp_{gas}} \tag{113}$$

$$\frac{p_{t3}}{p_3} = \left(\frac{T_{t3}}{T_3} \right)^{\frac{\gamma_{gas}}{\gamma_{gas}-1}} \tag{114}$$

where T_2 is now equal to:

$$T_2 = T_{1'} \frac{T_{2'}}{T_{1'}} \frac{T_2}{T_{2'}} \tag{115}$$

$T_{2'}/\ T_{1'}$ and $T_2\ /T_{2'}$ and functions of the local pressure ratio across the primary ($\Pi_S = p_3/p_{1'}$) and reflected ($\Pi_{R\text{-}air} = p_2/p_3$) shock waves, respectively, and can be obtained by using Eq. (5). Furthermore, $u_{R\text{-}air}$ is the induced velocity caused by the reflected shock wave and can be calculated from Eq. (7) using $\Pi_{R\text{-}air}$. Thus, 6 unknown parameters p_3, T_3 , $u_{2'}$, $p_{1'}$, $T_{1'}$, and $\Pi_{R\text{-}air}$ exist for the above five Eqs. (110)-(114). This shows that introducing the reflected shock gives an additional degree of freedom. This allows selecting arbitrary values of Π_S and $\Pi_{R\text{-}air}$ in a confined range. Thus, several solutions can be obtained for given engine data. However, if it is assumed that $p_{1'} = p_1$ and $T_{1'} = T_1$ the number of unknowns is reduced and unique solutions can be obtained for 4 unknown variables p_3, T_3, $u_{2'}$, and $\Pi_{R\text{-}air}$. This has been shown in a simple five-step procedure for a triple tuned wave rotor examined in our previous work [235, 236]. For example, Figure 76 shows the variation of Π_S and $\Pi_{R\text{-}air}$ versus PR_W for a given Π_{comb}. It is clearly seen that, for the given Π_{comb}, higher PR_W values can be only achieved by simultaneously increasing Π_S and decreasing $\Pi_{R\text{-}air}$. By assuming $p_{1'} = p_1$ and $T_{1'} = T_1$, the results also show that for a PR_W greater than around 1.8, $\Pi_{R\text{-}air}$ becomes less than unity which is physically impossible for a shock wave. However, a higher pressure drop allows for a higher $\Pi_{R\text{-}air}$ as it is shown in Figure 77 described below.

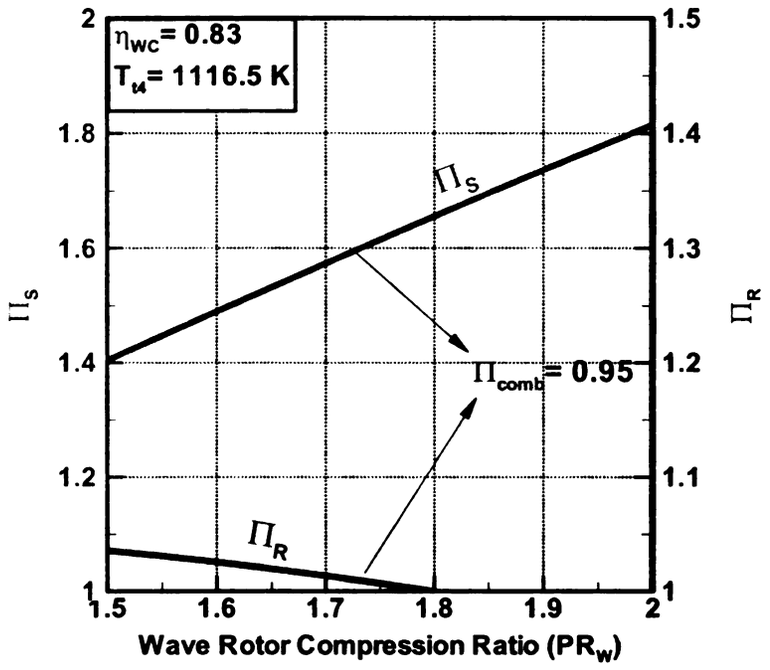

Figure 76: Variation of Π_S and Π_R versus PR_W for a constant value of Π_{comb}

Assuming $p_{1'} = p_1$ and $T_{1'} = T_1$, Figure 77 provides a general map relating the shock strengths Π_S and $\Pi_{R\text{-}air}$ to various combinations of PR_W and Π_{comb}. The right boundary of the map is the $\Pi_{R\text{-}air} = 1$ line, where the reflected shock wave vanishes. The lower and left boundary is the $u_2 = 0$ line, simulating the closed wall condition where no flow leaves the channel anymore. This condition occurs when $\Pi_{R\text{-}air}$ approaches the value of Π_S. Beside zero exit velocity line, several lines of finite exit velocity are shown between the left and right boundaries. They show that for a given PR_W, increasing $\Pi_{R\text{-}air}$ causes a reduction in u_2 due to the induction of mass motion behind the reflected shock wave.

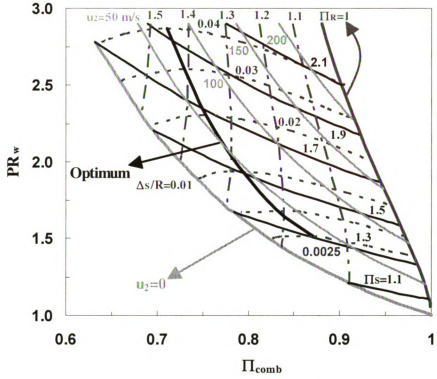

Figure 77: Shock strengths Π_S , Π_R , entropy production $\Delta s/R$, and exit velocity u_2 versus PR_W and Π_{comb}

The most interesting feature in the map may be the lines of constant entropy production in the channels due to the shock waves. The entropy production Δs is calculated by summing the entropy generations across the primary and reflected shock waves. They have been normalized by gas constants of the air and gas, respectively. For a desired fixed PR_W , coming from the $\Pi_{R\text{-}air} = 1$ line with only a primary shock, $\Delta s/R$ reduces as the reflected shock $\Pi_{R\text{-}air}$ becomes stronger. This shows the potential for higher efficiency, if the wave rotor is designed with a reflected shock wave. However, this continues only until the optimum line (solid black) is reached. The optimum line indicates the combinations of PR_W and Π_{comb} at which the least entropy production occurs in the shock wave compression for a given PR_W. Left of it, the entropy production

increases again for a given PR_W. Simultaneously in Figure 77 from the right to the left, Π_{comb} decreases. This allows for a combustor with a higher pressure drop that may be smaller and more compact, which may be especially desirable for aerospace applications. In fact, Figure 77 shows that for the desired $PR_W = 1.8$, the value of $\Pi_{comb} = 0.98$ considered in the thermodynamic analysis gives a value of $\Pi_{R\text{-}air} < 1$. Thus, a higher pressure drop ($\Pi_{comb} < 0.98$) should be selected for higher values of $\Pi_{R\text{-}air}$, which may preferably reduce the size of combustion chamber. Finally, the optimum line can be achieved at lower exit velocities, here lower than 100 m/s.

After calculating the above unknowns, it is now possible to obtain an equation for the ratio of the outlet port to the inlet port width (W_{out}/W_3) using the continuity equation at the inlet and outlet ports:

$$\frac{\rho_3 u_{2'} W_3}{\rho_2 u_2 W_{out}} = 1 + f \tag{116}$$

To find the gas penetration length for the charging process with the reflected shock wave, the following equation is introduced by equating the time required for the air/gas interface to be overtaken by the expansion wave with the opening time of the inlet port plus the time required for the expansion wave to catch the air/gas interface:

$$\frac{W_3}{V} + \frac{L_{gas}}{u_2 + a_{3'}} = \frac{L_s}{u_{2'}} + \frac{L_{gas} - L_s}{u_2} \tag{117}$$

where $a_{3'}$ is the speed of sound in the hot gas region 3′ after the reflected shock wave has passed through it and L_s is the location where the air/gas interface meets the reflected shock wave. The temperature in the region 3′ is found by using Eq. (5). The local pressure ratio across the reflected shock wave propagating in region 3 ($\Pi_{R\text{-}gas} = p_{3'}/p_3$) is calculated

similar to the method described for the charging process with the secondary shock wave. The value of L_s can be found by equating the time required for the air/gas interface originating from the lower corner of the inlet port to reach the reflected shock wave ($L_s/u_{2'}$) with the time required for the primary shock wave to run through the channel (L/w_S) plus the time for the reflected shock wave to meet the air/gas interface ($(L-L_s)/w_{R\text{-}air}$):

$$\frac{L_s}{u_{2'}} = \frac{L}{w_S} + \frac{L - L_s}{w_{R-air}} \tag{118}$$

Therefore, L_s/L can be obtained through this equation as:

$$\frac{L_s}{L} = \frac{\frac{1}{M_S} + \frac{1}{w_{R-air}/a_{1'}}}{\frac{1}{M} + \frac{1}{w_{R-air}/a_{1'}}} \tag{119}$$

Multiplying both sides of Eq. (117) with $a_{1'}$ and dividing it by the length L leads to:

$$\frac{L_{gas}}{L} = \frac{\frac{L_s}{L}\left(\frac{1}{M} - \frac{1}{u_2/a_{1'}}\right) - \frac{W_3}{M_R L}}{\frac{1}{(u_2 + a_{3'})/a_{1'}} - \frac{1}{u_2/a_{1'}}} \tag{120}$$

where M_R is the rotor Mach number defied as $M_R = V/a_{1'}$. The value of $W_3/M_R/L$ can be obtained from TC 2:

$$\frac{W_3}{M_R} = \frac{L}{M_S} + \frac{L - L_s}{w_{R-air}/a_{1'}} + \frac{L_s}{w_{R-gas}/a_{1'}} \tag{121}$$

which leads to:

$$\frac{W_3}{M_R L} = \frac{1}{M_S} + \frac{1}{w_{R-air}/a_{1'}} + \left(\frac{1}{w_{R-gas}/a_{1'}} - \frac{1}{w_{R-air}/a_{1'}}\right)\frac{L_s}{L} \tag{122}$$

Therefore, L_{gas}/L can be obtained based on Eq. (120) for a given PR_W and Π_{comb}. Figure 78 shows the variation of L_{gas}/L versus PR_W for different values of Π_{comb}. It clearly shows that the newly obtained value of L_{gas}/L is much greater than that calculated before. Therefore, employing a shock wave increases the gas penetration length significantly.

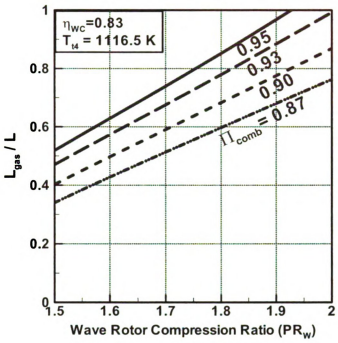

Figure 78: Variation of L_{gas}/L versus PR_W and Π_{comb}

Finally, the maximum outlet port width W_T for which TC 3 is satisfied can be obtained by equating the time required for the primary shock wave to run through the channel (L/w_S) plus the opening time of the outlet port (W_T/V) with the opening time of the inlet port (W_3/V) and the time required for the expansion wave to reach to the end of the channel:

$$\frac{L}{w_S}+\frac{W_T}{V}=\frac{W_3}{V}+\frac{L_{gas}}{u_2+a_T}+\frac{L-L_{gas}}{u_2+a_2} \tag{123}$$

By multiplying both sides of this equation by $a_{1'}$ and dividing it by length L and simplifying:

$$\frac{W_T}{W_3} = 1 - \frac{\frac{1}{M_S} + \frac{L_{gas}}{L}\left(\frac{1}{(u_2+a_2)/a_{1'}} - \frac{1}{(u_2+a_{3'})/a_{1'}}\right) - \frac{1}{(u_2+a_2)/a_{1'}}}{W_3/M_R L} \qquad (124)$$

As mentioned above, for any given PR_W, $W_T - W_{out} \geq 0$ should be a restriction. However, a designer may prefer to obtain a value of $W_T - W_{out}$ as small as possible to fulfill TC 3. Figure 79 shows the variation of dimensionless values of $(W_T - W_{out})/W_T$ versus PR_W for various values of Π_{comb}.

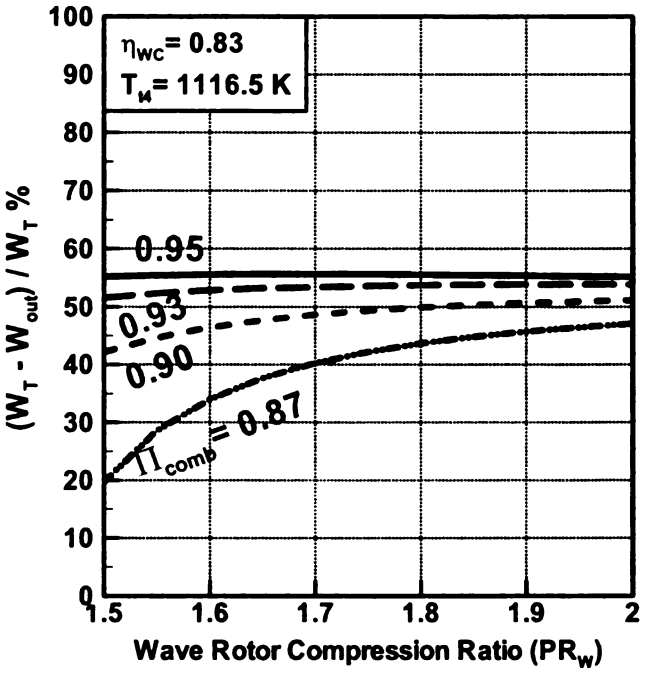

Figure 79: Variation of dimensionless values of $(W_T - W_{out})/W_T$ versus PR_W and Π_{comb}

The plot shows that the expansion wave reaches the right channel end at different times for different combinations of PR_W and Π_{comb}. Thus, for a desired fixed PR_W there is only a unique Π_{comb} that satisfies TC3 and vise versa. Furthermore, with increasing

PR_W the divergence from TC 3 increases, which is not preferred for an efficient design. In a practical design, the rotor may incorporate various cavities (pockets) in the end plates to reduce the sensitivity to a mismatch of the various wave arrival times [44]. These mismatches can be caused by other events such as variation in the engine load.

5.1.3 Validation

To validate the accuracy of the analytical prediction model described above, comparisons with numerical results of a test case have been made. Very little experimental data are published in the literature concerning successful operation of wave rotors. Therefore, it was decided to validate the above analytical model with existing numerical predictions which have been validated with some previous wave rotor investigations.

The data of the wave rotor numerically designed at University of Tokyo are selected [215]. Table 13 shows the pressure and temperature of the inlet and outlet ports of this wave rotor as they were imported into a computer code written in MathCAD software according to the above analytical approach. Additional design parameters of the Tokyo. wave rotor are shown in Figure 80 in which HP stands for high pressure and LP is used for low pressure.

Table 13: Inlet and outlet port data of University of Tokyo wave rotor, taken from Ref. [215]

Inlet air pressure	p_{t1}	3.0×101 kPa
Outlet air pressure	p_{t2}	10.1×101 kPa
Inlet gas pressure	p_{t3}	9.2×101 kPa
Outlet gas pressure	p_{t4}	3.7×101 kPa
Inlet total air temperature	T_{t1}	440 K
Outlet total air temperature	T_{t2}	907 K
Inlet total gas temperature	T_{t3}	12048 K
Outlet gas total temperature	T_{t4}	973 K

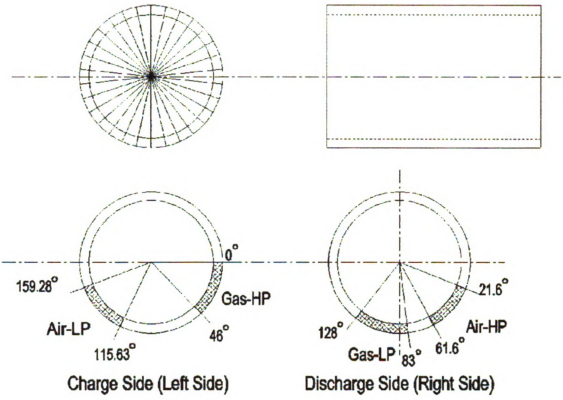

Cell Number	30
Cell Length	0.069 [m]
Cell Width	0.004 [m]
Cell Height	0.003 [m]
Mean Rotor Radius	0.02325 [m]
Rotational Speed	32151 [rpm]

Figure 80: University of Tokyo wave rotor, taken from Ref. [215]

Using some of the data provided in Table 13 (cell number, cell length, mean rotor radius, and rotational speed) and port locations shown in Figure 80, the analytical model predicts reasonable wave rotor geometry parameters as listed in Table 14 in comparison with the published data of the Tokyo wave rotor The listed data of the model are obtained for initial channel pressure and temperature of $p_{1'} = 4.34 \times 101$ kPa and $T_{1'} = 707$ K. Good agreement between the predicted results and those obtained by numerical

simulations is observed. The existing errors can be related to the assumptions made in the model, e.g., assuming pure air at the beginning of the high-pressure part of the cycle and using a constant specific heat at different states of air and gas. In the first step, the accuracy of the present model can be improved by solving the flow field in the low-pressure cycle to determine how much the temperature and pressure of the air filling the entire channel at the beginning of the high-pressure part model should be changed.

Table 14: Comparison between the analytical model and the numerical data of the Tokyo wave rotor

Geometry and port characteristics	Model	Tokyo WR
Cell width (W_{cell})	0.49 cm	0.4 cm
Cell height (H_{cell})	0.3 cm	0.3 cm
Circumferential length from 0 to opening of air outlet port (W_1)	0.76 cm	0.88 cm
Width of high pressure air outlet port (W_{out})	1.65 cm	1.62 cm
Width of high pressure gas inlet port (W_3)	2.1 cm	1.87
Port width ratio (W_{out}/W_3)	0.78	0.87
Angle from 0° until opening high pressure air outlet (α_1)	18.7 °	21.6 °
Opening angle of high pressure air outlet (α_2)	40.6 °	40.0 °
Opening angle of high pressure gas inlet (α_3)	51.7 °	46.0 °

5.2 Numerical Simulation

Even though the above analytical procedure can provide some useful design parameters for a preliminary design, for a complete design, a whole-cycle analysis including the low-pressure part of wave rotor operation is required. In analytical approaches, the method of characteristics is often used to solve the flow field especially in the scavenging part of the cycle [98-105]. An alternative technique is to use CFD methods, allowing more accurate simulation of the flow field. It has been common practice to create and use specialized codes. As reviewed in Chapter 2, several precise numerical codes have been developed so far. However, most of these codes are not commercially available, hence a few groups of researchers who have developed these in-

house codes are using them, e.g., the NASA wave rotor code. A broader accessibility of appropriate CFD tools could facilitate a wide range of wave rotor analysis. The development of modern multi-purpose commercial software packages has reached a level that allows the successful modeling and analysis of the operation of many technical devices, including wave rotors. Several commercial codes are now available that can be applied to investigate many problems related to wave rotor design and operation. Such codes are particularly interesting for 2D and 3D modeling of full devices and some special problems. They offer tools that allow for relatively easy geometric preparation, a range of typical boundary conditions, relatively fast and robust solving, and a wide range of post-processing which is valuable for engineers and scientists. Yet, the use of such codes is not as fast as the use of common office software. Although the geometry and boundary conditions can be modeled relatively fast, using such complex commercial software packages, the computational effort is still enormous, so that flow field is often only available after lengthy, time-consuming computations. Therefore, such simulations are not suitable for an initial geometry search or a geometry optimization but can be performed as a last stage of investigation, verifying solutions of particular problems or the full operation of a complete wave rotor. For preliminary investigations, initial design, and optimization they are not necessarily as efficient as specialized codes.

Some attempts at simulating pressure wave superchargers with the help of commercial codes already have been undertaken. One such code is GT-POWER, in which pipe elements have been divided into a series of objects for which the conservation equations have been solved. An interesting description of techniques for optimization of

timing, shaping, and control of pressure wave changers using GT-POWER has been described by Podhorelsky et al. [237].

The present work shows an attempt at developing 2D models of wave rotors using the commonly available CFD software FLUENT. This enables the realization of detailed gasdynamic phenomena inside the rotor channels. For most of the results investigated here, very little experimental data exist for possible verification. Therefore, the results are compared with some previous numerical data which are available for conventional wave rotors. The presented results shall not be interpreted as a proposition of a particular geometry for practical applications. While they can be a base for further investigations, they rather present some illustrations of physical phenomena generated in different configurations and phases of operation and showing the capability of the code.

5.2.1 Approach

The numerically designed Tokyo wave rotor (see Table 13 and Figure 80) was selected as a model and reference for the numerical simulation presented here. The main reason for selection of this wave rotor is the availability of detailed geometry data and operating conditions. Figure 81 shows the temperature contour in this wave rotor predicted at the University of Tokyo. While for this port arrangement the pressure contour is not reported, it is available for another operating condition as shown in Figure 82. The goal here is to produce similar results using the commercial software FLUENT. The numerical procedure described here can be performed for almost all other wave rotor configurations.

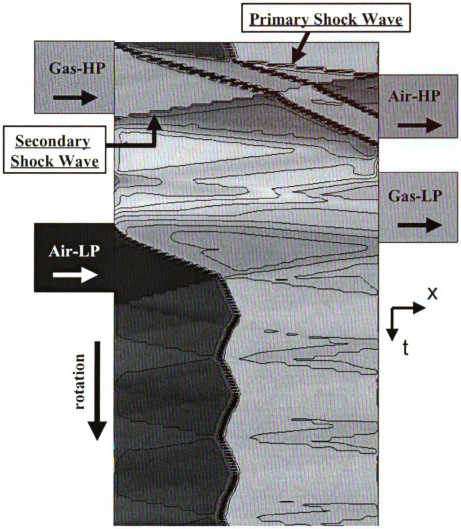

Figure 81: Non-dimensional total temperature contour of the Tokyo wave rotor, taken from Ref. [215]

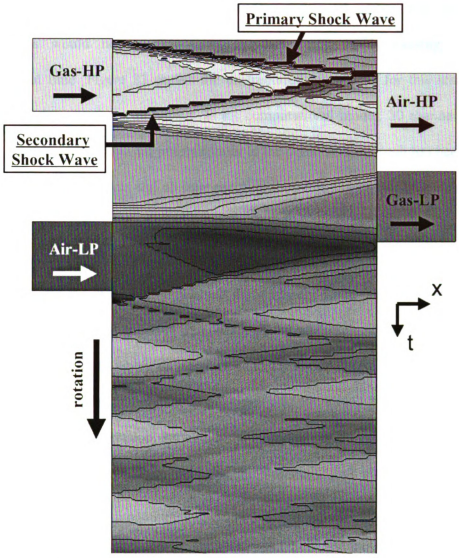

Figure 82: Non-dimensional total pressure contour of the Tokyo wave rotor, taken from Ref. [215]

The first step in the flow simulation with FLUENT is the mesh generation for a particular geometry. GAMBIT is the default grid generator for FLUENT. Even though GAMBIT has the ability to draw the geometry, a more advanced drawing software like AutoCAD was used to sketch the geometry. Using AutoCAD significantly reduces the sketching work. After creating the geometry in AutoCAD, the geometry was imported into GAMBIT for the grid generation. The mesh size in the channels and inlet and outlet

ports was carefully selected to provide accurate and fast solutions. Tests showed that finer meshes would not provide more accurate results, only causing additional computational time. Figure 83 shows the unstructured mesh used for this study at the beginning of the wave rotor operation. In the computational model, 30 channels (not all shown) move in a block upward perpendicular to the ports. A finer mesh has been used in the interface of the channels and all four ports, as shown in Figure 84. This enhances the simulation of gradual port opening and closing.

The most challenging step in generating the mesh is the creation of a stationary interface between the moving channels and the stationary ports. This was carried out by creating a relatively small gap (0.1 mm) between the wall ends of the channels and the end plates with the ports where an interface connects them. The yellowish line in Figure 85 indicates the interface where the entire right side connected grid lines slip along it during the wave rotor operation. An additional advantage of generating such a gap is the actual simulation of the leakage between the stationary end plates and the rotating channels.

Once the grid was generated in GAMBIT, the rotor geometry was imported into FLUENT. Boundary conditions, the solving method, the working fluids, the convergence criterion, and several other functions (parameters) must be defined prior to the simulation. Air as an ideal gas was chosen as the working fluid. Such an assumption reduces the accuracy of the results because the effects of gas at the inlet and outlet ports and the burned gas in the rotor channels are neglected. However, the trends of the gasdynamic processes occurring in the channels are consistent with more accurate models as shown later.

Figure 83: Generated mesh

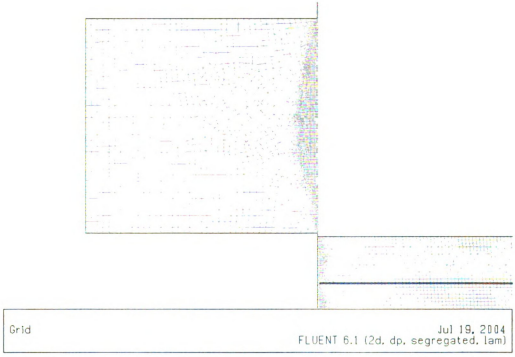

Figure 84: Finer mesh at port interface and channels, inlet high-pressure port

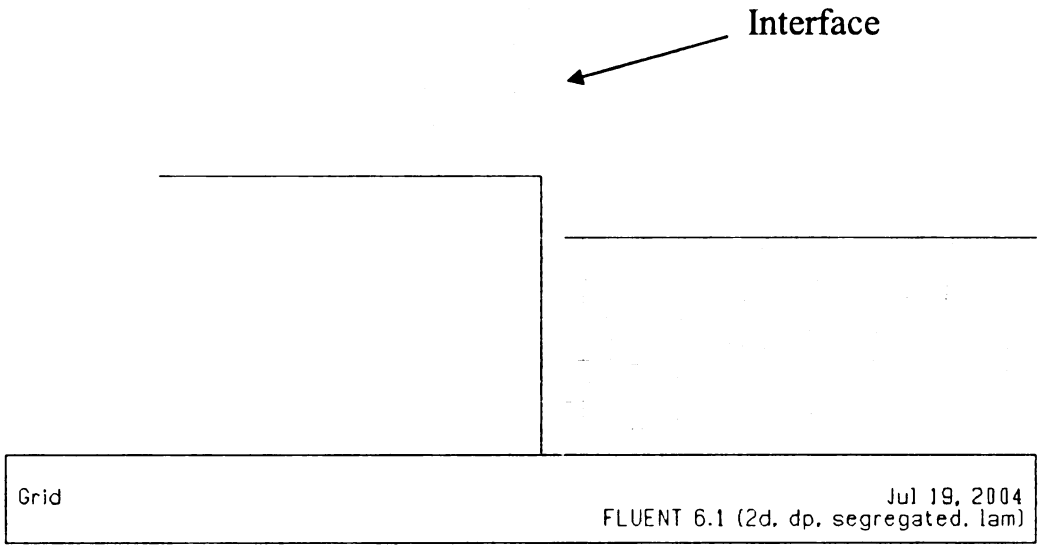

Figure 85: Interface and gap between stationary ports and moving channels

In this study, the governing equations of 2D unsteady laminar flow were selected and solved explicitly with a first order upwind difference scheme. The boundary conditions at the inlet and outlet ports play important roles in the flow filed simulations. These boundary conditions consist of flow pressure and temperature values at the inlet and outlet ports. The compressor exit pressure and temperature were assigned as initial values for the upward moving channels.

5.2.2 Numerical Results

Figure 86 shows contours of total pressure at two succeeding time steps when the first moving channel is exposed to the high-pressure gas inlet port. As expected, the high-pressure flow starts compressing the low-pressure fluid in the channel by generating compression waves. The pressure stratification along the channel length indicates the action of compression waves. These compression waves form a stronger single shock

wave running through the channel. The bottom part of Figure 87 can be interpreted in this way. Figure 87 also shows how the second channel is influenced by the high-pressure gas inlet port as the computational time increases.

Figure 88 depicts the moment when the head of the compression waves nearly meets the right end wall. The top figure indicates the moment before the wall contact, and the bottom figure presents the contact moment. The pressure contours clearly indicate the compression of the air by the compression waves.

Once the compression waves reaches the end wall, a reflected shock wave is generated as shown in the two following time steps in Figure 89. The reflected shock wave compresses the air further. The doubled-compressed air leaves the channel by the opening of the high-pressure air outlet port. A pressure peak well above the inlet pressure is seen at the moment the high-pressure air outlet port opens.

Figure 90 shows how the flow is scavenged from the rotor channels by opening the gas outlet port. This process is supported by the generation of expansion fans traveling through the channels toward the air inlet port.

Finally, the fresh air is ingested into the rotor channels by opening the air inlet port as shown in Figure 91. It is interesting to note that a region of lowest pressure even less than the air inlet pressure (here shown numerically as negative pressure) is created just before opening the air inlet port. This can be interpreted as the reflection of the expansion wave off the left end plate shortly before the air inlet port opens. This low- pressure region significantly assists the ingestion process. Closing the air inlet port terminates the first operating cycle. The pressure contour at this moment is shown in Figure 92. All of the above described phenomena can be seen in this figure.

Figure 93 shows the enhancement of flow circulation in the beginning parts of the channels, which becomes dominant resulting in some outflow from of the channel shortly before the high-pressure gas inlet port closes. In the lower corner of the gas inlet port, the effect of gradual channel opening is magnified as shown in the top section of Figure 94, also showing some leakage effects. The bottom part of Figure 94 represents a focused zone of the upper corner of the high-pressure gas inlet port, indicating less leakage because of flow blockage caused by intense flow recirculation in the beginning of the channels. This flow blockage suggests that a narrower gas inlet port may be substituted for the current wider port.

Figure 95, Figure 96, and Figure 97 show by colors the axial component of relative velocity vectors at air outlet port, gas outlet port, and air inlet port, respectively. For all three ports, recirculated flow regions exist in the upper port corner which again suggests that the port widths for all three ports can be reduced. Whereas the air inlet port shows the strongest recirculation, the air outlet port shows the least.

For the above described figures only the first operating cycle is simulated. To reach a periodic solution, the code needs to be run with more cycles. For instance, convergence to a periodic unsteady state has been achieved after 20 rotations in a study by Fatsis and Ribaud [198, 201]. This can be performed in FLUENT in a 2D simulation by extending the current port arrangements, as shown in Figure 98 for a 3 cycle port arrangement (coarser mesh is used for a better visualization of the reader). Another approach would be a quasi 2D simulation with a 3D model Unfortunately, the generated data requires a huge memory, which was not available for this research. Such a periodic solution, however,

can be simply obtained in the 2D simulation of a radial-flow wave rotor. This is the topic of the next chapter.

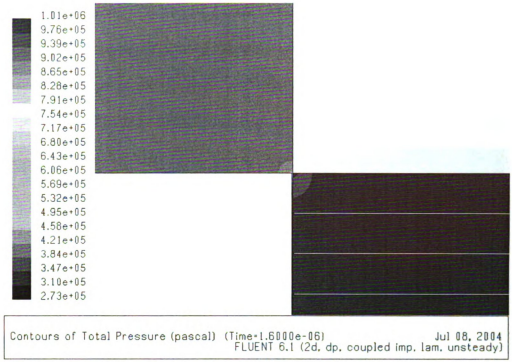

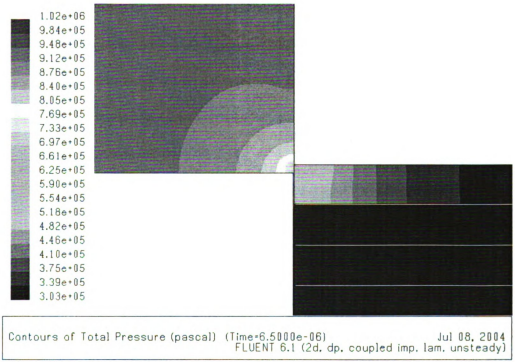

Figure 86: Total pressure contours, the effect of high-pressure gas inlet port on the 1st channel

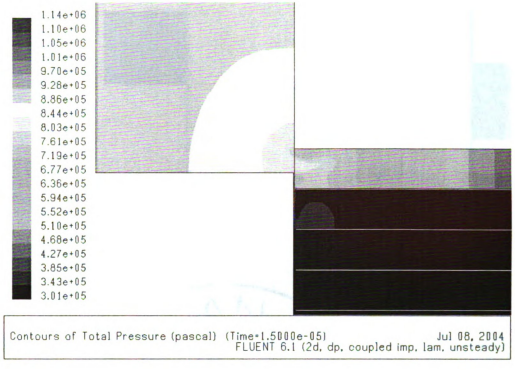

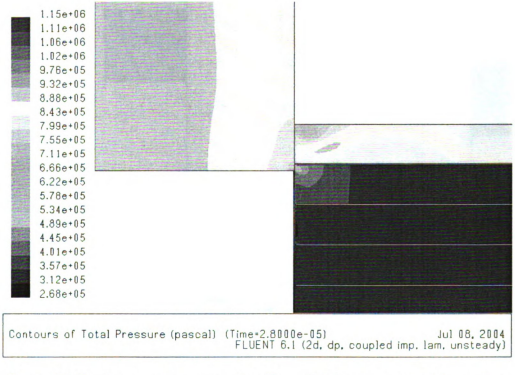

Figure 87: Total pressure contours, the effect of high-pressure gas inlet port on the 1st and 2nd channels

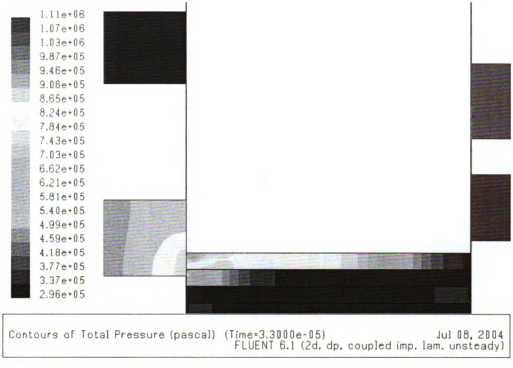

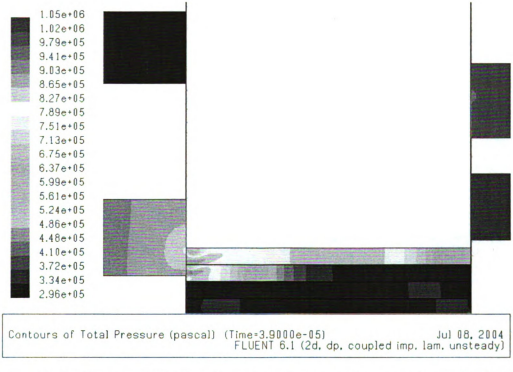

Figure 88: Total pressure contours, traveling of compression waves toward end wall

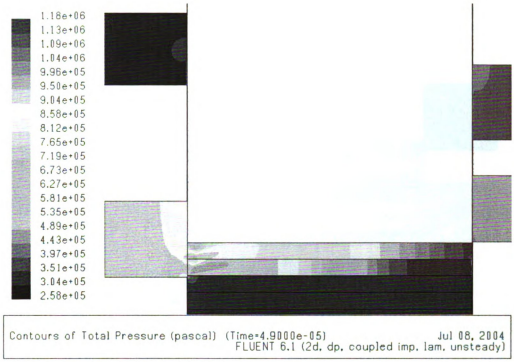

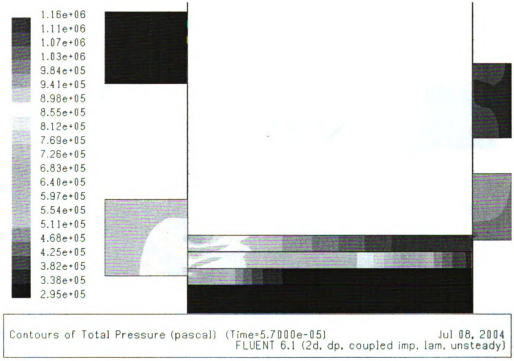

Figure 89: Total pressure contours, generation of reflected shock wave at two different time steps

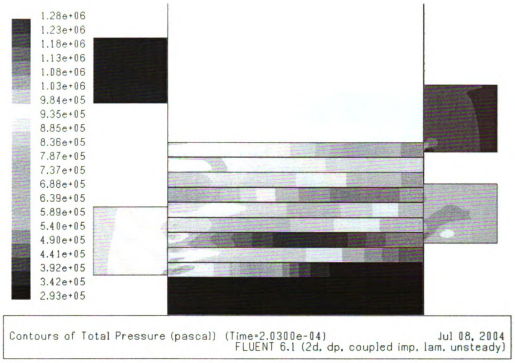

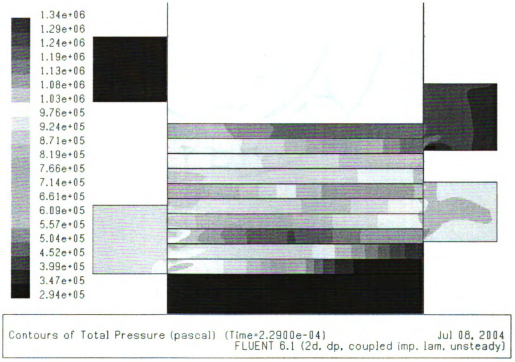

Figure 90: Total pressure contours, air scavenging process at two different time steps

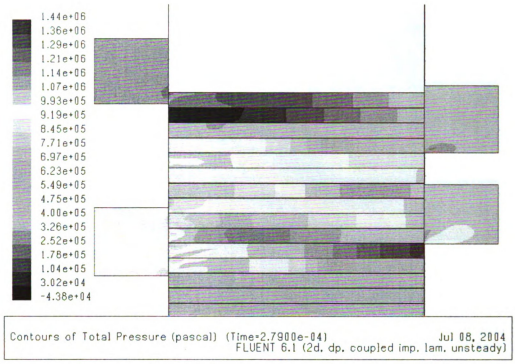

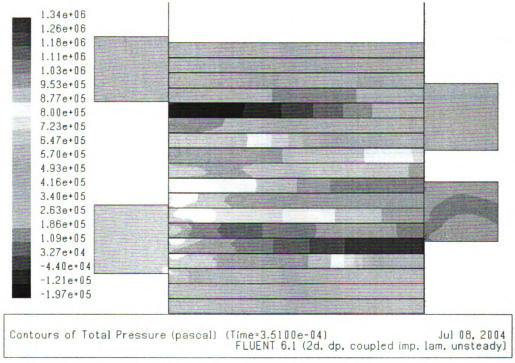

Figure 91: Total pressure contours, ingestion of fresh air at two different time steps

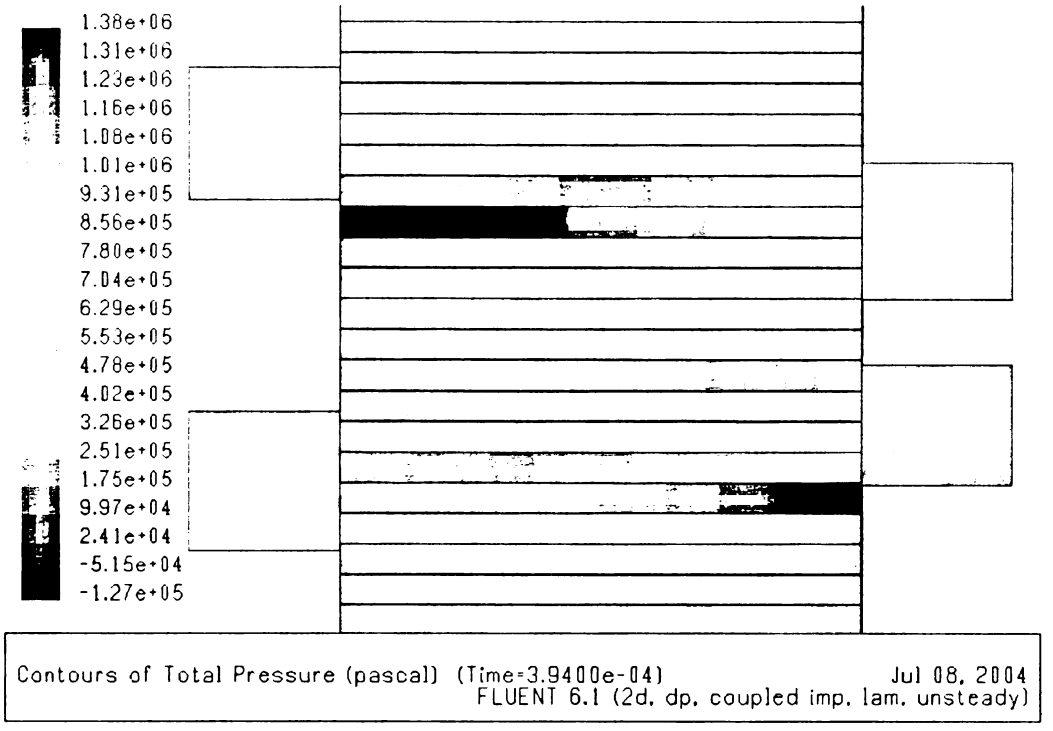

Figure 92: Total pressure contour, end of the first operating cycle

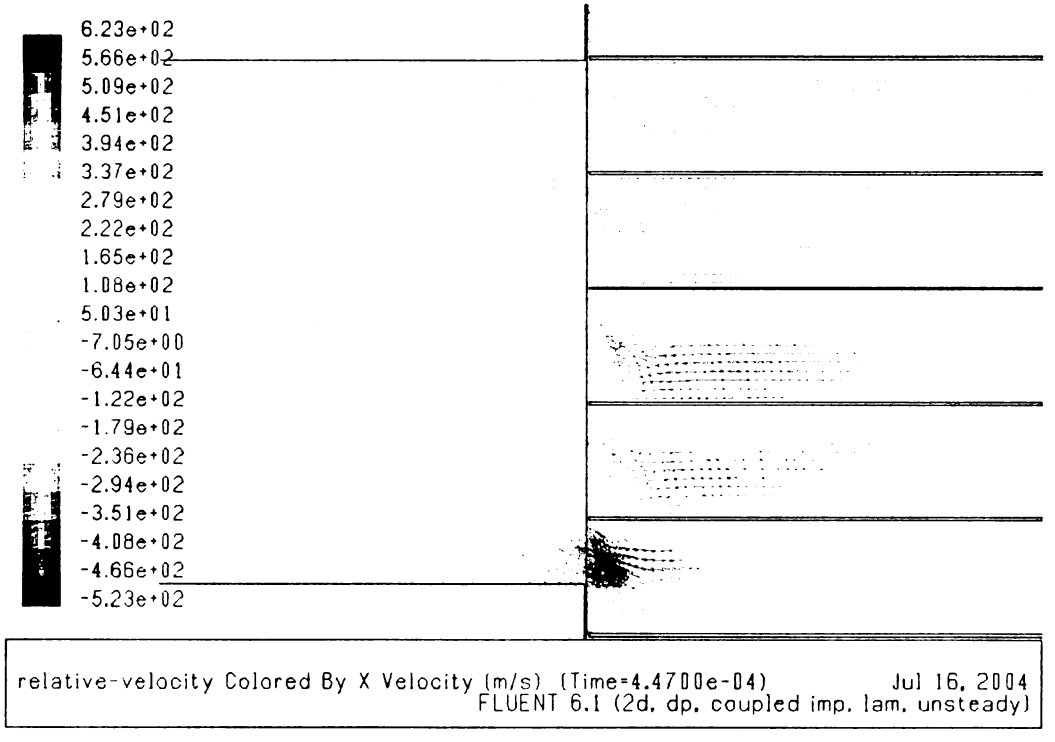

Figure 93: Axial component of relative velocity vector, gas inlet port and channels

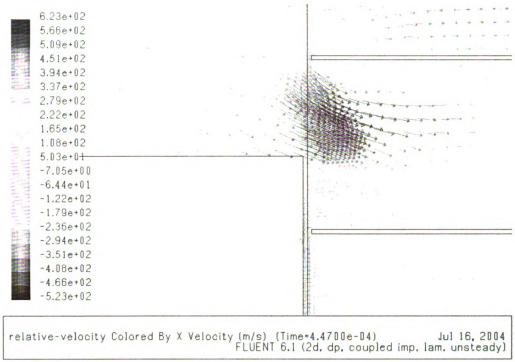

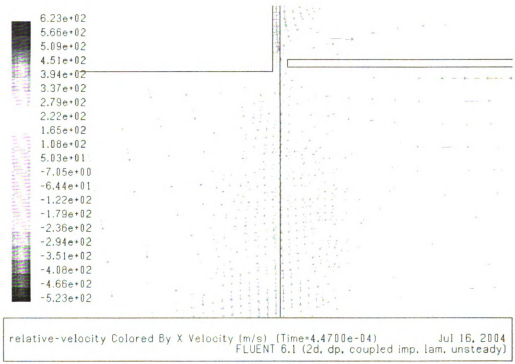

Figure 94: Axial component of relative velocity, lower and upper corners of gas inlet port

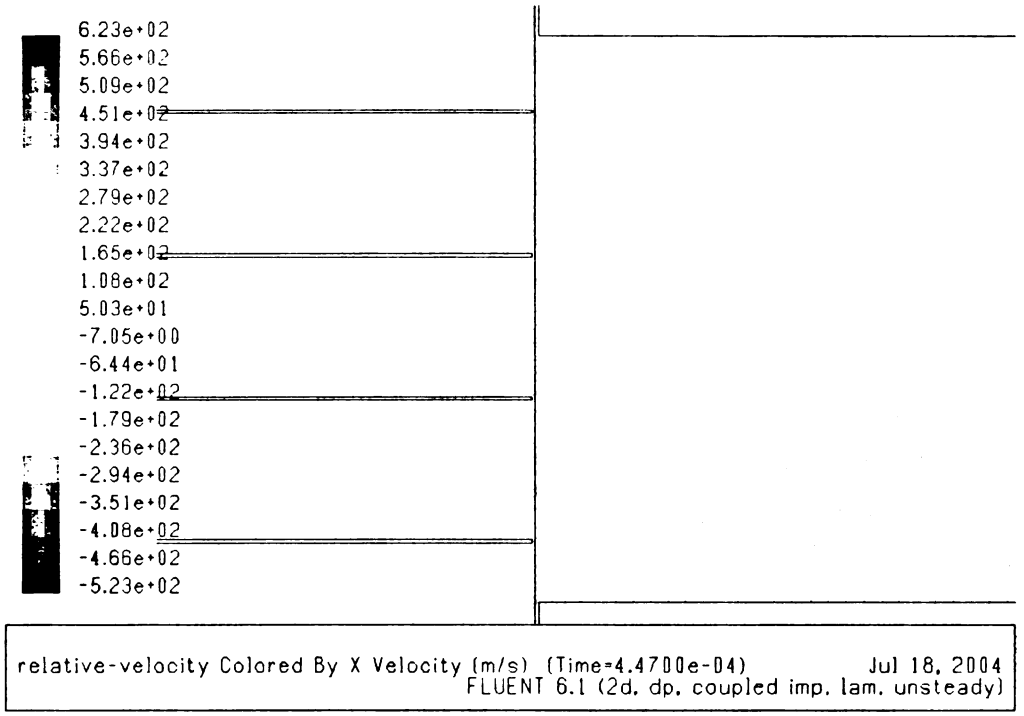

Figure 95: Axial component of relative velocity, air outlet port

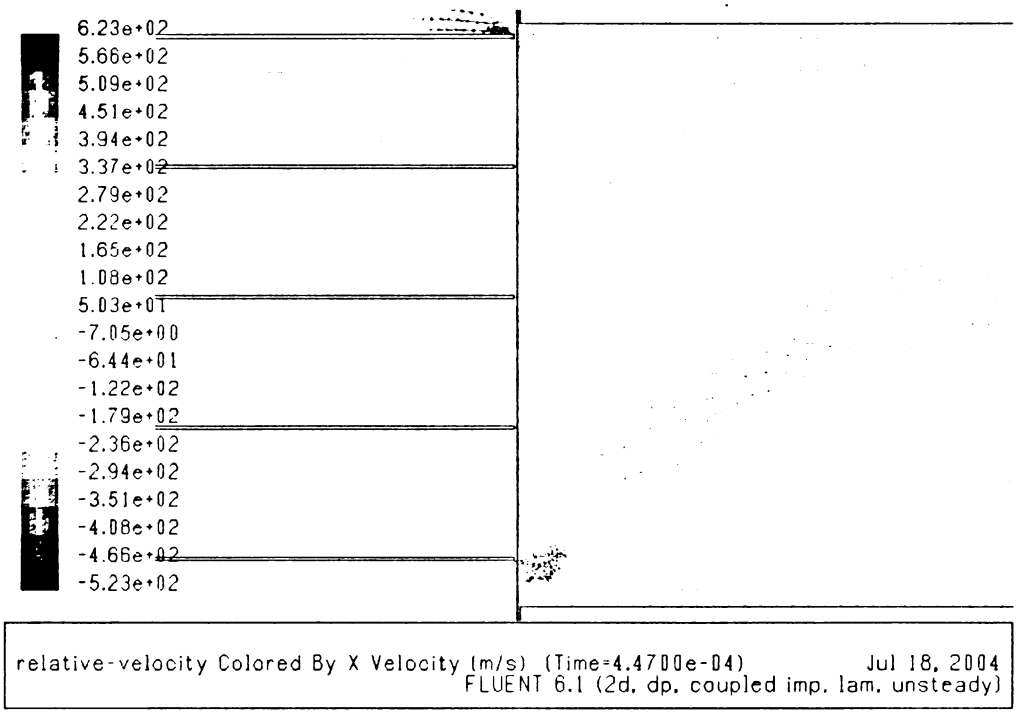

Figure 96: Axial component of relative velocity, gas outlet port

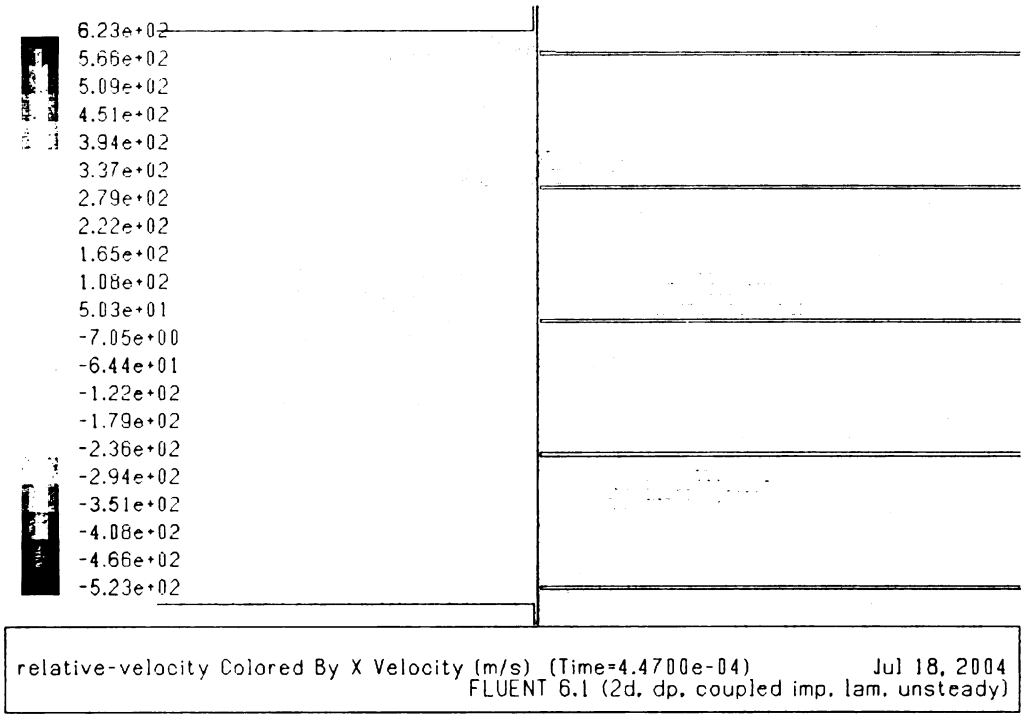

Figure 97: Axial component of relative velocity, air inlet port

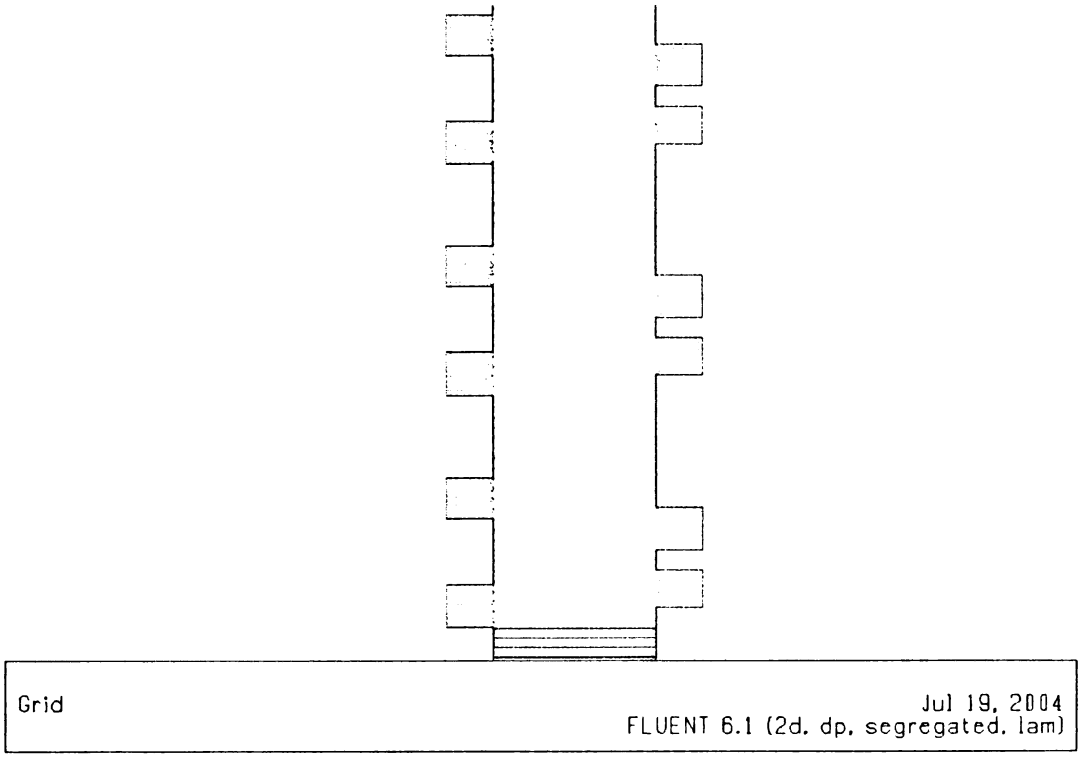

Figure 98: Mesh for multi cycles

CHAPTER 6: INNOVATIVE WAVE ROTOR DESIGNS AND APPLICATIONS

The MSU wave rotor group has initiated studies to evaluate the possible benefits of utilizing wave rotor technology in several thermal cycle applications. Besides the efforts described so far, the team has also investigated and developed several innovative conceptual designs, which will be briefly discussed in this chapter.

6.1 Radial Wave Rotor Concept

As described in the wave rotor history of Chapter 2, for various wave rotor applications several different configurations of mainly axial-flow wave rotors have been studied so far. The four-port version with straight channels has been used most widely. However, pure scavenging is a challenging task in axial-flow configurations. In gas turbine applications, neither the TF configurations nor the RF configurations can often achieve a full scavenging process, as discussed in Chapters 3 and 5. An innovative design taking advantage of centrifugal forces can improve the scavenging process, as described in the following.

6.1.1 Radial-Flow Wave Rotor with Straight Channels

Here, the radial-flow wave rotor concept (wave disc) is introduced employing a flow in the radial and circumferential directions. This can substantially improve the scavenging process by using centrifugal forces. Figure 99 shows schematically a simple radial-flow wave rotor with straight channels and a constant rectangular cross-sectional area. Similar to axial-flow wave rotors, if the driven flow enters and leaves at the inner radius and the driver flow enters and leaves at the outer radius, such a configuration can be referred to as a reverse-flow (RF) design. For a through-flow (TF) configuration, most

of the driven flow travels through the full length of the channel and leaves at the outer end.

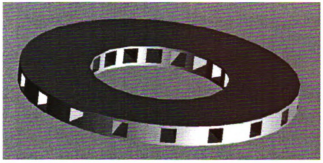

Figure 99: Radial-flow wave rotor with straight channels

To verify the general idea of wave disc operation, where our knowledge is still very limited, the commonly available software package FLUENT has been used to simulate the flow field inside a RF wave disk. Here, using FLUENT it has been shown that the novel concept of wave discs and their particular problems can be investigated by 2D models. The model considered here has 60 straight channels with an inner radius of 0.15 m and outer radius of 0.3 m, rotating clockwise at 8330 rpm as shown in Figure 100. The results presented below have been provided by a collaboration between the MSU wave rotor group and the wave rotor team at Warsaw University in Poland.

Two sets of four ports, as in a conventional four-port wave rotor, are used. It is assumed that the fresh air enters the channels with temperature a of 300 K at a pressure of 10^5 Pa. It is compressed by a high-pressure, high-temperature gas entering at 1000 K and 2.10^5 Pa. The gas expands and leaves at the lower value of 10^5 Pa.

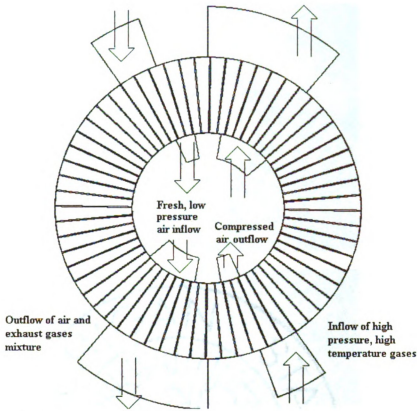

Figure 100: Reverse-flow wave disk with straight channels

From top to bottom, Figure 101 shows contours of local pressure, local temperature, and velocity. Due to the symmetry, only half of the solution is shown. Relatively uniform regions shown before and after the four ports indicate that the combination of diameters, speed, and port arrangement is not optimized, because nearly no changes are seen in these regions. Only the pressure contours show a certain radial stratification in these regions, indicating the action of centrifugal forces. They also clearly show the effects of compression and expansion waves and how the low-pressure region is created by supporting the ingestion of fresh air. The temperature contours clearly show the flow casing especially for the burned gas which is a typical feature of RF configurations. Furthermore, the contours of pressure and velocity show effects of gap leakage, especially on the left side before the high pressure gas port.

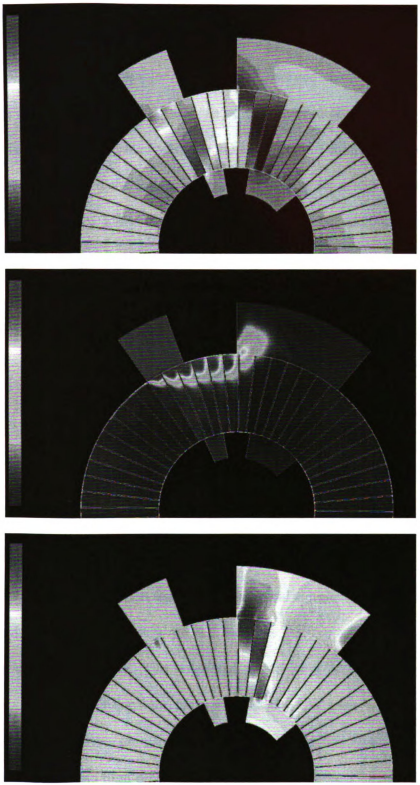

Figure 101: Wave disc with straight channels: contour plots of local pressure (top), local temperature (middle), and velocity (bottom) at time=8.6e-04 s

6.1.2 Radial-Flow Wave Rotor with Curved Channels

As Figure 102 suggests, the channels alternatively may be curved and varied in cross-sectional area. Compared to straight wall channels, curved channels provide a greater length for the same disc diameter, which can be important to obtain certain wave travel times for tuning. With curved channels also the angle against the radius can be changed freely. Furthermore, curved channels may be more effective for self-propelling and work extraction in the case of a wave turbine or work input for additional compression, analogous to the principle of turbomachines.

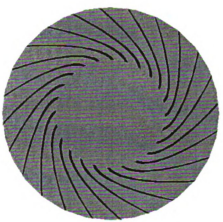

Figure 102: Radial-flow wave rotor with curved channels

Figure 103 is the configuration used in the numerical simulations presented here. The disc radii and number of channels are the same as for the wave disc with straight channels, as explained before. The rotational speed now is 8300 rpm. While the temperature boundary conditions for the ports also are the same as before, now two different high pressure levels are used. In the lower right corner 3.10^5 Pa is set for both high-pressure gas inlet and high-pressure air outlet ports while 2.10^5 Pa for these ports in the upper left corner, both parts being independent.

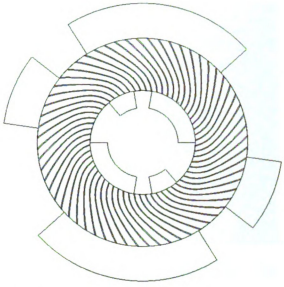

Figure 103: Reverse-flow wave disk with curved channels

The results are presented in Figure 104, showing that compression and expansion are generally working. The static pressure contours show a radial pressure stratification in the regions where both ends of the channels are closed as discussed in Figure 101. The complete temperature contours now show a similar casing like in Figure 101, but with deeper gas penetration and an unexpected carry on of expanding hot gas stretches after the exhaust gas port opens. The penetration is obviously deeper at the right side where the high-pressure level is 3.10^5 Pa.

More results and observations in the simulation of rather complex time-dependent flow phenomena that occur in radial wave rotors are not presented. The reader is referred to Ref. [238] for a complete discussion.

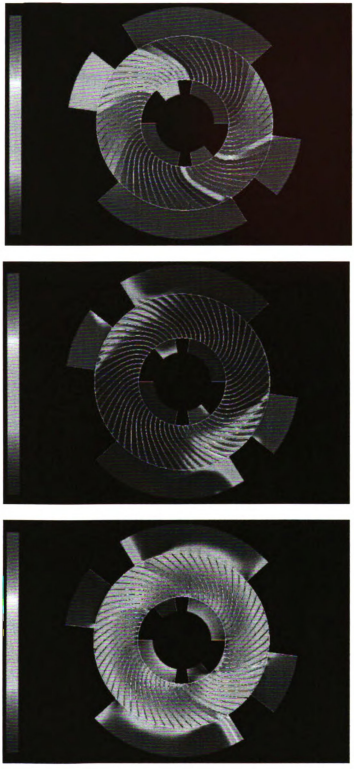

Figure 104: Wave disc with curved channels: contour plots of local pressure (top), local temperature (middle), and velocity (bottom), at time=1.73e-3 s

6.1.3 Radial-Flow Wave Rotor Concept

The wave disc described above can be also stacked together as shown in Figure 105. This way a modular construction is possible that can be adapted for designs with different mass flow rates. Furthermore, similar to the known two-row axial Comprex, the channels are subdivided, which can allow for acoustic noise reduction. Such a wave disc stack can be used in the same way as a single disc wave rotor for different applications like refrigeration, gas turbine topping and supercharging of IC engines.

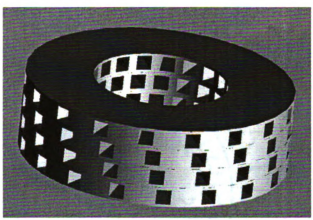

Figure 105: Stack of wave discs with straight channels

Stacked wave discs provide the unique opportunity to place a radial flow turbomachinery at the periphery of the axis of the wave disc stack with an angle such that the turbomachine impeller periphery interfaces all active discs of the stack. In this way, a peripheral continuous outflow from turbomachine impeller and inflow to the disks is possible without any additional ducting, collector, volute, diffuser or nozzle between the turbomachine impeller and the wave rotor. Thus, ducting losses are eliminated, resulting in a higher efficiency of the assembly. Figure 106 shows a configuration in which a radial compressor is placed inside a wave disc stack. Only the inner plate is placed between the impeller and the inner wave rotor. Due to the angle between the axes of the impeller and

wave rotor, the end plate between both can be spherical for minimum thickness (ducting length). This also allows switching on and off outer discs by varying the angle between impeller and wave rotor axis. The port opening can be a continuous oblique slot that interfaces with the impeller periphery. Since the end plates are stationary they can form one part with the housing of the turbo impeller as shown in Figure 106 for the outer impeller shroud and axial duct. The shape at the outer diameter of the wave rotor stack is generated by the shape at the inner diameter, the channel length, inclination and timing of each disc. Still if the outer shape is similar to the inner shape of the wave disc stack, the timing on each disc is different and is determined by the circumferential distance from one port to the other at the inner diameter , as shown schematically in Figure 106.

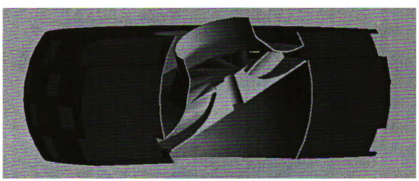

Figure 106: Stacked radial wave discs and radial compressor

In gas turbine applications preferably the turbo-compressor impeller is placed inside the wave rotor. Such a design eliminates the need for a diffuser which has been replaced by a more effective shock deceleration process [1, 2] in the wave disc channels. Using an outward-flow turbine, the turbine could be placed at the outer diameter with its axis also set at an angle to the wave rotor axis but rotating around the wave rotor axis with respect to the compressor axis, allowing a certain time between opening the channels at the inner and outer diameters. Such a configuration might be too challenging and would require

separate shafts for compressor and turbine. To avoid a gear box, their coupling could be achieved electrically via generator and motor. Figure 107 shows a simpler configuration with a direct shaft coupling compressor and turbine as in a gas turbine. This requires a flow collector from the wave rotor outer end plate and certain ducting that directs the flow to the turbine as shown schematically in Figure 108. The configurations shown here uses an internal combustion wave rotor that allows for outward flow only in the wave rotor. If a conventional external combustor is used than an additional port opening is necessary for the burned gases leaving the combustor and the high pressure air entering the combustor. External ducting may then be eliminated by having combustion in the pressure exchange channels.

Figure 107: Cut-view of a radial wave rotor topping a gas turbine

Figure 109 shows an exploded view of a radial wave rotor topping a gas turbine. The outer end plate is shown with an oblique slot as it would also be suitable for a peripherical outer radial outflow turbine. However, for an external turbine as shown here, the slot of the outer end plate can have any form that will adapt most conveniently to the

outlet opening time. In the figures sketched here, a turbine volute is used to distribute the flow around the turbine. The exhaust gas leaves the turbine axially. The reader is referred to Ref. [239] for additional discussions about the radial wave rotor concept.

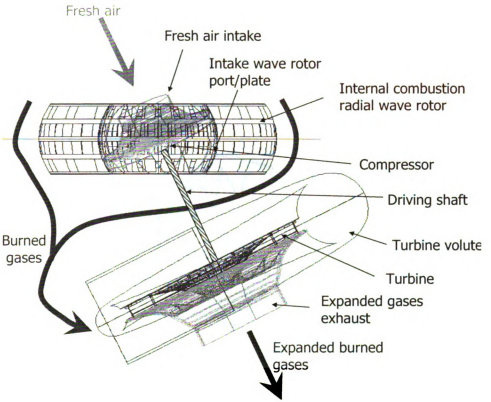

Figure 108: Flow through an internal combustion radial wave rotor topping a gas turbine

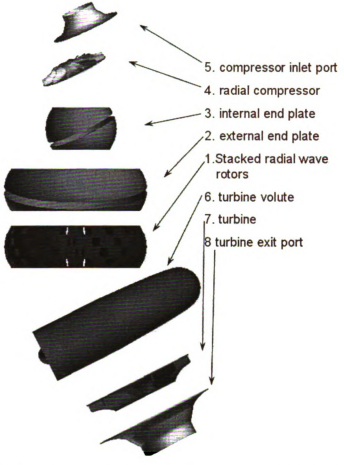

Figure 109: Component parts of a radial wave rotor topping a gas turbine

6.2 Condensing Wave Rotor

Wave rotor technology has the potential to enhance performance and reduce the size and cost of refrigeration cycles using water (R718) as a refrigerant. While R718 refrigeration systems have shown attractive features compared to commonly used refrigeration system, these units often suffer from the expensive and bulky multi-stage turbo-compressors which are crucial units for the R718 chiller technology. Utilizing the wave rotor in such water cycles appears to be a potentially promising solution.

While possibility of integrating four-port wave rotors in R718 cycles has been discussed in a previous study [240], the attention is on utilizing a three-port wave rotor in

R718 units. Utilizing a three-port wave rotor, know as the condensing wave rotor, appears more promising because it combines the function of a compressor stage and the condenser in one compact unit. Both pressure rise and condensation occur inside the wave rotor channels as described below.[4]

6.2.1 How Does a Condensing Wave Rotor Work?

Figure 110 depicts schematically a R718 cycle with a direct condenser and a direct evaporator. Figure 111 shows a schematic of a R718 cycle using a three-port condensing wave rotor. A comparison between these two cycles indicates that the wave rotor has substituted three subsystems: the condenser, one compressor stage, and the intercooler (now shown). A schematic design of a condensing wave rotor is depicted in Figure 112. In this innovative design, condensation of vapor occurs inside the wave rotor channels as depicted in Figure 113 and Figure 114. Figure 113 schematically shows a model for the condensation process inside a channel of a three-port condensing wave rotor. Figure 114 shows a corresponding schematic wave and phase-change diagram.

[4] Materials presented in this section have been accepted for publication in *2005 ASME Journal of Engineering for Gas Turbines and Power.*

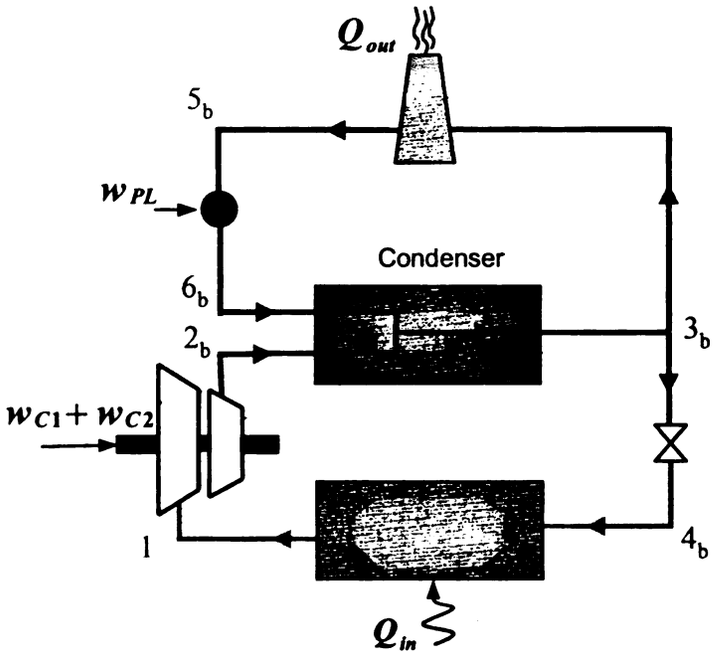

Figure 110: Schematic of a R718 cycle with direct condensation and evaporation

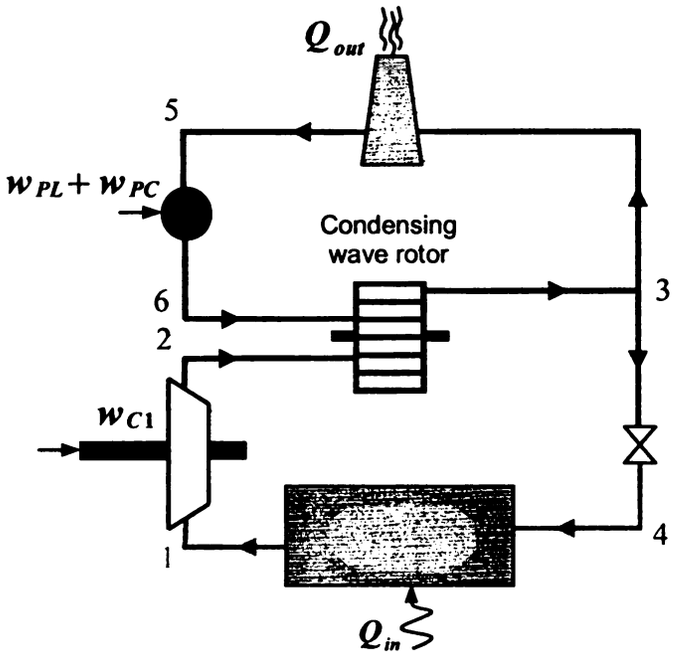

Figure 111: Schematic of a R718 cycle enhanced by a three-port condensing wave rotor substituting for the condenser and for one compressor stage

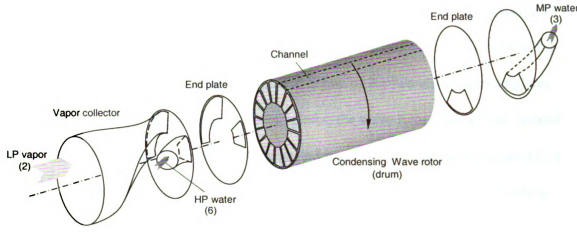

Figure 112: Schematic of a three-port condensing wave rotor

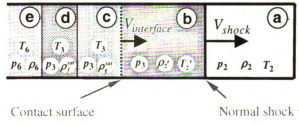

Figure 113: Regions modeled for each compression and condensation

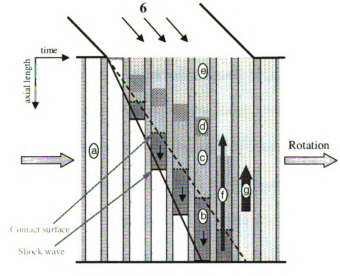

Following the points introduced in Figure 111, coming from the turbo-compressor (2), the superheated vapor flows continuously through a vapor collector (shown in Figure 112) to the inlet port of the wave rotor located at one of the two stationary end plates. By rotating the wave rotor between the two end plates, the wave rotor channels are opened to the port and filled with the incoming superheated vapor. The region (***a***) in Figure 113 and Figure 114 is the state after the filling process is completed. After further rotation, the channels meet the second-inlet port (6) through which the high-pressure low-temperature water (***e***) comes in and is exposed to the low-pressure high-temperature superheated vapor in region (***a***). Due to the sudden pressure drop (from p_6 to p_2), all the heat cannot be contained in the incoming water as sensible heat and the heat surplus is transformed into latent heat of vaporization. This is the so called flash evaporation or flashing phenomenon [241, 242]. Therefore, one portion of the incoming water suddenly vaporizes (***c***) and the remaining part cools down (***d***). The frontal area of the saturated vapor (***c***) generated by the flash evaporation is called the contact interface and acts like a fast moving piston. It causes a shock wave triggered from the leading edge of the inlet port traveling through the superheated low-pressure vapor which exists inside the channel (***a***). The shock wave travels with supersonic speed (V_{shock}) faster than the contact interface ($V_{interface}$). Therefore, the trajectory of the shock wave (solid line in Fig. 6) has a smaller slope than the incoming water and the contact interface of the generated vapor (dashed line). Behind the moving shock wave (***b***) the temperature is increased from T_2 to T_2' and the pressure is increased from p_2 to $p_2'=p_3$ due to the shock compression. The latter is a design decision similar to a tuning condition. With it, the pressure at the inlet port (p_6) is set to an appropriate value that generates the pressure ratio p_6/p_2 required to

trigger the desired shock wave. The superheated vapor will be condensed at pressure p_3 . This shows that the fluid in its liquid state serves as a "work capacitor" storing pump work to release it during its expansion in the wave rotor channels for the simultaneous vapor compression. Therefore, in the enhanced system the pump in the cooling water cycle not only has to provide the work necessary to overcome the pressure loss in the heat rejecter cycle (w_{PL}) but also the work necessary for the shock wave compression in the wave rotor channels (w_{WC}). The pressure behind the shock wave (***b***) is imposed on the vapor generated by the flash evaporation (***c***). It is the pressure at the water surface and the equilibrium pressure at which the evaporation decays $p(c)=p(b)=p_3$. Hence, both generated vapor and the cooled water obtain the saturation temperature $T_3=T_{sat}(p_3)$.

Due to the contact of the superheated compressed vapor (***b***) with the cold incoming water, the superheated vapor is desuperheated and its heat is transferred (***f***) to the incoming water. This continues until the equilibrium temperature T_3 is achieved in region (***b***) and the superheated vapor is changed to saturated vapor. Subsequently, the incoming water compresses the saturated vapor further and condenses it, while the latent heat is transferred to the incoming water (***g***). The water, which is nearly a fully condensed two-phase vapor with a typical quality of 0.005, is scavenged through the only outlet of the wave rotor (3). The scavenging process may be supported by gravity and pump power.

The schematic pressure-enthalpy (p-h) and temperature-entropy (T-s) diagrams of both the baseline and the wave–rotor-enhanced cycle are depicted in Figure 115 and Figure 116, respectively.

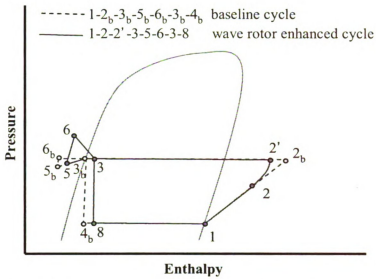

Figure 115: Schematic p-h diagram of a R718 baseline cycle and a wave rotor enhanced cycle

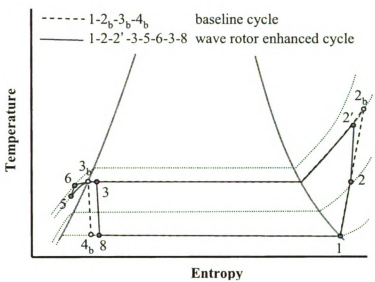

Figure 116: Schematic T-s diagram of a R718 baseline cycle (cooling water cycle not shown) and a wave rotor enhanced cycle

Both cycles start at the outlet of the evaporator 1, where the vapor is saturated. State 2_b represents the compressor outlet of the baseline cycle whereas state 2 is the compressor outlet of the wave-rotor-enhanced cycle that allows using a compressor with

a lower pressure ratio. State 2′ is an intermediate state inside the wave rotor channels that corresponds to the flow properties in region (***b***) right after the shock wave. The slope between points 2 and 2′ is greater than that between points 1 and 2_b because the shock compression typically occurs with a higher efficiency. Still inside the wave rotor channel, the superheated vapor is desuperheated to the equilibrium temperature T_3 (2′→3). State 3 is actually much closer to the liquid region than shown in Figure 115 and Figure 116 because the mass flow rate of the cooling water cycle is much greater than that of the refrigerant cycle. Knowing this, it becomes clear that the distances between points 3, 5, and 6 are exaggerated in both diagrams. The expansion process (6→3) releases the energy consumed by the compression process of the vapor (2→2′) all within the wave rotor channels. Coming from the only outlet port of the wave rotor (3), the flow diverges. The small fraction used as refrigerant is directed to the expansion valve and is expanded in a constant enthalpy process (3→ 4), while most of the flow out of the wave rotor goes into the heat rejecter (cooling tower or similar) where it cools (3→ 5). Afterwards the pressure is again increased (5→6) by the pump, providing the energy for the vapor compression in the wave rotor (w_{WC}) and compensating for the pressure loss in the heat rejecter and associated piping (w_{PL}).

6.2.2 Performance Evaluation

Using a thermodynamic model described in Ref. [243, 244], a performance map of the enhanced cycle is obtained as shown in Figure 117. For each point on this plot, the mass flow ratio between the cooling water cycle and the chilled water cycle is considered as a fixed value, e.g. here, $K=m_6/m_2=125$. Reference [245] describes how increasing the mass flow ratio above 200 appears ineffective for the COP_{gain} (COP increase of enhanced cycle relative to the base cycle divided by the COP of the baseline cycle) and the gradient

of the COP_{gain} increase above K=125 is not significant. According to Figure 117, each point on this plot shows the maximum COP_{gain} that can be obtained by the optimum choice of PR_W for a given evaporator temperature and a temperature-lift meaning that for each evaporation temperature and temperature-lift combination, PR_W is varied within a certain range ($1 < PR_W < 4.5$). Then among all COP_{gain}s recorded, the maximum COP_{gain} is the optimum value. On the other hand, the constant PR_W lines indicate the optimum PR_W that yields the highest possible COP_{gain} indicated by the $max.COP_{gain}$ lines. This graph reveals a theoretical improvement of the COP up to 22% using the three-port condensing wave rotor.

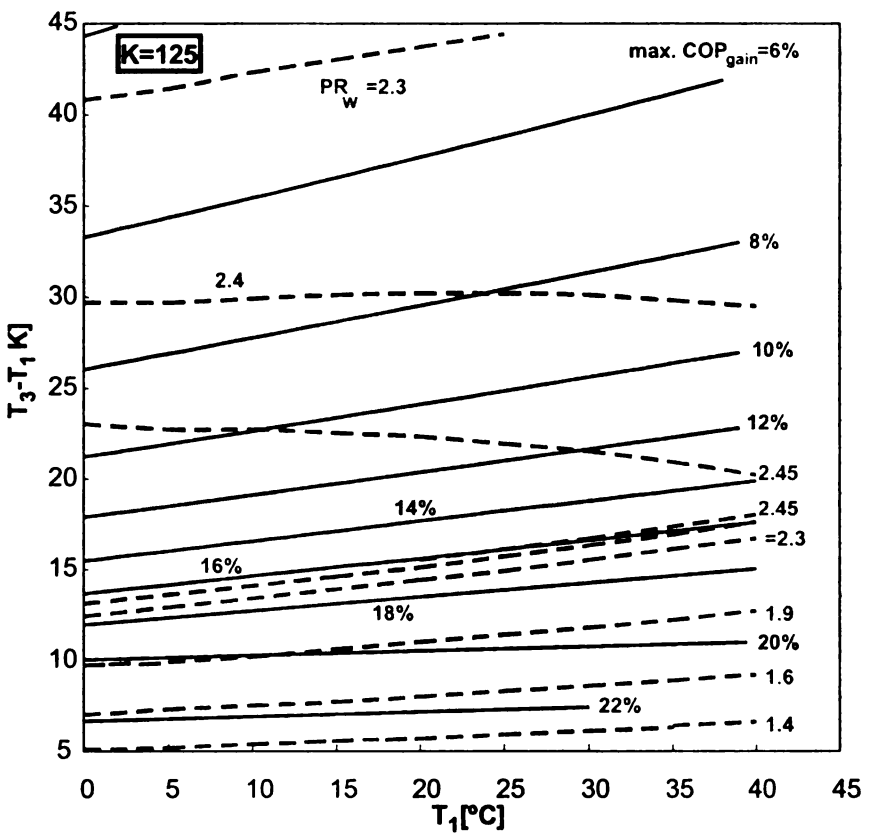

Figure 117: Performance map representing maximum performance increase and optimum wave rotor pressure ratios

6.3 Wave Rotors for Ultra-Micro Gas Turbines

Ultra-micro gas turbines (UμGT) are seen as appropriate solutions for propelling mini unmanned air-vehicles (UAV) and powering miniaturized wireless sensors and equipment on board. This vision has been inspired by the improvements in Micro Electrical Mechanical Systems (MEMS) technology. Furthermore, these microfabricated gas turbines are suitable for high-density, distributed and redundant power generation on aircrafts, and other vehicles. A typical size of an UμGT is 20mm × 20mm × 4mm. An UμGT can achieve higher power densities compared to larger gas turbines as indicated by the so called Cube-Square Law. Because the output power is proportional to the mass flow rate of working fluid through the engine and the mass or volume of the engine is proportional to the cube of the characteristic length, the power density (Power/Mass=L^{-1}) is increased as the device is miniaturized.

However, investigations of such UμGT have shown difficulties in obtaining high thermal efficiencies and output power levels. The reasons are additional losses due to miniaturization and the dominant 2D geometries typical for MEMS-fabrication technology. The flow paths often encounter 90-degree bends, which are known to decrease efficiency and mass flow rate. The compressor isentropic efficiency typically drops to $\leq$ 60% [246]. Here, innovations are sought to attractively enhance the low performance of the UμGT. Utilizing wave rotor technology, the idea of integrating a wave rotor into an UμGT is proposed by the MSU wave rotor team. This section briefly review some of the challenges and advantages of conceptual designs integrating wave rotor devices into such small engines [247].

6.3.1 Performance Enhancement of UμGT Using Wave Rotors

The way in which the wave-rotor topping enhances the cycle at the micro scale often differs from that at larger scales. In the large scale, for a fixed turbine inlet temperature, the goal is generally either to increase the cycle overall pressure ratio (Case A) or to substitute for costly high pressure turbomachinery stages with the wave rotor (Case B). At the ultra-micro scale, the optimum cycle pressure ratio is very small, e.g. around 2, due to the low component efficiencies. Thus, a single-stage centrifugal compressor can easily generate the low optimum overall pressure ratio and a further increase with the same efficiency actually decreases the desired performance. Therefore, the wave rotor integration is most effective if its compression and expansion efficiencies are greater than those of the turbomachinery components of the baseline engine. This enhances not only the overall compression and expansion efficiencies, but it also increases the optimum cycle pressure ratio to a greater value that allows for additional performance improvements. In such a case in which the wave rotor compression efficiency is higher than that of the spool compressor, a wave rotor can enhance the performance of an UμGT that was already designed for an optimum pressure ratio. While the optimum overall compression ratio increases with the wave rotor integration, usually the pressure ratio of the spool compressor decreases. This can additionally enhance the isentropic efficiency of the spool compressor, provided its polytropic efficiency (aerodynamic quality) stays the same [246].

As described before, the efficiencies of both compression and expansion processes in a wave rotor have been found to be greater than 70%. This may be considered as matching the efficiency of large scale compressors or turbines and as almost double of that achieved with UμGT compressors. Exploring the application of even smaller wave

rotors suitable for UμGT, the question arises if such wave rotor efficiencies can be maintained at the ultra-micro scale. No experimental and theoretical values are available at this scale. However, recent results show no or only a small decrease in efficiency with reduced size, which encourages investigations at the ultra-micro scale. Recent research has shown only a small decrease in efficiency of small wave rotors. For example, for a small-scale wave rotor with a channel length of 69 mm, the wave-rotor characteristic equation introduced in Eq. (38) calculates a compression efficiency of 79% using the parameters provided by Okamoto and Nagashima [213, 215].

Using the available wave rotor efficiencies above versus the corresponding wave rotor channel length, a trend can be generated as shown by the solid green line in Figure 118. The simple linear extrapolation predicts a wave rotor efficiency at the ultra-micro scale (about 1mm channel length) that is greater than 70%. Such a compression efficiency of a microfabricated wave rotor is much better than the obtained efficiencies of around 50% for microfabricated compressors [246]. Furthermore, efficiency values of compressors suitable for or corresponding to the reported wave rotor topped cycle are shown in red in Figure 118. This allows showing the red broken trend line for the compressor efficiency corresponding to the wave rotor length. Both trends for the wave rotor efficiency and for the compressor efficiency coincide at the larger scale. However, towards the smaller wave rotor size for UμGT, the compressor efficiency trend falls far below the wave rotor efficiency trend. This clearly suggests an advantage of using a wave rotor for the UμGT.

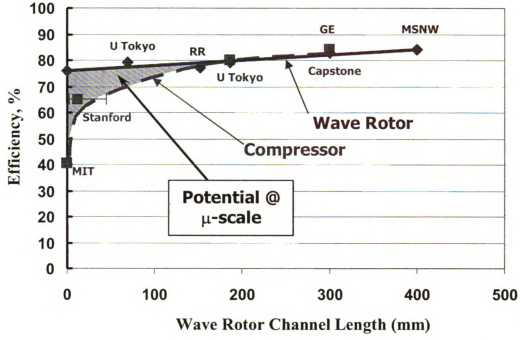

Figure 118: Efficiency trend of compression process. Green: wave rotor efficiency, Red: compressor efficiency

6.3.2 Conceptual Designs of Wave Rotor Implementation into UμGT

Based on possible design restrictions and preferences, three different advantageous conceptual designs for a four-port (or multiple of that) wave rotor integrated into a baseline UμGT are suggested. Figure 119 shows a wave rotor added at outer diameter of the disk of the "classical" MIT baseline design [248]. This innovative design has several advantages. The wave rotor rotates with the compressor/turbine disk, i.e., there is still only one rotating disk in the engine. Additionally, because the wave rotor is a self-cooled device, it isolates the compressor disk from the combustion chamber while in the wave rotor the heat is given to the compressed air adding a recuperative effect. The end plates with the ports at either side of the wave rotor can be etched in the same wafer as the stationary guide vanes.

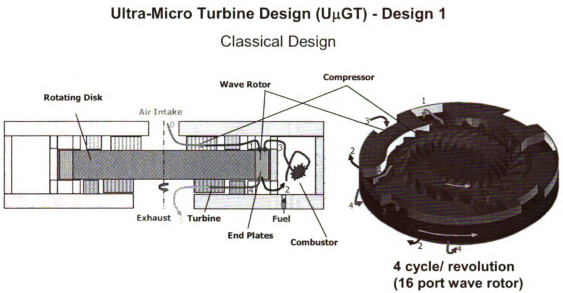

Figure 119: First conceptual design of an UμGT equipped with a four-port wave rotor

The second possible design implies using additional wafers allowing a multi layer rotor, as shown in Figure 120. However, the diameter of the rotor is smaller than in the first design. This results in a smaller frontal area, which is favorable for the propulsion of air vehicles and may generate less stress in the disks. Further, this design allows for better separation of the combustion chamber from the compressor, reducing the heat introduced to the compressor. The major challenge with this design is the perfect axial alignment of the compressor/turbine unit with the wave rotor, which may be achieved with the common laser aligning method. The flow connection from the compressor to the wave rotor may be viewed as a challenge with respect to keeping the pressure loss small. However, the equivalent diameter of this connection may be designed sufficiently large. Further, this may aid in isolating the compressor case from the combustor heat, especially with the counter flow of the compressed air, where a regenerative effect is seen again.

Ultra-Micro Turbine Design (UμGT) - Design 2

Two-Layer Design

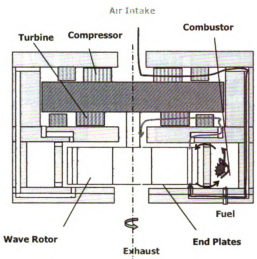

Figure 120: Second conceptual design of an UμGT equipped with a four-port wave rotor

The third design concept introduces a new idea having multiple wave rotors arranged circumferentially around the compressor/turbine unit, as shown in Figure 121. The advantage of this design is that no additional stresses occur in the main rotor, which is the compressor/turbine disk. The stresses in the separate small diameter wave rotors are negligible since they can rotate at a relatively low speed. Similar to the first classic design, this design requires fewer layers then the second design, which translates into a lower fabrication cost. The challenge associated with this design is driving all wave rotors at appropriate speed. This may be achieved by arranging the wave rotor ports at proper and suitable angles, so that the impulse of the fluid streams can be utilized.

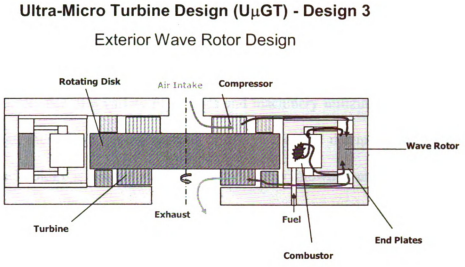

Figure 121: Third conceptual design of an UμGT equipped with a four-port wave rotor

CONCLUSION

Wave rotor technology has shown unique capabilities to enhance the performance and operating characteristics of a variety of engines and machinery utilizing thermodynamic cycles. Although there have been numerous efforts in the past dealing with this novel concept, this technology is not yet widely used and barely known to engineers. Here, an attempt was made to investigate this novel technology further and to show its significant potential for performance gain in small gas turbines. This work has extensively discussed the following topics:

- **Comprehensive Review of Wave Rotor Technology**

The presented research summarizes both the previously reported work in the literature and ongoing efforts around the world. It covers a wide range of wave rotor applications including the early attempts to use wave rotors, its successful commercialization as supercharges for car engines, research and development for gas turbine topping, and other developments. The review also pays close attention to more recent efforts, e.g. utilization of such devices in pressure-gain combustors, highlighting possible further efforts on this topic. Observations and lessons learnt from experimental studies, numerical simulations, analytical approaches, and other design and analysis tools were presented.

- **Performance Prediction of Gas Turbine Topping Wave Rotors**

Significant performance enhancement of two microturbines (30 and 60 kW) was predicted by implementing various wave rotor topping cycles. Five different advantageous cases were considered for implementation of a four-port wave rotor into the given baseline engines. The compressor and turbine pressure ratios and the turbine inlet temperatures vary in the thermodynamic calculations, according to the anticipated design

objectives of the cases. Advantages and disadvantages were discussed. To evaluate the performance enhancement of topping small gas turbines with wave rotors, a computer program based on a thermodynamic approach was created to determine the thermodynamic properties of the gases in different states of the cycles. The results were used to calculate the theoretical performance and the actual T-s diagrams of both wave-rotor-topped and baseline engines. The unrecuperated engines were predicted to have thermal efficiency and specific work enhancement up to 34% for the smaller engine and 25% for the larger engine, using a four-port wave rotor with a compression ratio of 1.8. Similar approach has predicted an improvement up to 15% of overall efficiency and specific thrust in a turbojet engine using the wave-rotor-topping cycle of 30 kW microturbine flying at an altitude of 10,000 m at Mach 0.8. The 30 kW recuperated engine was predicted to achieve thermal efficiency and specific work enhancement up to 7% and 38%, respectively, by implementing Case A where the baseline compressor and turbine remain unchanged. In addition, the impact of ambient temperature on performance of both baseline and topped engines was investigated and it was shown that the wave-rotor-topped engines are less prone to performance degradation under hot-weather conditions than the baseline engines

- **Development of an Analytical Preliminary Design Procedure**

A one-dimensional analytical gasdynamic model of the charging process was employed to calculate flow characteristics inside the wave rotor channels. Three different wave patterns were considered. The first scenario uses a single shock wave and an expansion wave. This situation may occur when the combustor pressure loss is relatively small and hence the total pressure difference between the incoming hot gas and outgoing compressed air is small. It was shown that for a tuned condition, this particular scenario

requires a huge channel height, resulting in an undesirably bulky wave rotor. The second wave pattern employs two primary shock waves to perform the charging operation. It was discussed that while the charging process is theoretically feasible, this case is rarely seen in wave rotor designs. Therefore, the attention was given to last studied case which employs a primary shock wave, a reflected shock wave, and an expansion wave. This is the wave diagram often exists in the charging process of four-port wave rotors. For all three cases considered here, useful design parameters such as port widths and rotor size are determined by computing transit times of the waves traveling inside the channels. To verify the accuracy of the model, the results were compared with some previous numerical data which are available for conventional wave rotors. Reasonable agreement has been found comparing the predicted results of the model with the numerical data.

- **Numerical Simulations with FLUENT**

A successful attempt at developing 2D models of wave rotors using the commonly available CFD software FLUENT was performed. It was shown that such an available software package can be effectively used for simulation of rather complex time-dependent flow phenomena that typically occur in wave rotors, resulting in a wide range of information about the unsteady processes.

- **Innovative Wave Rotor Designs and Applications**

Several innovative and cutting-edge application of wave rotors were suggested and discussed. These concepts include radial-flow wave rotors, integrating wave rotors in ultra-micro gas turbines (UμGT), and water refrigeration systems working with wave rotors.

As the final note, while new knowledge and technology innovations have provided a new opportunity to consider wave rotor concept as innovative technology, still sealing and thermal expansion appear to be dominant problems despite continued research. Special technology developments and additional research on wave rotors overcoming some of present challenges and limitations are needed.

REFERENCES

[1] Weber, H. E., 1986, "Shock-Expansion Wave Engines: New Directions for Power Production," ASME Paper 86-GT-62.

[2] Weber, H. E., 1995, *Shock Wave Engine Design*, John Wiley and Sons, New York.

[3] Kentfield, J. A. C., 1998, "Wave Rotors and Highlights of Their Development," AIAA Paper 98-3248.

[4] Darrieus, G., 1950, "Pressure Exchange Apparatus," US Patent 2526618.

[5] Kentfield, J. A. C., 1993, *Nonsteady, One-Dimensional, Internal, Compressible Flows*, Oxford University Press, Oxford.

[6] Gyarmathy, G., 1983, "How Does the Comprex Pressure-Wave Supercharger Work?," SAE Paper 830234.

[7] Zehnder, G., Mayer, A. and Mathews, L., 1989, "The Free Running Comprex®," SAE Paper 890452.

[8] Hiereth, H., 1989, "Car Tests With a Free-Running Pressure-Wave Charger - A Study for an Advanced Supercharging System," SAE Paper 890 453.

[9] Zauner, E., Chyou, Y. P., Walraven, F., and Althaus, R., 1993, "Gas Turbine Topping Stage Based on Energy Exchangers: Process and Performance," ASME Paper 93-GT-58.

10] Welch, G. E., 2000, "Overview of Wave-Rotor Technology for Gas Turbine Engine Topping Cycles," Novel Aero Propulsion Systems International Symposium, The Institution of Mechanical Engineers, pp. 2-17.

11] Knauff, R., 1906, "Converting Pressures of Liberated Gas Energy into Mechanical Work," British Patent 2818.

[12] Pearson, R. D., 1982, "Pressure Exchangers and Pressure Exchange Engines," Chapter 16, *The Thermodynamics and Gas Dynamics of Internal Combustion Engines*, Vol. 1, Benson, R., Oxford University Press., pp. 903-940.

[13] Knauff, R., 1906, "Converting Internal Gas Energy into Mechanical Work," British Patent 8273.

[14] Burghard, H., 1913, British Patent 19421.

[15] Lebre, A. F., 1928, British Patent 290669.

[16] Burghard, H., 1929, German Patent 485386.

[17] Meyer, A., 1947, "Recent Developments in Gas Turbines," Journal of Mechanical Engineering, **69**, No. 4, pp. 273-277.

[18] Real, R., 1946, "The 3000 kW Gas Turbine Locomotive Unit," Brown Boveri Review, **33**, No. 10, pp. 270-271.

[19] Meyer, A., 1947, "Swiss Develop New Gas Turbine Units," Electrical World, **127**, pp. 38-40.

[20] Azoury P. H., 1992, *Engineering Applications of Unsteady Fluid Flow*, John Wiley and Sons, New York.

[21] Rose, P. H., 1979, "Potential Applications of Wave Machinery to Energy and Chemical Processes," Proceedings of the 12th International Symposium on Shock Tubes and Waves, pp. 3-30.

[22] Seippel, C. ,1940 Swiss Patent 225426.

[23] Seippel, C., 1942, Swiss Patent 229280.

[24] Seippel, C., 1946, "Pressure Exchanger," US Patent 2399394.

[25] Seippel, C., 1949, "Gas Turbine Installation," US Patent 2461186.

[26] Berchtold, M., Gardiner, F. J., 1958, "The Comprex: A New Concept of Diesel Supercharging," ASME Paper 58-GTP-16.

[27] Berchtold, M., 1958, "The Comprex Diesel Supercharger," SAE Paper 63A.

[28] Berchtold, M., Gull, H. P., 1959, "Road Performance of a Comprex Supercharged Diesel Truck," SAE Paper 118U.

[29] Taussig, R. T., Hertzberg, A., 1984, "Wave Rotors for Turbomachinery," Winter Annual Meeting of the ASME, edited by Sladky, J. F., Machinery for Direct Fluid-Fluid Energy Exchange, AD-07, pp. 1-7.

[30] Doerfler, P. K., 1975, "Comprex Supercharging of Vehicle Diesel Engines," SAE Paper 750335.

[31] Schruf, G. M., Kollbrunner, T. A., 1984, "Application and Matching of the Comprex Pressure-Wave Supercharger to Automotive Diesel Engines," SAE Paper 840133.

[32] Zehnder, G., Mayer, A., 1984, "Comprex® Pressure-Wave Supercharging for Automotive Diesels - State-of-the-Art," SAE Paper 840132.

[33] Berchtold, M., 1985, "The Comprex®," Proceeding ONR/NAVAIR Wave Rotor Research and Technology Workshop, Report NPS-67-85-008, pp. 50-74, Naval Postgraduate School, Monterey, CA.

[34] Azoury, P. H., 1965-66, "An Introduction to the Dynamic Pressure Exchanger," Proceedings of the Institution of Mechanical Engineers, **180**, Part 1, No. 18, pp. 451-480.

[35] Guzzella, L., Wenger, U., and Martin, R., 2000, "IC-Engine Downsizing and Pressure-Wave Supercharging for Fuel Economy," SAE Paper 2000-01-1019.

[36] Mayer, A., Oda, J., Kato, K., Haase, W. and Fried, R., 1989, "Extruded Ceramic - A New Technology for the Comprex® Rotor," SAE Paper 890453.

[37] Guzzella, L., Martin, R., 1998, "The Save Engine Concept," MTZ Report 10, pp. 9-12.

[38] Burri, H., 1958, "Nonsteady Aerodynamics of the Comprex Supercharger," ASME Paper 58-GTP-15.

[39] Wunsch, A., 1971, "Fourier-Analysis Used in the Investigation of Noise Generated by Pressure Wave Machines," Brown Boveri Review. No. 4/5/71.

[40] Croes, N., 1977, "The Principle of the Pressure-Wave Machine as Used for Charging Diesel Engines," Proceedings of the 11th International Symposium on Shock Tubes and Waves, pp. 36-55.

[41] Summerauer, I., Spinnler, F., Mayer, A., and Hafner, A., 1978, "A Comparative Study of the Acceleration Performance of a Truck Diesel Engine With Exhaust-Gas Turbocharger and With Pressure-Wave Supercharger Comprex®," The Institution of Mechanical Engineers, Paper C70/78.

[42] Kollbrunner, T. A., 1980, "Comprex Supercharging for Passenger Diesel Car Engines," SAE Paper 800884.

[43] Jenny, E., Zumstein, B., 1982, "Pressure Wave Supercharger of Passenger Car Diesel Engines," The Institution of Mechanical Engineers, Paper C44/82.

[44] Keller, J. J., 1984, "Some Fundamentals of the Supercharger Comprex," Presented at Winter Annual Meeting of the ASME, edited by Sladky, J. F., Jr., Machinery for Direct Fluid-Fluid Energy Exchange, AD-07, pp. 47-54.

[45] Rebling, P., Jaussi, F., 1984, "Field Experience with a Fleet of Test Cars Equipped with Comprex Supercharged Engines," Institution of Mechanical Engineers, Paper C442/84. Also SAE Paper 841308.

[46] Schneider, G., 1986, "Comprex® Pressure Wave Supercharger in An Opel Senator with 2.3 Liter Diesel Engine," Brown Boveri Review, **73**, No. 10, pp. 563-565.

[47] Zehnder, G., 1971, "Calculating Gas Flow in Pressure-Wave Machines," Brown Boveri Review, No. 4/5/71, 4019 E., pp. 172-176.

[48] Mayer, A., Schruf, G., 1982, "Practical Experience with Pressure Wave Supercharger Comprex on Passenger Cars," The Institution of Mechanical Engineers, Paper C110/82, London.

[49] Zehnder, G., Mayer, A., 1986, "Supercharging with Comprex to Improve the Transient Behavior of Passenger Car Diesel Engines," SAE Paper 860450.

[50] Spinnler, F., Jaussi, F. A., 1986, "The Fully Self-Regulated Pressure Wave Supercharger Comprex for Passenger Car Diesel Engines," The Institution of Mechanical Engineers, Paper C124/86.

[51] Jenny, E., Moser, P., and Hansel, J., 1986, "Progress with Variable Geometry and Comprex," Institution of Mechanical Engineers Conference, Paper C109/86.

[52] Jenny, E., Naguib, M., 1987, "Development of the Comprex Pressure-Wave Supercharger: In the Tradition of Thermal Turbomachinery," Brown Boveri Review, **74**, No. 8, pp. 416-421.

[53] Mayer, A., 1987, "The Comprex Supercharger - A Simple Machine for a Highly Complex Thermodynamic Process," Brown Boveri Review, **74**, No. 8, pp. 422-430.

[54] Zehnder, G., Müller, R., 1987, "Comprex Pressure-Wave Supercharger for Car Diesel Engines," Brown Boveri Review, **74**, No. 8, pp. 431-437.

[55] Mayer, A., 1988, "Comprex-Supercharging Eliminates Trade-off of Performance, Fuel Economy and Emissions," SAE Paper 881152.

[56] Mayer, A., Pauli, E., 1988, "Emissions Concept for Vehicle Diesel Engines Supercharged with Comprex," SAE Paper 880 008.

[57] Mayer, A., 1988, "The Free Running Comprex - A New Concept for Pressure Wave Supercharger," SAE Document PC 55.

[58] Amstutz, A., Pauli, E., and Mayer, A., 1990, "System Optimization with Comprex Supercharging and EGR Control of Diesel Engines," SAE Paper 905097.

[59] Mayer, A., Nashar, I., Perewusnyk, J. 1990, "Comprex with Gas Pocket Control," The Institution of Mechanical Engineers, Paper C405/032, pp. 289-294, London.

[60] Mayer, A., Pauli, E., and Gygax, J., 1990, "Comprex (R) Supercharging and Emissions Reduction in Vehicles Diesel Engines," SAE Paper 900881.

[61] Barry, F. W., 1950, "Introduction to the Comprex," Journal of Applied Mechanics, pp. 47-53.

[62] Lutz, T. W., Scholz, R., 1968, "Supercharging Vehicle Engines by the Comprex System," The Institution of Mechanical Engineers.

[63] Berchtold, M., Lutz, T. W., 1974, "A New Small Power Output Gas Turbine Concept," ASME Paper 74-GT-111.

[64] Berchtold, 1974, "The Comprex Pressure Exchanger: A New Device for Thermodynamic Cycles," JSAE Paper, Tokyo.

[65] Eisele, E., Hiereth, H., and Polz, H., 1975, "Experience with Comprex Pressure Wave Supercharger on the High-Speed Passenger Car Diesel Engine," SAE Paper 750334.

[66] Groenewold, G. M., Welliver, D. R., and Kamo, R., 1977, "Performance and Sociability of Comprex Supercharged Diesel Engine," ASME paper 77-DGP-4.

[67] Schwarzbauer, G. E., 1978, "Turbocharging of Tractor Engines with Exhaust Gas Turbochargers and the BBC-Comprex," The Institution of Mechanical Engineers, Paper C69/78, pp. 161-164.

[68] Walzer, P., Rottenkolber, P., 1982, "Supercharging of Passenger Car Diesel Engines," The Institution of Mechanical Engineers, Paper C117/82, London.

[69] Wallace, F. J., Aldis, C. A., 1982, "Comprex Supercharging Versus Turbocharging of a Large Truck Diesel Engine," The Institution of Mechanical Engineers, Paper C39/82, pp. 89-99, London.

[70] Hong-De, J., 1983, "Two-Dimensional Unsteady Flow in Comprex Rotor," Tokyo International Gas Turbine Congress, Paper 83-Tokyo-IGTC-59.

[71] Zhang, H. S., So, R. M., 1990, "Calculation of the Material Interface in a Pressure-Wave Supercharger," Proceeding of the Institution of Mechanical Engineers, Part A: Journal of Power and Energy, **204**, No. A3, pp 151-161.

[72] Hitomi, M., Yuzuriha, Y., and Tanake, K., 1989, "The Characteristics of Pressure Wave Supercharged Small Diesel Engine," SAE Paper 89054.

[73] Anonymous, 1997, "A Pressure-Wave Machine with Integrated Constant-Volume Combustion," NEFF Funding of Swiss Energy Research 1977-1997, Project No. 426, pp. 142-153.

[74] Nour Eldin, H. A., Oberhem, H., and Schuster, U., 1987, "The Variable Grid-Method for Accurate Animation of Fast Gas Dynamics and Shock-Tube Like Problems," Proceeding of the IMACS/IFAC International Symposium on Modeling and Simulation of Distributed Parameter Systems, pp. 433-440, Japan.

[75] Oberhem, H., Nour Eldin, H. A., 1990, "Fast and Distributed Algorithm for Simulation and Animation of Pressure Wave Machines," Proceeding of the IMACS International Symposium on Mathematical and Intelligent Models in System Simulation, Belgium, pp. 807-815.

[76] Oberhem, H., Nour Eldin, H. A., 1991, "A Variable Grid for Accurate Animation of the Nonstationary Compressible Flow in the Pressure Wave Machine," 7th International Conference on Numerical Methods in Laminar and Turbulent Flow, US.

[77] Nour Eldin, H. A., Oberhem, H., 1993, "Accurate Animation of the thermo-fluidic Performance of the Pressure Wave Machine and its Balanced Material Operation," 8th International Conference on Numerical Methods in Laminar and Turbulent Flow, UK.

[78] Markarious, S. H., Nour Eldin, H. A., and Pu, H., 1995, "Inverse Problem Approach for Unsteady Compressible Fluid-Wave Propagation in the Comprex," 9th International Conference on Numerical Methods in Laminar and Turbulent Flow, US.

[79] Oberhem, H., Nour Eldin, H. A., 1995, "Accurate Animation of the Thermo-Fluidic Performance of the Pressure-Wave Machine and its Balanced Material Operation," International Journal of Numerical Methods of Heat and Fluid Flow, **5**, No. 1, pp. 63-74.

[80] Markarious, S. H., Hachicho, O. H., and Nour Eldin, H. A., 1997, "Wave-Control Modeling in the Pressure-Wave Supercharger (Comprex)," 10th International Conference on Numerical Methods in Laminar and Turbulent Flow, UK.

[81] Piechna, J., 1998, "Comparison of Different Methods of Solution of Euler Equations in Application to Simulation of the Unsteady Processes in Wave Supercharger," The Archive of Mechanical Engineering, **45**, No. 2, pp. 87-106.

[82] Piechna, J., 1998, "Numerical Simulation of the Comprex Type of Supercharger: Comparison of Two Models of Boundary Conditions," The Archive of Mechanical Engineering, **45**, No. 3, pp. 233-250.

[83] Piechna, J., 1998, "Numerical Simulation of the Pressure Wave Supercharger - Effects of Pockets on the Comprex Supercharger Characteristics," The Archive of Mechanical Engineering, **45**, No. 4, pp. 305-323.

[84] Piechna, J., Lisewski, P., 1998, "Numerical Analysis of Unsteady Two-Dimensional Flow Effects in the Comprex Supercharger," The Archive of Mechanical Engineering, **45**, No. 4, pp. 341-351.

[85] Selerowicz, W., Piechna, J., 1999, "Comprex Type Supercharger As a Pressure-Wave Transformer Flow Characteristics," The Archive of Mechanical Engineering, **46**, No. 1, pp. 57-77.

[86] Elloye, K. J., Piechna, J., 1999, "Influence of the Heat Transfer on the Operation of the Pressure Wave Supercharger," The Archive of Mechanical Engineering, **46**, No. 4, pp. 297-309.

[87] Piechna, J., 1999, "A Two-Dimensional Model of the Pressure Wave Supercharger," The Archive of Mechanical Engineering, **46**, No. 4, pp. 331-348.

[88] Piechna, J., 2003, "Autonomous Pressure Wave Compressor Device," 2003 International Gas Turbine Congress, ASME Paper IGTC03-FR-305, Japan.

[89] Oguri, Y., Suzuki, T., Yoshida, M., and Cho, M., 2001, "Research on Adaptation of Pressure Wave Supercharger (PWS) to Gasoline Engine," SAE Paper 2001-01-0368.

[90] Pfiffner, R., Weber, F., Amstutz, A., and Guzzella, L., 1997 "Modeling and Model based Control of Supercharged SI-Engines for Cars with Minimal Fuel Consumption," Proceedings of the American Control Conference, **1**, pp. 304-308.

[91] Weber, F, Guzzella, L., 2000, "Control Oriented Modeling of a Pressure Wave Supercharger," SAE Paper 2000-01-0567.

[92] Weber, F., Spring, P., Guzzella, L., and Onder, C., 2001, "Modeling of a Pressure Wave Supercharged SI Engine Including Dynamic EGR Effects," 3rd International Conference on Control and Diagnostics in Automotive Applications, Italy.

[93] Weber, F, Guzzella, L., and Onder, C., 2002, "Modeling of a Pressure Wave Supercharger Including External Exhaust Gas Recirculation," Proceeding of the Institution of Mechanical Engineers, Part D: Journal of Automobile Engineering, **216**, No. 3, pp 217-235.

[94] Spring, P., Guzzella, L., and Onder, C., 2003, "Optimal Control Strategy for a Pressure-Wave Supercharged SI Engine," 2003 ASME Spring Technical Conference, ASME Paper ICES2003-645, Austria.

[95] Icingür, Y., Hasimoglu, C., and Salman, M. S., 2003, "Effect of Comprex Supercharging on Diesel Emissions," Energy Conversion and Management, **44**, pp. 1745-1753.

[96] Weatherston, R. C., Hertzberg, A., 1967, "The Energy Exchanger, A New Concept for High- Efficiency Gas Turbine Cycles," Journal of Engineering for Power, pp. 217-228.

[97] Hendricks, J. R., 1991, "Wave Rotor Diffusers," M.S. Thesis, Cornell University, Ithaca, New York.

[98] Mathis, G. P., 1991, "Wave Enhanced Gas Turbine Engine Cycles," M.S. Thesis, Cornell University, Ithaca, New York.

[99] Resler, E. L, Moscari, J. C., and, Nalim, M. R., 1993, "Analytic Methods for Design of Wave Cycles for Wave Rotor Core Engines," AIAA Paper 93-2523.

[100] Nalim, M. R., Moscari, J. C., and Resler, E. L., 1993, "Wave Cycle Design for NO_X Limited Wave Rotor Core Engines for High Speed Propulsion," ASME Paper 93-GT-426.

[101] Resler, E. L, Moscari, J. C., and, Nalim, M. R., 1994, "Analytic Design Methods for Wave Cycles," Journal of Propulsion and Power, **10**, No. 5, pp. 683-689.

[102] Mocsari, J. C., 1994, "Design of Wave Rotor Topping Cycles for Propulsion and Shaftpower," M.S. Thesis, Cornell University, Ithaca, New York.

[103] Nalim, M. R., 1994 "Wave Cycle Design for Wave Rotor Engines with Limited Nitrogen-Oxide Emissions," Ph.D. Thesis, Cornell University, Ithaca, New York.

[104] Nalim, M. R., Resler, E. L., 1995, "Wave Cycle Design for Wave Rotor Gas Turbine Engines with Low NO_X Emissions," ASME Paper 95-GT-245.

[105] Nalim, M. R., Resler, E. L., 1996, "Wave Cycle Design for Wave Rotor Gas Turbine Engines with Low NO_X Emissions," ASME Journal of Engineering for Gas Turbines and Power, **118**, pp. 474-480.

[106] Resler, E. L., 2001, "Shock Wave Propulsion," International Journal of Chemical Kinetics, **33**, pp. 846-852.

[107] Müller, M. A., 1954, German Patents 916607 and 924845.

[108] Foa, J. V., 1960, *Elements of Flight Propulsion*, John Wiley and Sons, New York.

[109] Taussig, R. T., 1984, "Wave Rotor Turbofan Engines for Aircraft," Winter Annual Meeting of the ASME, edited by Sladky, J. F., Machinery for Direct Fluid-Fluid Energy Exchange, AD-07, pp. 9-45.

[110] Kentfield, J. A. C., 1985, "The Pressure Exchanger, An Introduction Including a Review of the Work of Power Jets (R & D) Ltd.," Proceeding ONR/NAVAIR Wave Rotor Research and Technology Workshop, Report NPS-67-85-008, pp. 9-49, Naval Postgraduate School, Monterey, CA.

[111] Jendrassik, G., 1956, "Jet Reaction Propulsion Units Utilizing a Pressure Exchanger," US Patent 2757509.

[112] Jendrassik, G., 1960, "Pressure Exchangers and Applications Thereof," US Patent 2946184.

[113] Spalding, D. B., 1985, "Remarks on the Applicability of Computational Fluid Dynamics to Wave Rotor Technology," Proceeding ONR/NAVAIR Wave Rotor Research and Technology Workshop, Report NPS-67-85-008, pp. 403-49, Naval Postgraduate School, Monterey, CA.

[114] Jonsson, V. K., Matthews, L., and Spalding, D. B., 1973, "Numerical Solution Procedure for Calculating the Unsteady, One-Dimensional Flow of Compressible Fluid," ASME Paper 73-FE-30.

[115] Matthews, L., 1969, "An Algorithm for Unsteady Compressible One-Dimensional Fluid Flow," M.S. Thesis, University of London.

[116] Azim, A., 1974, "An Investigation Into the Performance and Design of Pressure Exchangers," Ph.D. Thesis, University of London.

[117] Azoury, P. H., Hai, S. M., 1975, "Computerized Analysis of Dynamic Pressure Exchanger Scavenge Processes," Proceedings of the Institution of Mechanical Engineers, **189**, pp. 149-158.

[118] Azoury, P. H., 1960, "The Dynamic Pressure Exchanger-Gas Flow in a Model Cell," Ph.D. Thesis, University of London.

[119] Kentfield, J. A. C., 1963, "An Examination of the Performance of Pressure Exchanger Equalizers and Dividers," Ph.D. Thesis, University of London.

[120] Kentfield, J. A. C., 1968, "An Approximation Method for Predicting the Performance of Pressure Exchangers," ASME Paper 68-WA-FE-37

[121] Kentfield, J. A. C., 1969, "The Performance of Pressure-Exchanger Dividers and Equalizers," Journal of Basic Engineering, **91**, No. 3, pp. 361-370.

[122] Kentfield, J. A. C., Barnes, J. A., 1976, "The Pressure Divider: A Device for Reducing Gas-Pipe-Line Pumping-Energy Requirements," Proceeding of 11th Intersociety Energy Conversion Engineering Conference, pp. 636-643.

[123] Kentfield, J. A. C., 1998, "Circumferential Cell-Dividers in Wave Rotors," AIAA Paper 98-3397.

[124] Pearson, R. D., 1983, "A Pressure Exchange Engine for Burning Pyroil as the End User in a Cheap Power from Biomass System," 15ht International Congress of Combustion Engines, Paris.

[125] Pearson, R. D., 1985, "A Gas Wave-Turbine Engine Which Developed 35 HP and Performed Over a 6:1 Speed Range," Proceeding ONR/NAVAIR Wave Rotor Research and Technology Workshop, Report NPS-67-85-008, pp. 403-49, Naval Postgraduate School, Monterey, CA.

[126] Mathur, A., 1985, "A Brief Review of the GE Wave Engine Program (1958-1963)," Proceeding ONR/NAVAIR Wave Rotor Research and Technology Workshop, Report NPS-67-85-008, pp. 171-193, Naval Postgraduate School, Monterey, CA.

[127] Shreeve, R., Mathur, A., Eidelman, S., and Erwin, J., 1982, "Wave Rotor Technology Status and Research Progress Report," Report NPS-67-82-014PR, Naval Post-Graduate School, Monterey, CA.

[128] Coleman, R. R., 1984, "Wave Engine Technology Development," Final report prepared by General Power Corporation for AFWAL, Contract No. AFWAL -TR-83-2095.

[129] Coleman, R. R., 1994, "Cycle for a Three-Stage Ultrahigh Pressure Ratio Wave Turbine Engine," AIAA Paper 94-2725.

[130] Moritz, R., 1985, "Rolls-Royce Study of Wave Rotors (1965-1970)," Proceeding ONR/NAVAIR Wave Rotor Research and Technology Workshop, Report NPS-67-85-008, pp. 116-124, Naval Postgraduate School, Monterey, CA.

[131] Berchtold, M., 1985, "The Comprex as a Topping Spool in a Gas Turbine Engine for Cruise Missile Propulsion" Proceeding ONR/NAVAIR Wave Rotor Research and Technology Workshop, Report NPS-67-85-008, pp. 284-290, Naval Postgraduate School, Monterey, CA.

[132] Zumdiek, J. F., Thayer, W. J., Cassady, P. E., Taussig, R. T., Christiansen, W. H., and Hertzberg, A., 1979, "The Energy Exchanger in Advanced Power Cycle Systems," Proceeding of the 14th Intersociety Energy Conversion Engineering Conference, Boston.

[133] Thayer, W. J., Taussig, R. T., 1982 "Erosion Resistance and Efficiency of Energy Exchangers," ASME Paper 82-GT-191.

[134] Zumdiek, J. F., Vaidyanathan, T. S., Klosterman, E. L., Taussig, R. T., Cassady, P. E., Thayer, W. J., and Christiansen, W. H., 1979 "The Fluid Dynamic Aspects of an Efficient Point Design Energy Exchanger," Proceeding of the 12th International Symposium on Shock Tubes and Waves, Jerusalem.

[135] Thayer, W. J., Vaidyanathan, T. S., and Zumdiek, J. F. 1980, "Measurements and Modeling of Energy Exchanger Flow," Proceeding of the 14th Intersociety Energy Conversion Engineering Conference, Seattle.

[136] Thayer, W. J., Zumdiek, J. F. 1981 "A Comparison of Measured and Computed Energy Exchanger Performance," Proceeding of the 13th International Symposium on Shock Tubes and Waves, Niagara Falls.

[137] Thayer, W. J., 1985, "The MSNW Energy Exchanger Research Program," Proceeding ONR/NAVAIR Wave Rotor Research and Technology Workshop, Report NPS-67-85-008, pp. 85-116, Naval Postgraduate School, Monterey, CA.

[138] Taussig, R. T., 1984, "Wave Rotor Turbofan Engines for Aircraft," Mechanical Engineering, **106**, No. 11, pp. 60-68.

[139] Mathur, A., 1985, "Design and Experimental Verification of Wave Rotor Cycles," Proceeding ONR/NAVAIR Wave Rotor Research and Technology Workshop, Report NPS-67-85-008, pp. 215-228, Naval Postgraduate School, Monterey, CA.

[140] Eidelman, S., Mathur, A., Shreeve, R. P. and Erwin, J., 1984, "Application of Riemann Problem Solvers to Wave Machine Design," AIAA Journal, **22**, No. 7, pp. 1010-1012.

[141] Eidelman, S., 1984, "The Problem of Gradual Opening in Wave Rotor Passages," 19th Intersociety Energy Conversion Engineering San Francisco, California.

[142] Eidelman, S., 1986, "Gradual Opening of Rectangular and Skewed Wave Rotor Passages," Proceeding ONR/NAVAIR Wave Rotor Research and Technology Workshop, Report NPS-67-85-008, pp. 229-2249, Naval Postgraduate School, Monterey, CA.

[143] Eidelman, S., 1985, "The Problem of Gradual Opening in Wave Rotor Passages," Journal of Propulsion and Power, **1**, No. 1, pp. 22-28.

[144] Mathur, A., Shreeve, R. P., and Eidelman, S., "Numerical Techniques for Wave Rotor Cycle Analysis," American Society of Mechanical Engineers, Fluids Engineering Division (Publication) FED , **15**, 1984. Presented at the 1984 Winter Annual Meeting of the American Society of Mechanical Engineers, US.

[145] Eidelman, S., 1986, "Gradual Opening of Skewed Passages in Wave Rotors," Journal of Propulsion and Power, **2**, No. 4, pp. 379-381.

[146] Mathur, A., 1985, "Wave Rotor Research: A Computer Code for Preliminary Design of Wave Diagrams," Report NPS67-85-006CR, Naval Postgraduate School, Monterey, CA..

[147] Mathur, A., Shreeve, R. P., 1987, "Calculation of Unsteady Flow Processes in Wave Rotors," AIAA Paper 87-0011.

[148] Mathur, A., 1986, "Code Development for Turbofan Engine Cycle Performance With and Without a Wave Rotor Component," Report NPS67-86-006CR, Naval Postgraduate School, Monterey, CA.

[149] Mathur, A., 1986, "Estimation of Turbofan Engine Cycle Performance With and Without a Wave Rotor Component," Report NPS67-86-008CR, Naval Postgraduate School, Monterey, CA.

[150] Roberts, J. W., 1990, "Further Calculations of the Performance of Turbofan Engines Incorporating a Wave Rotor," M.S. Thesis, Naval Postgraduate School, CA.

[151] Salacka, T. F., 1985, "Review, Implementation and Test of the QAZID Computational Meth od with a View to Wave Rotor Applications," M.S. Thesis, Naval Postgraduate School, CA.

[152] Johnston, D. T., 1987, "Further Development of a One-Dimensional Unsteady Euler Code for Wave Rotor Applications," M.S. Thesis, Naval Postgraduate School, CA.

[153] Shreeve, R. P., Mathur, A., 1985, Proceeding ONR/NAVAIR Wave Rotor Research and Technology Workshop, Report NPS-67-85-008, Naval Postgraduate School, Monterey, CA.

[154] Wilson, J., Paxson, D. E., 1993, "Jet Engine Performance Enhancement Through Use of a Wave-Rotor Topping Cycle," NASA TM-4486.

[155] Paxson, D. E., 1992, "A General Numerical Model for Wave-Rotor Analysis," NASA TM-105740.

[156] Paxson, D. E., 1993, "An Improved Numerical Model for Wave Rotor Design and Analysis," AIAA Paper 93-0482. Also NASA TM-105915.

[157] Paxson, D. E., 1993, "A Comparison Between Numerically Modeled and Experimentally Measured Loss Mechanisms in Wave Rotors," AIAA Paper 93-2522.

[158] Paxson, D. E., 1995, "Comparison Between Numerically Modeled and Experimentally Measured Wave-Rotor Loss Mechanism," Journal of Propulsion and Power, **11**, No. 5, pp. 908-914. Also NASA TM-106279.

[159] Wilson J., Fronek, D., 1993, "Initial Results from the NASA-Lewis Wave Rotor Experiment," AIAA Paper 93-2521. Also NASA TM-106148.

[160] Wilson, J., 1997, "An Experiment on Losses in a Three Port Wave-Rotor," NASA CR-198508.

[161] Wilson, J., 1998, "An Experimental Determination of Loses in a Three-Port Wave Rotor," Journal of Engineering for Gas Turbines and Power, **120**, pp. 833-842. Also ASME Paper 96- GT-117, and NASA CR-198456.

[162] Welch, G. E., Chima, R. V., 1993, "Two-Dimensional CFD Modeling of Wave Rotor Flow Dynamics," AIAA-93-3318. Also NASA TM-106261.

[163] Welch, G. E., 1993, "Two-Dimensional Numerical Study of Wave-Rotor Flow Dynamics," AIAA Paper 93-2525.

[164] Welch, G. E., 1997, "Two-Dimensional Computational Model for Wave Rotor Flow Dynamics," Journal Engineering for Gas Turbines and Power, **119**, No. 4, pp. 978-985. Also ASME Paper 96-GT-550, and NASA TM-107192.

[165] Larosiliere, L. M., 1993, "Three-Dimensional Numerical Simulation of Gradual Opening in a Wave-Rotor Passage," AIAA Paper 93-2526. Also NASA CR-191157.

[166] Larosiliere, L. M., 1995, "Wave Rotor Charging Process: Effects of Gradual Opening and Rotation," Journal of Propulsion and Power, **11**, No. 1, pp. 178-184.

[167] Larosiliere, L. M., Mawid, M., 1995, "Analysis of Unsteady Wave Processes in a Rotating Channel," International Journal of Numerical Methods in Fluids, **21**, pp. 467-488. Also AIAA Paper 93-2527, and NASA CR-191154.

[168] Welch, G. E., 1997, "Macroscopic Balance Model for Wave Rotors," Journal of Propulsion and Power, **13**, No. 4, pp. 508-516. Also AIAA Paper 96-0243.

[169] Welch, G. E., Larosiliere, L. M., 1997, "Passage-Averaged Description of Wave Rotor Flow," AIAA Paper 97-3144. Also NASA TM-107518.

[170] Paxson, D. E., 1998, "An Incidence Loss Model for Wave Rotors with Axially Aligned Passages," AIAA Paper 98-3251. Also NASA TM-207923.

[171] Paxson D. E., Wilson, J., 1995, "Recent Improvements to and Validation of the One Dimensional NASA Wave Rotor Model," NASA TM-106913.

[172] Paxson, D. E., 1995, "A Numerical Model for Dynamic Wave Rotor Analysis," AIAA Paper 95-2800. Also NASA TM-106997.

[173] Paxson, D. E., 1996, "Numerical Simulation of Dynamic Wave Rotor Performance," Journal of Propulsion and Power, **12**, No. 5, pp. 949-957.

[174] Paxson, D. E., Lindau, J. W., 1997, "Numerical Assessment of Four-Port Through-Flow Wave Rotor Cycles with Passage Height Variation," AIAA Paper 97-3142. Also NASA TM-107490.

[175] Paxson, D. E., 1997, "A Numerical Investigation of the Startup Transient in a Wave Rotor," Journal of Engineering for Gas Turbines and Power, **119**, No. 3, pp. 676-682. Also ASME Paper 96-GT-115, and NASA TM 107196.

[176] Wilson, J., Paxson, D. E., 1996, "Wave Rotor Optimization for Gas Turbine Topping Cycles," Journal of Propulsion and Power, **12**, No. 4, pp. 778-785. Also SAE Paper 951411, and NASA TM-106951.

[177] Wilson, J., 1997, "Design of the NASA Lewis 4-Port Wave Rotor Experiment," AIAA Paper 97-3139. Also NASA CR-202351.

[178] Paxson, D. E., Nalim, M. R., 1999, "Modified Through-Flow Wave-Rotor Cycle with Combustor Bypass Ducts," Journal of Propulsion and Power, **15**, No. 3, pp. 462-467. Also AIAA Paper 97-3140, and NASA TM-206971.

[179] Nalim, M. R., Paxson, D. E., 1999, "Method and Apparatus for Cold-Gas Reinjection in Through-Flow and Reverse-Flow Wave Rotors," US Patent 5894719.

[180] Welch, G. E., Jones, S. M. and Paxson, D. E., 1997, "Wave Rotor-Enhanced Gas Turbine Engines," Journal of Engineering for Gas Turbines and Power, **119**, No. 2, pp. 469-477.

[181] Welch, G. E., 1997, "Wave Engine Topping Cycle Assessment," AIAA Paper 97-0707. Also NASA TM-107371.

[182] Welch, G. E., Paxson, D. E., 1998, "Wave Turbine Analysis Tool Development," AIAA Paper 98-3402. Also NASA TM-208485.

[183] Nalim, M. R., 1995, "Preliminary Assessment of Combustion Modes for Internal Combustion Wave Rotors," AIAA Paper 95-2801. Also NASA-TM 107000.

[184] Nalim, R. M., Paxson, D. E., 1997, "A Numerical Investigation of Premixed Combustion in Wave Rotors," Journal of Engineering for Gas Turbines and Power, **119**, No. 3, pp. 668-675. Also ASME Paper 96-GT-116, and NASA TM-107242.

[185] Nalim, M. R., 1997, "Numerical Study of Stratified Charge Combustion in Wave Rotors," AIAA Paper 97-3141. Also NASA TM-107513.

[186] Hendricks, R. C., Wilson, J., Wu, T., and Flower, R., 1997, "Bidirectional Brush Seals," ASME Paper 97-GT-256. Also NASA TM-107351.

[187] Hendricks, R. C., Wilson, J., Wu, T., Flower, R., and Mullen, R. L., 1997, "Bidirectional Brush Seals – Post-Test Analysis," NASA TM-107501.

[188] Hendricks, R. C., Wilson, J., Wu, T., and Flower, R., 1998, "Two-Way Brush Seals Catch a Wave," Journal of Mechanical Engineering, **120**, No. 11, pp. 78-80.

[189] Snyder, P. H., 1996, "Wave Rotor Demonstrator Engine Assessment," NASA CR-198496.

[190] Snyder, P. H., Fish, R. E., 1996, "Assessment of a Wave Rotor Topped Demonstrator Gas Turbine Engine Concept," ASME Paper 96-GT-41.

[191] Gegg, S., Snyder, P., 1998, "Aerodynamic Design of a Wave Rotor to High Pressure Turbine Transition Duct," AIAA Paper 98-3249.

[192] Weber, K., Snyder, P., 1998, "Wave Rotor to Turbine Transition Duct Flow Analysis," AIAA Paper 98-3250.

[193] Snyder, P. H., 2002, "Pulse Detonation Engine Wave Rotor," US Patent 6449939.

[194] Smith, C. F., Snyder, P. H., Emmerson, C. W., and Nalim, M. R., 2002, "Impact of the Constant Volume Combustor on a Supersonic Turbofan Engine," AIAA Paper 2002-3916.

[195] Lear, W. E., Candler, G., 1993, "Direct Boundary Value Solution of Wave Rotor Flow Fields," AIAA Paper 93-0483.

[196] Lear, W. E., Kielb, R. P., 1996, "The Effect of Blade Angle Design Selection on Wave-Turbine Engine Performance," ASME Paper 96-GT-259.

[197] Hoxie, S. S., Lear, W. E., and Micklow, G. J., 1998, "A CFD Study of Wave Rotor Losses Due to the Gradual Opening of Rotor Passage Inlets," AIAA Paper 98-3253.

[198] Fatsis, A., Ribaud, Y., 1997, "Numerical Analysis of the Unsteady Flow Inside Wave Rotors Applied to Air Breathing Engines," 13th International Symposium on Airbreathing Engines, Paper ISABE-97-7214.

[199] Fatsis, A., Ribaud, Y., 1999, "Thermodynamic Analysis of Gas Turbines Topped with Wave Rotors," Aerospace Science and Technology, **3**, No. 5, pp. 293-299.

[200] Jones, S. M., Welch, G. E., 1996, "Performance Benefits for Wave Rotor-Topped Gas Turbine Engines," ASME Paper 96-GT-075.

[201] Fatsis, A., Ribaud, Y., 1998, "Preliminary Analysis of the Flow Inside a Three-Port Wave Rotor by Means of a Numerical Model," Aerospace Science and Technology, **2**, No. 5, pp. 289-300.

[202] Nalim, M. R., 2000, "Longitudinally Stratified Combustion in Wave Rotors," Journal of Propulsion and Power, **16**, No. 6, pp. 1060-1068.

[203] Nalim, M. R., 2003, "Partitioned Multi-Channel Combustor," US Patent 6526936.

[204] Pekkan, K., Nalim, M. R., 2003, "Two-Dimensional Flow and NO_X Emissions In Deflagrative Internal Combustion Wave Rotor Configurations," ASME Journal of Engineering for Gas Turbines and Power, **125**, pp. 720-733. Also ASME Paper 2002-GT-30085.

[205] Pekkan, K., Nalim, M. R., 2002 "Control of Fuel and Hot-Gas Leakage in a Stratified Internal Combustion Wave Rotor," AIAA Paper 2002-4067.

[206] Pekkan, K., Nalim, M. R., 2002, "On Alternative Models for Internal Combustor Wave Rotor Simulation," Proceeding of 2002 Technical Meeting of the Central State Section of the Combustion Institute, Knoxville.

[207] Nalim, M. R., Jules, K., 1998, "Pulse Combustion and Wave Rotors for High-Speed Propulsion Engines," AIAA Paper 98-1614.

[208] Nalim, M. R., 2002, "Wave Rotor Detonation Engine," US Patent 6460342.

[209] Kailasanath, K., 2003, "Recent Developments in the Research on Pulse Detonation Engines," AIAA Journal, **14**, No. 2, pp. 145-159.

[210] Izzy, Z., Nalim, M. R., 2001, "Rotary Ejector Enhanced Pulsed Detonation System," AIAA Paper 2001-3613.

[211] Snyder, P., Alparslan, B., and Nalim, M. R., 2002, "Gas Dynamic Analysis of the Constant Volume Combustor, A Novel Detonation Cycle," AIAA paper 2002-4069.

[212] Snyder, P., Alparslan, B., and Nalim, M. R., 2002, "Wave Rotor Combustor Test Rig Preliminary Design," 2004 International Mechanical Engineering Conference, ASME Paper IMECE2004- 61795.

[213] Okamoto, K., Nagashima, T., 2003, "A Simple Numerical Approach of Micro Wave Rotor Gasdynamic Design," 16th International Symposium on Airbreathing Engines, Paper ISABE-2003-1213.

[214] Okamoto, K., Nagashima, T., and Yamaguchi, K., 2001, "Rotor-Wall Clearance Effects upon Wave Rotor Passage Flow," 15th International Symposium on Airbreathing Engines, Paper ISABE-2001-1222.

[215] Okamoto, K., Nagashima, T., and Yamaguchi, K., 2003, "Introductory Investigation of Micro Wave Rotor," 2003 International Gas Turbine Congress, ASME Paper IGTC03-FR-302, Japan.

[216] Anderson, J. D., 2002, *Modern Compressible Flow: With Historical Perspective*, 3rd edition, New York: McGraw-Hill.

[217] Benini, E., Toffolo, A., and Lazzaretto, A., 2003, "Centrifugal Compressor of A 100 KW Microturbine: Part 1– Experimental and Numerical Investigations on Overall Performance," ASME Paper GT2003-38152.

[218] Rogers, C., 2003, "Some Effects of Size on the Performance of Small Gas Turbine," ASME Paper GT2003-38027.

[219] Shi, J., Venkata, R., Vedula, J. H., Connie, E.B., Scott, S. O., Bertuccioli, L., and Bombara, D. J., 2002, "Preliminary Design of Ceramic Components for the ST5+ Advanced Microturbine Engine," ASME Paper GT-2002-30547.

[220] Walsh, C., An, C., Kapat, J. S., and Chow, L. C., 2002, "Feasibility of a High-Temperature Polymer-Derived-Ceramic Turbine Fabricated Through Micro-Stereolithography," ASME Paper GT-2002-30548.

[221] Craig, P., 1997, "The Capstone Turbogenerator as an Alternative Power Source," SAE Paper 970292, 1997.

[222] Kang, Y., and McKeirnan, R., 2003, "Annular Recuperator Development and Performance Test for 200kW Microturbine," ASME Paper GT-2003-38522.

[223] McDonald, C. F., 1996, "Heat Recovery Exchanger Technology for Very Small Gas Turbine," Journal of Turbo and Jet Engines, **13**, pp. 239-261.

[224] Proeschel, R. A., 2002, "Proe 90TM Recuperator for Microturbine Applications," ASME Paper GT-2002-30406.

[225] Carman, B. G., Kapat, J. S., Chow, L. C., and An, L., 2002, "Impact of a Ceramic Microchannel Heat Exchanger on a Microturbine," ASME Paper GT2002-30544.

[226] Treece, B., Vessa, P., and McKeirnan, R., 2002, "Microturbine Recuperator Manufacturing and Operating Experience," ASME Paper GT2002-30404.

[227] McDonald, C. F., 2000, "Low Cost Recuperator Concept for Microturbine Applications," ASME Paper GT2000-167.

[228] Utriainen, E., Sunden, B., 2001, "A Comparison of Some Heat Transfer Surfaces for Small Gas Turbine Recuperators," ASME Paper GT2001-0474.

[229] Maziasz, P. J., Pint, B. A., Swindeman, R. W., More, K. L., and Lara-Curzio, E., 2003, "Selection, Development and Testing of Stainless Steel and Alloys for High-Temperature Recuperator Applications," ASME Paper GT2003-38762.

[230] Akbari, P., Müller, N., 2003, "Performance Improvement of Small Gas Turbines Through Use of Wave Rotor Topping Cycles," 2003 International ASME/IGTI Turbo Exposition, ASME Paper GT2003-38772.

[231] El Hadik, A. A., 1990, "The Impact of Atmospheric Conditions on Gas Turbine Performance," Journal of Engineering for Gas Turbines and Power, **112**, No. 4, pp. 590-595.

[232] Akbari, P., Müller, N., and Nalim, M. R., 2004, "Performance Improvement of Recuperated and Unrecuperated Microturbines Using Wave Rotor Machines," 2004 ASME-ICED Spring Technical Conference, Japan.

[233] Mattingly, J. D., 1996, *Elements of Gas Turbine Propulsion*, McGraw-Hill, International Editions.

[234] Akbari P., Müller, N., 2003, "Performance Investigation of Small Gas Turbine Engines Topped with Wave Rotors," AIAA-Paper 2003-4414.

[235] Akbari, P., Müller, N., 2003, "Preliminary Design Procedure for Gas Turbine Topping Reverse-Flow Wave Rotors," 2003 International Gas Turbine Congress, ASME Paper IGTC03-FR-301. Japan.

[236] Akbari, P., Müller, N., 2003, "Gas Dynamic Design Analyses of Charging Zone for Reverse-Flow Pressure Wave Superchargers," 2003 ASME Spring Technical Conference, ASME Paper ICES2003-690.

[237] Podhorelsky L., Macek J., Polasek M., and Vitek O., 2004, "Simulation of a Comprex Pressure Exchanger in 1-D Code," SAE Paper 2004-01-1000.

[238] Frąckowiak, M., Iancu, F., Potrzebowski, A., Akbari, P., Müller, N., and Piechna, J., 2004, "Numerical Simulation of Unsteady-Flow Processes in Wave Rotors," 2004 International Mechanical Engineering Conference, ASME Paper IMECE2004- 60973.

[239] Piechna, J., Akbari, P., Iancu, F., and Müller, N., 2004, "Radial-Flow Wave Rotor Concepts, Unconventional Designs and Applications," 2004 International Mechanical Engineering Conference, ASME Paper IMECE2004-59022.

[240] Akbari, P., Kharazi, A. A., and Müller, N., 2003, "Utilizing Wave Rotor Technology to Enhance the Turbo Compression in Power and Refrigeration Cycles," 2003 International Mechanical Engineering Conference, ASME Paper IMECE2003-44222.

[241] Saury, D., Harmand, S., and Siroux, M, 2001, "Experimental Study of Flash Evaporation of Water Film," International Journal of Heat and Mass Transfer, No. 45, pp. 3447-3457.

[242] Miyatake, O., Murakami, K., and Kawata, Y., 1973, "Fundamental Experiments with Flash Evaporation," Heat Transfer Jpn., Res. 2, pp. 89-100.

[243] Kharazi, A. A., Akbari, P., and Müller, N., 2004, "An Application of Wave Rotor Technology for Performance Enhancement of R718 Refrigeration Cycles," AIAA Paper 2004-5636.

[244] Kharazi, A. A., Akbari, P., and Müller, N., 2004, "Performance Benefits of R718 Turbo-Compression Cycles Using a 3-Port Condensing Wave Rotors," 2004 International Mechanical Engineering Conference, ASME Paper IMECE2004- 60992.

[245] Kharazi, A. A., Akbari, P., and Müller, N., 2004, "Preliminary Study of a Novel R718 Turbo-Compression Cycle Using a 3-Port Condensing Wave Rotor," 2004 International ASME Turbo Exposition, ASME Paper GT2004-53622, Austria.

[246] Müller, N., Fréchette, L. G., 2002, "Performance Analysis of Brayton and Rankine Cycle Microsystems for Portable Power Generation," ASME Paper IMECE2002-39628..

[247] Iancu, F., Akbari, P., and Müller, N., 2004, "Feasibility Study of Integrating Four-Port Wave Rotors into Ultra-Micro Gas Turbines," AIAA Paper 2004-3581.

[248] Epstein, A. H., Senturia, et al, 1997, "Power MEMS and Microengines," IEEE Transducers Conference.

APPENDICES

Appendix A: Shock Waves and Diffusers

In order to obtain the plots shown in Figure 1 and Figure 2, it is first necessary to find relations between pressure gain and Mach number changes of upstream and downstream flow across a moving shock wave and a diffuser.

A.1: Moving Shock Wave

According to the top part of Figure 36, for a moving shock wave propagating in a frictionless channel, the flow upstream and downstream Mach numbers are respectively defined as:

$$M_1 = \frac{u_1}{a_1} \ , \ M_2 = \frac{u_2}{a_2} \tag{125}$$

The goal here is to find an equation relating the pressure gain across the shock wave (Π_S) to the Mach numbers introduced in Eq. (125). To do so, it is necessary to transfer the non-steady frame of reference to a stationary coordinate as shown in the bottom part of Figure 36. In such a stationary frame of reference, the flow upstream and downstream Mach numbers now are defined respectively as:

$$M_{1-s} = \frac{w_S + u_1}{a_1} \ , \ M_{2-s} = \frac{w_S + u_2}{a_2} \tag{126}$$

The governing normal-shock equations for a stationary shock wave results in:

$$M_{2-s}{}^2 = \frac{(\gamma - 1)M_{1-s}{}^2 + 2}{2\gamma M_{1-s}{}^2 - (\gamma - 1)} \tag{127}$$

Now the task is to find relations for $M_{1\text{-}s}$ and $M_{2\text{-}s}$ relating them to Π_S , M_1 , and M_2 and substitute all of them in Eq. (127). As shown in Eq. (11), the definition of the shock Mach number (M_S) becomes the same as $M_{1\text{-}s}$, therefore:

$$M_{1-s} = M_S = \sqrt{\frac{\gamma+1}{2\gamma}(\Pi_S - 1)+1} \tag{128}$$

To find a relation between M_{2-s} and Π_S:

$$M_{2-s} = \frac{w_S}{a_2} + \frac{u_2}{a_2} = \frac{w_S + u_1 - u_1}{a_2} + \frac{u_2}{a_2} = \frac{w_S + u_1}{a_2} - \frac{u_1}{a_2} + \frac{u_2}{a_2} = \left(\frac{w_S + u_1}{a_1} - \frac{u_1}{a_1}\right)\frac{a_1}{a_2} + \frac{u_2}{a_2} \tag{129}$$

or,

$$M_{2-s} = (M_S - M_1)\sqrt{\frac{T_1}{T_2}} + M_2 \tag{130}$$

Substituting Eq. (128) and (130) into (127) yields:

$$\left[\left[\sqrt{\frac{\gamma+1}{2\gamma}(\Pi_S - 1)+1} - M_1\right]\sqrt{\frac{T_1}{T_2}} + M_2\right]^2 = \frac{(\gamma-1)\left[\frac{\gamma+1}{2\gamma}(\Pi_S - 1)+1\right]+2}{2\gamma\left[\frac{\gamma+1}{2\gamma}(\Pi_S - 1)+1\right]-(\gamma-1)} \tag{131}$$

where T_2/T_1 is a function of the local pressure ratio as well, calculated by Eq. (5). Therefore, this equation calculates Π_S as a function of M_1 and M_2 as illustrated in Figure 1 for $\gamma = 1.4$.

To calculate the shock wave efficiency (η_{Shock}) as a function of the local pressure ratio, first the definition of the shock wave isentropic efficiency is considered. It is defined as the ratio of the isentropic enthalpy change to the actual enthalpy change:

$$\eta_{Shock} = \frac{(\Delta h)_{isentropic}}{(\Delta h)_{actual}} \tag{132}$$

Treating the flow as a perfect gas, for which $h = C_p T$ and C_p is constant:

$$\eta_{Shock} = \frac{(\Delta T)_{isentropic}}{(\Delta T)_{actual}} = \frac{(T_{2,s}/T_1) - 1}{(T_2/T_1) - 1} \tag{133}$$

Using the isentropic relation for $T_{2,s}/T_1$ and substituting Eq. (5) for T_2/T_1 assuming a frictionless channel yields:

$$\eta_{Shock} = \frac{\Pi_s^{\gamma-1/\gamma} - 1}{\Pi_s \left(\frac{\frac{\gamma+1}{\gamma-1} + \Pi_s}{1 + \frac{\gamma+1}{\gamma-1}\Pi_s} \right) - 1} \tag{134}$$

Figure 2 illustrates the variation of η_{Shock} as a function of the local pressure ratio for γ =1.4.

A.2: Diffuser

The diffuser isentropic efficiency known as the diffuser effectiveness is defined similar to that of a shock wave:

$$\eta_{Diffuser} = \frac{(\Delta h)_{isentropic}}{(\Delta h)_{actual}} = \frac{(\Delta T)_{isentropic}}{(\Delta T)_{actual}} = \frac{(T_{2,s}/T_1) - 1}{(T_2/T_1) - 1} \tag{135}$$

Because the total temperature remains constant across the diffuser (T_{t1}=T_{t2}), the diffuser isentropic efficiency can be expressed based on the static pressure ratio across the diffuser (p_2/p_1) and the ratio of the total pressure (p_{t2}/p_{t1}) that represents the pressure loss across the diffusers:

$$\eta_{Diffuser} = \frac{\left(\frac{p_2}{p_1}\right)^{\gamma-1/\gamma} - 1}{\left(\frac{p_{t1}}{p_{t2}}\frac{p_2}{p_1}\right)^{\gamma-1/\gamma} - 1} \tag{136}$$

The variation of $\eta_{Diffuser}$ as a function of the static pressure ratio across the diffuser, p_2/p_1, for certain losses of total pressure across the diffuser expressed by the ratio, p_{t2}/p_{t1}, is shown in Figure 2 and compared with the shock wave isentropic efficiency η_{Shock}.

Now, to obtain a relation between the pressure gain and changes of inlet and outlet Mach number, the following procedure is pursued:

The following equations relate the ratio of the total pressure to static pressure of the flow in the inlet and outlet, respectively:

$$\frac{p_{t1}}{p_1} = \left(1 + \frac{\gamma - 1}{2} M_1^2\right)^{\gamma/\gamma-1} \tag{137}$$

and,

$$\frac{p_{t2}}{p_2} = \left(1 + \frac{\gamma - 1}{2} M_2^2\right)^{\gamma/\gamma-1} \tag{138}$$

Dividing these two equations gives:

$$\frac{p_{t1}}{p_{t2}} \frac{p_2}{p_1} = \left(\frac{1 + \frac{\gamma - 1}{2} M_1^2}{1 + \frac{\gamma - 1}{2} M_2^2}\right)^{\gamma/\gamma-1} \tag{139}$$

By substituting this equation in Eq. (136):

$$\eta_{Diffuser} = \frac{\left(\frac{p_2}{p_1}\right)^{\gamma-1/\gamma} - 1}{\left(\frac{1 + \frac{\gamma - 1}{2} M_1^2}{1 + \frac{\gamma - 1}{2} M_2^2}\right) - 1} \tag{140}$$

or,

$$\frac{p_2}{p_1} = \left[1 + \eta_{Diffuser}\left(\frac{1 + \frac{\gamma - 1}{2} M_1^2}{1 + \frac{\gamma - 1}{2} M_2^2}\right)\right]^{\gamma/\gamma-1} \tag{141}$$

Using this equation and Eq. (131), Figure 1 therefore compares the variation of pressure gain between a moving shock wave (solid) and a 100% efficient ($\eta_{Diffuser}=1$) diffuser (dotted) as a function of the incoming flow Mach number, M_1, for two different values of M_2 assuming $\gamma=1.4$.

Appendix B: Temperature-Entropy Diagram Construction

The temperature-entropy (T-S) diagrams serve as valuable tools for visualizing the second law aspects of processes and cycles. They are frequently used in performance demonstration of gas turbine cycles. The performance enhancement of a gas turbine topped by a four-port wave rotor can be easily observed by comparing the T-S diagrams of the baseline and topped engines. Here is shown the calculations necessary to draw T-S diagrams for a four-port wave rotor topped cycle and the corresponding baseline engine.

B1: Compressor and Turbine Isentropic Efficiencies

For a compressor, the isentropic efficiency relates actual work per unit mass flow to that of an ideal machine with equivalent pressure change as below:

$$\eta_{comp} = \frac{Ideal\ work}{Actual\ work} \tag{142}$$

By neglecting the changes in kinetic and potential energies associated with the fluid stream flowing through the compressor and assuming an adiabatic process, the above relation can be expressed as:

$$\eta_{comp} \cong \frac{(\Delta h)_{isentropic}}{(\Delta h)_{actual}} \tag{143}$$

Treating the flow as a perfect gas, for which $h = C_P T$:

$$\eta_{comp} \cong \frac{(\Delta T)_{isentropic}}{(\Delta T)_{actual}} \tag{144}$$

Assuming a process between points j and $j+1$:

$$\eta_{comp} = \frac{T_{j+1,s} - T_j}{T_{j+1} - T_j} = \frac{(T_{j+1,s}/T_j) - 1}{(T_{j+1}/T_j) - 1} \tag{145}$$

By substituting $T_{j+1,s}/T_j = (p_{j+1}/p_j)^{\gamma-1/\gamma}$

$$\eta_{comp} = \frac{(p_{j+1}/p_j)^{\gamma-1/\gamma} - 1}{(T_{j+1}/T_j) - 1} \tag{146}$$

This equation can also written as:

$$\frac{T_{j+1}}{T_j} = \frac{(p_{j+1}/p_j)^{\gamma-1/\gamma} - 1}{\eta_{comp}} + 1 \tag{147}$$

For a turbine, the isentropic efficiency relates actual work per unit mass flow to that of an ideal machine with equivalent pressure change as below:

$$\eta_{turb} = \frac{Actual\ work}{Ideal\ work} \tag{148}$$

Similarly, the turbine isentropic efficiency for a process begins from a point j to a point $j+1$ can be expressed as:

$$\eta_{turb} = \frac{(T_{j+1}/T_j) - 1}{(p_{j+1}/p_j)^{\gamma-1/\gamma} - 1} \tag{149}$$

or,

$$\frac{T_{j+1}}{T_J} = \eta_{turb}\left[\left(\frac{p_{j+1}}{p_j}\right)^{\gamma-1/\gamma} - 1\right] + 1 \tag{150}$$

B2: Compressor and Turbine Stage Efficiencies

For a multistage compressor, each stage has an isentropic efficiency. For a N-stage compressor with equal stage pressure ratios ($\pi_{sc}=(p_{j+1}/p_j)^{1/N}$) and equal stage efficiencies (η_{sc}), it can be shown that [233]:

$$\eta_{comp} = \frac{\pi_{sc}^{N(\gamma-1)/\gamma} - 1}{\left[1 + (1/\eta_{sc})(\pi_{sc}^{(\gamma-1)/\gamma} - 1)\right]^N - 1} \tag{151}$$

This equation can give us the compressor stage efficiency as:

$$\eta_{sc} = \frac{\pi_{sc}^{(\gamma-1)/\gamma} - 1}{\left[\sqrt[N]{1 + \frac{\pi_{sc}^{N(\gamma-1)/\gamma} - 1}{\eta_{comp}}}\right] - 1} \tag{152}$$

For a multistage turbine, when all stages have the same stage pressure ratios ($\pi_{st} = (p_{j+1}/p_j)^{1/N}$) and equal stage efficiencies (η_{st}), the turbine isentropic efficiency can be written as:

$$\eta_{turb} = \frac{1 - \left[1 - \eta_{st}(1 - \pi_{st}^{(\gamma-1)/\gamma})\right]^N}{1 - \pi_{st}^{N(\gamma-1)/\gamma}} \tag{153}$$

So, the turbine stage efficiency is then becomes:

$$\eta_{st} = \frac{1 - \sqrt[N]{1 - \eta_{turb}(1 - \pi_{st}^{N(\gamma-1)/\gamma})}}{1 - \pi_{st}^{(\gamma-1)/\gamma}} \tag{154}$$

B3: Compressor and Turbine Polytropic Efficiencies

In general, for a polytropic process beginning from a point j to a point $j+1$ the following relation can be written:

$$\frac{p_{j+1}}{p_j} = \left(\frac{T_{j+1}}{T_j}\right)^{n/(n-1)} \tag{155}$$

where n is called polytropic component. The values of n for some familiar processes are given below:

Isobaric process $n = 0$

Isothermal process $n = 1$

Isentropic process $n = \gamma$

The polytropic efficiency is a useful concept for a non-isentropic process. For a non-isentropic process:

For compression: $\frac{n}{n-1} = \frac{\gamma \eta_P}{\gamma - 1}$

For expansion: $\frac{n}{n-1} = \frac{\gamma}{(\gamma - 1)\eta_P}$

where η_P is the polytropic efficiency.

Therefore, for a non-isentropic process beginning from a point j to a point $j+1$ we can write:

For a compression process:

$$\frac{p_{j+1}}{p_j} = \left(\frac{T_{j+1}}{T_j}\right)^{\gamma \eta_P / (\gamma - 1)} \tag{156}$$

For an expansion process:

$$\frac{p_{j+1}}{p_j} = \left(\frac{T_{j+1}}{T_j}\right)^{\gamma / (\eta_P (\gamma - 1))} \tag{157}$$

For a compressor, assuming that the polytropic efficiency is constant over the pressure ratio, the relation between the isentropic efficiency and the polytropic efficiency is given by using Eq. (146) and (156) as:

$$\eta_{comp} = \frac{(p_{j+1}/p_j)^{(\gamma-1)/\gamma} - 1}{(p_{j+1}/p_j)^{(\gamma-1)/(\gamma \eta_{Pc})} - 1} \tag{158}$$

Similarly, the relation between the turbine isentropic efficiency and the polytropic efficiency can be shown as:

$$\eta_{turb} = \frac{(p_{j+1}/p_j)^{(\gamma-1)\eta_{Pt}/\gamma} - 1}{(p_{j+1}/p_j)^{(\gamma-1)/\gamma} - 1} \tag{159}$$

B4: Entropy Calculation

The relation which relates the entropy generation between points j and $j+1$ is:

$$s_{j+1} = s_j + Cp\ln(\frac{T_{j+1}}{T_j}) - R\ln(\frac{p_{j+1}}{p_j}) \tag{160}$$

The above all equations can be used to sketch T-s diagrams of the gas turbine cycles. For a case when a four-port wave rotor is added to a baseline gas turbine engine, similar methodology described above is adopted as will be explained in the following. Referring to state numbering introduced in Figure 6 (TF wave rotor) or Figure 34 (RF wave rotor), the below procedure is performed to sketch the T-s diagrams for such enhanced cycle.

- **Path 0-1: Compressor**

The stage pressure ratio can be simply obtained by:

$$\pi_{sc} = \sqrt[N]{\frac{p_{t1}}{p_0}} \tag{161}$$

where N can be considered any arbitrary integer number greater than unity. N =12 is chosen for this study. By knowing the compressor isentropic efficiency, Eq. (152) gives the compressor stage efficiency. Then, Eq. (147) calculates the temperature at each pressure stage $j+1$. Finally, the entropy at each stage can be obtained by using Eq. (160).

- **Path 1-2: Compression in the Wave Rotor**

A similar approach described for the compressor path can be used for the wave rotor compression process by simulating a wave rotor stage pressure ratio obtained by:

$$\pi_s = \sqrt[N]{\frac{p_{t2}}{p_{t1}}} \tag{162}$$

- **Path 2-3: Combustion Chamber**

The treatment of this path is different from the earlier paths because there is no information about isentropic paths across the combustion process. Indeed, Eq. (155) should be used to find the polytropic component along path 2-3. To do so, for the path 2-3, Eq. (155) can be expressed as:

$$n = \frac{1}{1 - ln(\frac{T_{t3}/T_{t2}}{p_{t3}/p_{t2}})} \tag{163}$$

or,

$$n = \frac{1}{1 - ln(\frac{T_{t3}/T_{t2}}{\Pi_{comb}})} \tag{164}$$

By calculating n, Eq. (155) will be used to calculate the pressure (or temperature) in each temperature (or pressure) step.

In calculating the entropy at each step, the values of Cp (specific heat) and R (gas constant) need to be determined. For the first approximation, the following estimation have been made:

$$Cp_{ave} = \frac{Cp_{air} + Cp_{gas}}{2} \tag{165}$$

$$R_{ave} = \frac{R_{air} + R_{gas}}{2} \tag{166}$$

- **Path 3-4: Expansion in the Wave Rotor**

The stage pressure ratio is obtained by:

$$\pi_s = \sqrt[N]{\frac{p_{t3}}{p_{t4}}} \tag{167}$$

Therefore, the wave rotor expansion stage efficiency can be obtained by using Eq. (154). Then, using Eq. (150) leads to the temperature at each pressure stage $j+1$.

- **Path 4-5: Turbine**

A similar approach described for the wave rotor expansion process now is used for the flow expansion in the turbine using the turbine stage pressure ratio obtained by:

$$\pi_{st} = \sqrt[N]{\frac{p_{t4}}{p_{t5}}} \tag{168}$$